THE MAGNETIC AND CHEMICAL STRUCTURES OF THE HEUSLER ALLOYS

by

Peter John Webster

A thesis submitted to the University of Sheffield in candidature for the degree of Doctor of Philosophy

Department of Physics
The University
Sheffield

August 1968.

PREFACE

The Heusler alloys have been of interest since 1903 when F. Heusler reported that ferromagnetic alloys could be made from non-ferromagnetic constituents copper-manganese bronze and group B elements such as aluminium and tin. A number of investigations have been conducted into the magnetic properties of these alloys, and it has been established that their ferromagnetism is closely associated with their chemical ($L2_1$) structure. However, the investigations have usually been concerned with only one, or a very limited number of alloys, and although several theories have been advanced to explain their properties they have been based on very limited and sometimes conflicting data.

The present investigation has been conducted with a view to obtaining more complete data on a larger range of alloys to provide a better experimental foundation for theoretical calculations.

The thesis is divided into 9 chapters. The first 2 are a review of earlier work and of the basic theories of magnetic ordering. Chapter 3 is concerned with diffraction theory, and chapter 4 with experimental techniques. The experimental results for the various alloy series are presented in chapters 5, 6, 7, and 8, and chapter 9 is devoted to a summary and discussion of their structural and magnetic properties.

The work described in this thesis has been aided by many people to whom I accord my most sincere thanks.

To Professor R.S. Tebble, who suggested the subject of research,

for his continued help and encouragement.

Professors N.H. March and G.E. Bacon and the U.K.A.E.A. for permission to use facilities at Sheffield and Harwell.

My colleagues for much assistance and helpful discussion, especially Dr. D.P. Oxley for assistance at the start of the work, Dr. P. Gaunt for our many discussions on problems connected with diffraction and Dr. J.G. Booth for many helpful discussions and for his criticisms of the manuscript.

The members of the technical staff, particularly Mr. K.C. Ward for his skill in the construction of the equipment and Miss K. Ashton for her careful tracing of the diagrams.

Peter J. Webster

Salford

August 1968

Peter J. Webster

ABSTRACT

Four series of alloys have been prepared with the $L2_1$ or B2 structures at the compositions Cu_2MnX, Ni_2MnX, Co_2MnX, and Pd_2MnX, where X is a B sub-group element such as Al, Si, Ga, Ge, In, Sn, or Sb. A further series, with the Cl_b structure, has been prepared at the compositions CuMnSb, NiMnSb, CoMnSb, and PdMnSb. X-ray diffraction, neutron diffraction, and magnetic susceptibility data have been used to determine the chemical structures, the degrees and types of long-range order, and the magnetic structures of all the alloys.

Manganese, the one element common to all the alloys, carries in every case a large magnetic moment, usually about 4 β, which is coupled, via some form of exchange interaction, to moments on neighbouring Mn ions in an ordered magnetic structure. In addition to the traditional ferromagnetic Heusler alloys several new intermetallic compounds with the $L2_1$ or B2 structures have been discovered, some with antiferromagnetic or complex spiral spin structures.

A generalized molecular field theory has been employed as a first step in the theoretical analysis to indicate the major aspects of the exchange forces that are present. The principal features that emerge indicate that either several different exchange mechanisms are present or that a single, oscillatory, relatively long-range exchange force is operating. Further lines of research are suggested that would lead to a more detailed understanding of the magnetic properties of this group of alloys.

CONTENTS

CHAPTER 1

An historical survey of earlier investigations

In 1903 Heusler reported that manganese-copper bronze can be alloyed with tin, aluminium, arsenic, antimony, bismuth or boron to produce ferromagnetic alloys even though none of the constituent elements is itself ferromagnetic.

Owing to its important bearing on the general theory of magnetism this discovery excited considerable interest and led to numerous further investigations. Starck and Haupt (1903) measured the intensities of magnetization of several alloys in the Cu-Mn-Al and Cu-Mn-Sn systems, and found maxima at the approximate compositions Cu_2MnAl and Cu_6Mn_3Sn. Ross and Gray (1910) reinvestigated the Cu-Mn-Sn system and found a second, larger, maximum in magnetic intensity near the composition Cu_2MnSn. In addition, they showed that the magnetization is affected by heat treatment. Quenching from 580°C usually results in a marked reduction in magnetization. Take and Semm (1914) made a systematic survey of magnetism in the Cu-Mn-Sn system and published magnetic contours showing two pronounced maxima, one at Cu_6Mn_3Sn and the other, and larger one, at Cu_2MnSn.

Young (1923) investigated the structure of an alloy at the approximate composition Cu_2MnAl using X-ray powder diffraction techniques. He was able to show that the structure of the alloy depends upon its previous heat treatment. The weakly magnetic alloy that had been

quenched from red heat was indexed as f.c.c. with a lattice parameter 3.70 kX, and the more magnetic 'naturally aged' specimen as a mixture of f.c.c. together with a b.c.c. structure of lattice parameter 2.98 kX.

Potter (1929) investigated the X-ray structure of single crystals of Cu_2MnAl and found that the alloy was b.c.c. with a lattice parameter 2.95 kX. However the presence of f.c.c. superlattice lines indicated the existence of planes of low scattering power, and he was able to show that the Al atoms were arranged on an f.c.c. sublattice of cell size 5.9 kX. He was unable to distinguish between the Cu and Mn atoms because of the small difference in atomic scattering factors. The directional magnetic properties were measured using the torsion method and disc-shaped single crystals cut in the (100), (110), and (111) planes. The results bore a striking similarity to those of f.c.c. nickel, but were totally unlike those of b.c.c. iron. As it was thought unlikely that the directional magnetic properties were much influenced by the spatial arrangement of the Al atoms, it was suggested that Mn, which was known to form several other ferromagnetic alloys, was also arranged on an f.c.c. sublattice. The two possible structures which would satisfy the requirements of chemical proportions, density, and X-ray data are shown in figure (1.1). In structure (1) the Cu atoms are arranged on a simple cubic sublattice with Mn and Al atoms at alternate body-centres. In structure (2) there are four interpenetrating f.c.c. sublattices, two of Cu, and one each of Mn and Al.

Persson (1929) working independently on a series of alloys of the form $(CuMn)_3Al$ came to the same structural conclusions. In addition he

showed that only alloys with Mn content >19 At.% are ferromagnetic, and concluded that this amount was necessary to produce an f.c.c. Mn sublattice.

Bradley and Rodgers (1933) investigated the aluminium Heusler alloy with the object of locating by direct experiment the positions of the Mn atoms, and to test whether the change in structure without change of composition would affect the ferromagnetic character of the alloy. An alloy at the composition $Cu_{2.2}Mn_{0.65}Al_{1.15}$ was investigated because it exhibited an almost complete change in structure with heat treatment. After annealing at 500°C and slow-cooling, the structure corresponded to the $\delta\ Cu_9Al_4$ structure, and was practically non-magnetic. The same alloy, after quenching from 800°C, had a b.c.c. structure with an f.c.c. superlattice and was strongly ferromagnetic, confirming that the magnetic properties of the alloy are structure dependent.

The difference between the atomic scattering factors of Mn and Cu, of atomic numbers 25 and 29 respectively, is small, and to distinguish between them is a matter of some difficulty. Bradley and Rodgers overcame this problem by comparing accurate photometer measurements of powder diffraction photographs taken using X-rays of different wavelengths, making use of the anomalies in atomic scattering factor which occur when the frequency of the X-radiation is close to the characteristic absorption frequency of the scattering element. Diffraction photographs were taken using iron, copper, and zinc targets. The scattering factors of Cu and Mn are depressed almost equally for copper radiation, but the scattering factor of Mn is depressed more than that

of Cu with iron radiation, and less than that of Cu with zinc radiation. The disparity between the scattering factors of the Cu and Mn atoms is thus accentuated with iron radiation and reduced by zinc radiation. The anomalous scattering effects were evident from the change in relative intensities of the 'odd' and 'even' superlattice lines, indicating that the Mn atoms were also ordered. The intensities were such as to indicate that the order is as shown in structure (1), figure (1.1). The actual Heusler ($L2_1$) structure is illustrated in figure (1.2).

O. Heusler (1934), working independently, derived the same structure and showed that the lattice parameter had a maximum value of 5.935 kX at the composition Cu_2MnAl. He also determined the magnetization after various heat treatments, and recorded a maximum value equivalent to 3.4 Bohr magnetons per Cu_2MnAl group.

The range of alloys known to have the Heusler structure has been extended in more recent times, and their structural and magnetic properties have been the subject of many investigations. The most reliable results, together with those that have been the subject of the present investigation, are tabulated and discussed in the appropriate chapters.

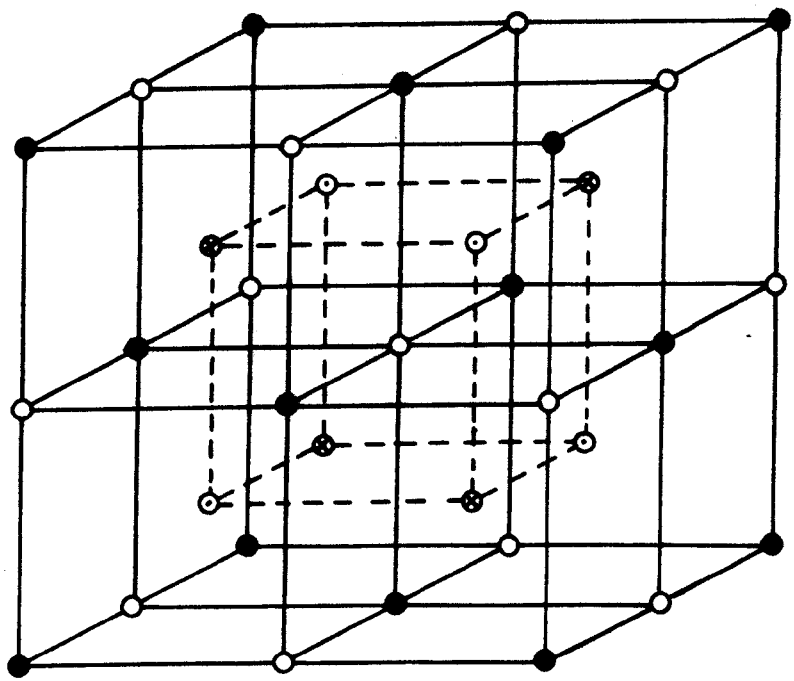

		● A	⊙ B	○ C	⊗ D
Structure	(1)	Cu	Mn	Cu	Al
Structure	(2)	Cu	Cu	Mn	Al

Fig 1·1 The two possible structures of Cu_2MnAl

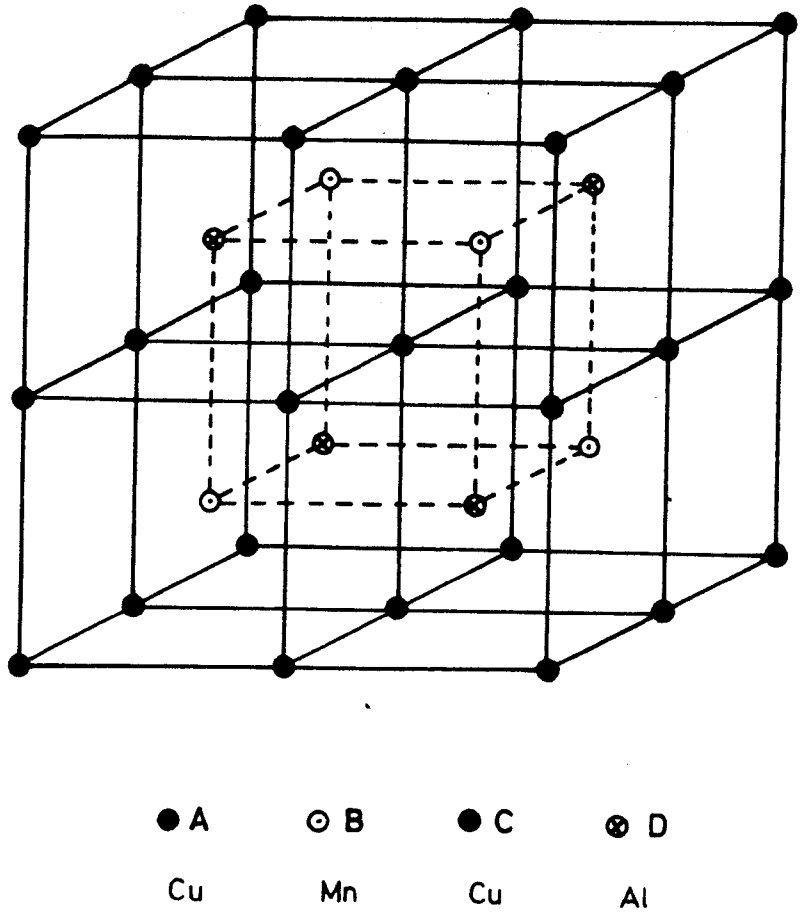

Fig 1·2 The Heusler Structure

CHAPTER 2

A survey of the theories of magnetic ordering

2.1 Introduction

The magnetic properties of materials are very varied but it is possible to classify them into several groups characterized by their behaviour in a magnetic field. The principal classifications are as follows.

Diamagnetism

Paramagnetism

Ferromagnetism

Antiferromagnetism

Ferrimagnetism.

The atomic origins of magnetism have been explained in terms of the magnetic moments associated with the orbital and spin motions of the electrons. The explanations are summarized briefly below.

2.2 Diamagnetism

Diamagnetic materials have a small negative temperature independent susceptibility χ of magnitude of the order of 10^{-5}emu/mole. Diamagnetism is a consequence of Lenz's law applied to the orbital motion of electrons round an atom, and is a property of all materials. However, since the diamagnetic contribution to the total susceptibility is relatively small for the materials that we shall be concerned with, it will not be considered further.

2.3 Paramagnetism

Each electron in an atom has an angular momentum $\underline{l}$ associated with its orbital motion plus an intrinsic spin angular momentum $\underline{s}$. In Russell-Saunders coupling the individual momenta couple to give a total orbital angular momentum $\underline{L} = \sum_i \underline{l}_i$, and a total spin angular momentum $\underline{S} = \sum_i \underline{s}_i$. Finally $\underline{L}$ and $\underline{S}$ couple to give a total angular momentum $\underline{J} = \underline{L} + \underline{S}$.

Both the orbital and spin angular momenta have a magnetic moment associated with them, the magnetic moment operators being

$$\underline{\mu}_L = -\frac{|e|\hbar}{2mc}\underline{L} = -\beta\,\underline{L} \qquad (2.1)$$

and

$$\underline{\mu}_S = -2\beta\underline{S}$$

where $\beta = |e|\hbar/2mc = 0.927 \times 10^{-20}$ emu, is the fundamental unit of magnetic moment entitled the Bohr magneton. $\underline{\mu}_L$ and $\underline{\mu}_S$ combine to give a total magnetic moment $\underline{\mu}$, where

$$\underline{\mu} = -\beta(\underline{L} + 2\underline{S}) \qquad (2.2)$$

However, since the ratios of magnetic moment to angular momentum are different for the orbital and spin cases, $\underline{\mu}$ and $\underline{J}$ are not parallel. $\underline{\mu}$ precesses about $\underline{J}$ such that its component perpendicular to $\underline{J}$ averages to zero and the component parallel to $\underline{J}$, μ_J, is given by

$$\mu_J^2 = g^2 J(J+1)\beta^2 \qquad (2.3)$$

where g is the Landé g-factor given by

$$g = 1 + \frac{J(J+1) + L(L+1) + S(S+1)}{2J(J+1)} \qquad (2.4)$$

When a magnetic field is applied, the angular momentum is space quantized, and only certain orientations are possible. The quantization rule is such that the projection of $\underline{J}$ along the field direction has the value $m\hbar$, where m may take the values m = J, (J-1), (J-2), ...-(J-1),-J, and the component of magnetic moment μ_H parallel to the field is given

by

$$\mu_H = -mg\beta \tag{2.5}$$

The potential energy of a dipole in a magnetic field is given by

$$E = \mu_H H = -mg\beta H \tag{2.6}$$

and according to Maxwell-Boltzmann statistics the number of atoms having the quantum number m is proportional to $\exp(-E/kT) = \exp(mg\beta H/kT)$.

The total magnetic moment per unit volume is thus given by

$$I = \frac{n \sum_{m=-J}^{m=+J} mg\beta \exp(mg\beta H/kT)}{\sum_{m=-J}^{m=+J} \exp(mg\beta H/kT)} \tag{2.7}$$

which after some algebraic manipulation reduces to the form

$$I = ng\beta J\left[\left(\frac{2J+1}{2J}\right)\coth\left(\frac{2J+1}{2J}\right)y - \frac{1}{2J}\coth\left(\frac{y}{2J}\right)\right] \tag{2.8}$$

The expression in brackets is known as the Brillouin function B(y) where $y = gJ\beta H/kT$. As J becomes very large B(y) approaches as a limit the classical Langevin function L(α), where $L(\alpha) = (\coth\alpha - 1/\alpha)$ and $\alpha = \mu H/kT$.

At normal field strengths and ordinary temperatures $g\beta mH/kT \ll 1$, and the exponentials in equation (2.7) may be approximated by $(1 + g\beta mH/kT)$. Calculation results in an approximate paramagnetic susceptibility

$$\chi = I/H = ng^2J(J+1)\beta^2/3kT = C/T \tag{2.9}$$

This equation is known as the Curie law.

It has been assumed in the above analysis that any interaction between neighbouring atomic moments is unimportant. The analysis may be

extended to take into account the interaction of neighbouring atomic moments using the molecular field approach of Weiss (1907). It is assumed that the effect of neighbouring moments may be represented by an internal field H_i proportional to the magnetization. The total effective field H_e is thus

$$H_e = H + cI \tag{2.10}$$

where c is the molecular field constant. Substitution of H_e for H in equation (2.9) results in

$$\chi = \mu_J^2 n/3k(T - c\mu_J^2 n/3k) = C/(T - \theta) \tag{2.11}$$

This is the Curie-Weiss law, where $\theta = c\mu_J^2 n/3k$ is the paramagnetic Curie temperature.

2.4 Ferromagnetism

A ferromagnetic material is one in which the atomic moments are strongly coupled and tend to be aligned parallel. As a result below a critical temperature, the ferromagnetic Curie temperature θ_F, such materials possess a spontaneous magnetization even in the absence of an applied field.

Many ferromagnetic materials, however, exist in an apparently unmagnetized state below their Curie temperatures, but exhibit a large moment on the application of a small field. Weiss (1907) was able to explain these results by postulating the existence of small regions called domains. Each domain is spontaneously magnetized but the direction of magnetization of each domain is not necessarily parallel, and the material may have any nett magnetization from zero to the saturation value at the temperature of measurement. The hypothesis of Weiss has

since become well established.

The intensity of magnetization of a ferromagnetic may be calculated on the assumption that the interaction between neighbouring magnetic moments may be represented by a Weiss molecular field. Equation (2.8) is then modified to become

$$I = ng\beta JB(x) \qquad (2.12)$$

where B(x) is the Brillouin function, and

$$x = gJ\beta(H + cI)/kT \qquad (2.13)$$

The spontaneous magnetization I(T) at temperature T may be obtained in terms of I(0), the spontaneous magnetization at $0^{o}K$, by putting H = 0 in equations (2.12) and (2.13). The resulting equations are

$$I(T)/I(0) = B(x) \qquad (2.14)$$

and

$$I(T)/I(0) = kTx/ncg^{2}\beta^{2}J^{2} \qquad (2.15)$$

Solution of these two simultaneous equations may be conveniently obtained graphically from the non-zero intersections of the two curves which are shown in figure (2.1a). P is the solution for $T < \Theta_F$, and the resulting reduced spontaneous magnetization curves are shown in figure (2.1b). Above $T = \Theta_F$ there is no spontaneous magnetization.

The calculated curves are in good agreement with many experimental results, but detailed differences do exist, and the origin of the internal field was unexplained until Heisenberg (1928) applied the concept of the exchange interaction.

2.5 The exchange interaction

An estimate of the magnitude of the internal molecular field may be obtained from the Curie temperatures of typical ferromagnetic materials

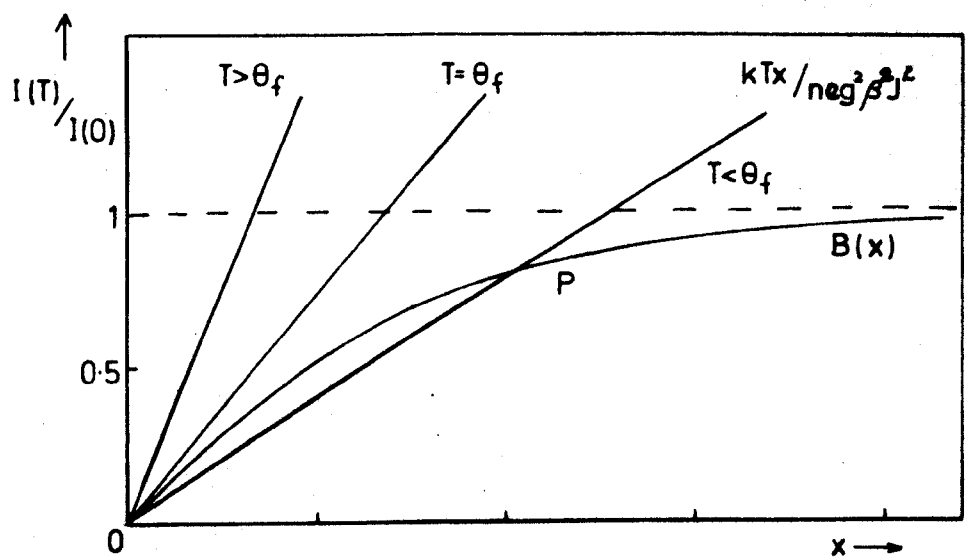

Fig 2·1(a) Graphical method for determination of spontaneous magnetization at temperature T

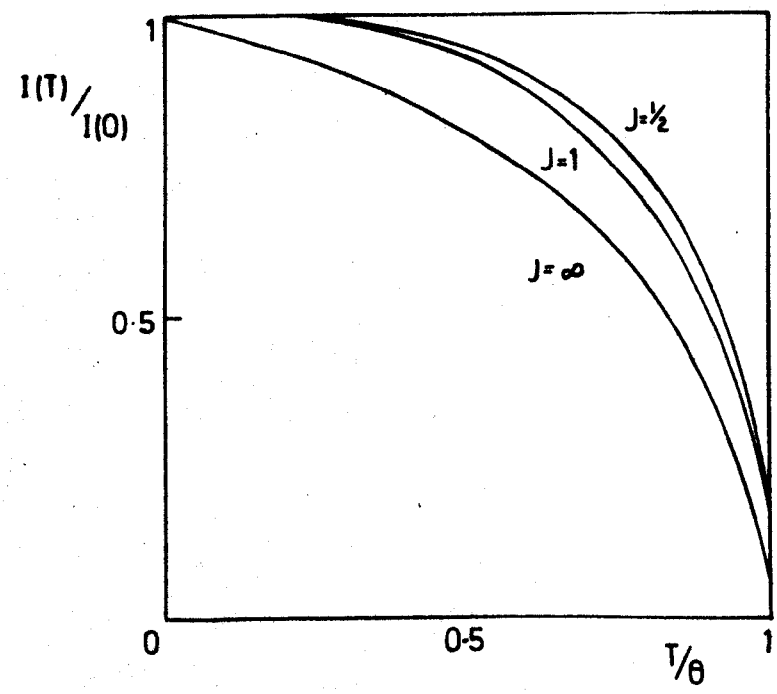

Fig 2·1(b) Spontaneous magnetization as a function of temperature [J = ∞ corresponds to classical case]

since $\mu H_i \sim k\Theta_F$. For a material with $\Theta_F \sim 1000^oK$, and $\mu \sim \beta$ per atom, $H_i \sim 10^7$ Oe, but the field due to a classical dipole β at a typical nearest neighbour distance is $\sim 10^3$ Oe.

Heisenberg (1928) first showed that a Weiss molecular field of the correct order of magnitude could originate as a result of the quantum mechanical exchange interaction between electrons from neighbouring atoms. This may be best illustrated by considering the hydrogen molecule.

Suppose that the two hydrogen atoms A and B have wave functions ψ_a and ψ_b, and energy levels E_a and E_b respectively when moving independently. Let the electrons have spin wave functions α or β corresponding to spins +1/2 or -1/2 respectively. Then, as a result of the Pauli exclusion principle, the total wave functions of the molecule must be antisymmetric, and are

$$\psi_1 = \{\psi_a(1)\psi_b(2) + \psi_a(2)\psi_b(1)\}\{\alpha(1)\beta(2) - \alpha(2)\beta(1)\} \qquad (2.16a)$$

$$\psi_{11} = \{\psi_a(1)\psi_b(2) - \psi_a(2)\psi_b(1)\}\begin{Bmatrix} \alpha(1)\alpha(2) \\ \beta(1)\beta(2) \\ \alpha(1)\beta(2) + \alpha(2)\beta(1) \end{Bmatrix} \qquad (2.16b)$$

where ψ_1 is the singlet state corresponding to antiparallel alignment of spins, and ψ_{11} represents the three triplet states associated with parallel alignment of spins. The energies of the two types of states are

$$E_1 = E_c + J_{12} \qquad (2.17a)$$

$$E_{11} = E_c - J_{12} \qquad (2.17b)$$

where E_c is the sum of the atomic and Coulomb interaction energies, and J_{12} is the exchange integral given by

$$J_{12} = \int \psi_a^*(1)\psi_b^*(2)V_{12}\psi_a(2)\psi_b(1)\, dv_1 dv_2 \qquad (2.18)$$

V_{12} is the mutual interaction energy of the two electrons, and dv_1, dv_2 are their volume elements. It is clear that the triplet ferromagnetic state is only energetically favourable when the exchange integral is positive.

The exchange energy H between two spins $\underline{s}_i$ and $\underline{s}_j$ may be re-expressed in the Dirac (1935) form

$$H = -2J_{ij}\underline{s}_i \cdot \underline{s}_j \qquad (2.19)$$

where J_{ij} is the exchange integral for the two electrons i and j.

Similarly we have for two atoms i and j, each of which has at least one unpaired spin

$$H = -2J_{ij}\underline{S}_i \cdot \underline{S}_j \qquad (2.20)$$

where $\underline{S}_i = \sum_i \underline{s}_i$.

If it may be assumed that the exchange integral is negligible except between nearest neighbours, the exchange energy for a given atom i with its j nearest neighbours is

$$H = -2J_e \sum_j \underline{S}_i \cdot \underline{S}_j \qquad (2.21)$$

where J_e is the exchange integral which is assumed isotropic.

The magnitude of J_e may in principle be related to the Curie temperature Θ, and the Molecular field constant c by carrying out the summation of equation (2.21). This is not possible however without making further approximations. One such approximation is the Ising (1925) model which amounts in effect to assuming that the instantaneous values of the neighbouring spins may be replaced by their time averages. Thus for z

nearest neighbours

$$H = -2zJ_e(\bar{S}_{xi}\bar{S}_{xj} + \bar{S}_{yi}\bar{S}_{yj} + \bar{S}_{zi}\bar{S}_{zj}) \qquad (2.22)$$

and if z is the axis of magnetization,

$$\bar{S}_{xj} = \bar{S}_{yj} = 0$$

hence $$H = -2zJ_eS_{zi}\bar{S}_{zj} \qquad (2.23)$$

The magnetization $$I = ng\beta\bar{S}_{zj}$$

hence $$H = -2zJ_eS_{zi}I/ng\beta \qquad (2.24)$$

which is equal to the potential energy of the spin i in the Weiss molecular field cI.

i.e. $$H = -gS_{zi}\beta cI \qquad (2.25)$$

Equating (2.24) and (2.25) results in

$$c = 2zJ_e/ng^2\beta^2 \qquad (2.26)$$

And since $$\theta = c\mu^2n/3k$$

we have $$\theta = 2zJ_eS(S + 1)/3k \qquad (2.27)$$

2.6 Antiferromagnetism and ferrimagnetism

If the exchange integral J_e is negative, rather than positive as in the ferromagnetic case, then coupled spins will tend to antiparallel alignment and antiferromagnetism or ferrimagnetism will result.

The first theory of antiferromagnetism was developed by Néel and extended by Van Vleck (1941) as a generalization of the Weiss molecular field theory. In summary, it was supposed that, if the atomic lattice of magnetic atoms is such as to permit its division into two equivalent interpenetrating sublattices A and B such that A atoms have only B atoms

as nearest neighbours and vice versa, then if only nearest neighbour interactions are considered the exchange between atoms on sublattice A is entirely with atoms on sublattice B. It was shown that such a system possesses a critical temperature, Θ_N the Néel temperature, below which the spins on the two sublattices are coupled antiparallel. Above Θ_N the moments are disordered as in a ferromagnetic above its Curie temperature, and the susceptibility is given by the relation

$$\chi = \frac{ng^2\beta^2S(S+1)}{3k(T+\Theta_N)} \qquad (2.28)$$

which is identical to the Curie-Weiss law, but with a negative intercept $\Theta = -\Theta_N$.

Below the critical temperature, each sublattice acquires a spontaneous magnetization and the susceptibility depends upon whether the applied field is parallel or perpendicular to the antiferromagnetic axis.

When the external field is applied perpendicular to the antiferromagnetic axis the susceptibility below Θ_N is constant and is given by

$$\chi_\perp = ng^2\beta^2S(S+1)/6k\Theta_N \qquad (2.29)$$

When the external field is applied parallel to the antiferromagnetic axis, its effect is to increase the magnetization of one sublattice and to decrease that of the other. The susceptibility varies from zero at $0^\circ K$ to a maximum equal to the perpendicular susceptibility at the Néel temperature, and is represented by the equation

$$\chi_{11} = \frac{ng^2\beta^2S^2B'(y)}{k(T+3\Theta_NS(S+1)^{-1}B'(y))} \qquad (2.30)$$

where B(y) is the Brillouin function for

$$y = 2z|J|S\bar{S}/kT \qquad (2.31)$$

$\overline{S}$ is the mean value of S at temperature T, and z is the number of nearest neighbours.

For powder, or polycrystalline, samples an average over all possible orientations must be taken, and for cubic materials it is given by

$$\chi = \frac{1}{3}\chi_{11} + \frac{2}{3}\chi_{\perp} \qquad (2.32)$$

It follows that $\chi(0) = \frac{2}{3}\chi(\theta_N)$, where $\chi(0)$ and $\chi(\theta_N)$ are the susceptibilities at $0^{\circ}K$ and θ_N respectively.

Ferrimagnetism is the more general case of antiferromagnetism, and occurs when the magnetizations of sublattices A and B are unequal. As a result, ferrimagnetics possess a spontaneous moment below their critical temperatures.

2.7 Band theories of ferromagnetism

In the discussions of ferromagnetism and antiferromagnetism so far considered, it has been assumed that the magnetic moments may be regarded as localized at the magnetic atom sites and that the exchange coupling is a direct Heisenberg exchange between nearest neighbours. In the ferromagnetic transition metals it is assumed that the magnetic moments originate in the incomplete 3d shells, and the 3d wave functions of adjacent atoms overlap sufficiently to provide a direct exchange interaction of the appropriate magnitude and sign. However, since most ferromagnetic materials are either metals or alloys, it is clear that a localized model that does not take into account the effects of the conduction electrons is at best incomplete.

When an assembly of free atoms is condensed into a solid the wave functions of neighbouring atoms overlap, and the formerly discrete energy

levels of the outer electrons become broadened into a band of available energy states. The first calculations for the 3d and 4s band electrons of the iron group transition metals were made by Slater (1936). The energy band for the 3d electrons is relatively narrow and is overlapped in energy by the much wider 4s band. Since the bands will be filled to the same level, the number of electrons (or holes) per atom in each band will in general be non-integral. This leads to an immediate explanation of the experimentally observed fact of non-integral Bohr magneton numbers of the ferromagnetic elements.

A quantitative 'collective electron theory of ferromagnetism' was proposed by Stoner (1938)(1948)(1951) in a series of papers and reviews. The theory is based on the following assumptions.

1. The 3d band is parabolic in the region of the Fermi level. i.e. $n(E)dE = AE^{1/2}dE$.

2. The electrons (holes) obey Fermi-Dirac statistics.

3. The exchange energy $J(\zeta)$ is proportional to the square of the relative magnetization ζ, as in the Weiss theory, and may be written $J(\zeta) = -\frac{1}{2} Nk\Theta'\zeta^2$, where N is the number of holes and Θ' a parameter which in the 'classical' treatment would correspond to the Curie temperature.

The reduced magnetization and reciprocal susceptibility curves derived by Stoner are in reasonable agreement with experiment. The $1/\chi,T$ curve is concave upwards near the Curie temperature but approaches the corresponding 'classical curve' asymptotically at high temperatures. The reduced spontaneous magnetization curves are always lower than the

limiting 'classical' case. Later Wohlfarth (1951) extended the analysis to apply to rectangular energy bands, but concluded that the band shape is less decisive in determining many of the properties of ferromagnetic substances than the form of the exchange energy $J(\zeta)$.

2.8 Indirect exchange theories

The localized and collective electron theories of ferromagnetism approach the problem of explaining cooperative magnetic phenomena from two opposite extremes, and attempts have been made to construct theories using models intermediate between the two. One such attempt is due to Zener (1951)(1952)(1953).

In the Zener model it is assumed that the 3d electrons remain localized whilst the 4s electrons form an energy band, and the interactions are governed by the following simple principles.

1. The spin correlation between the electrons in the incomplete d shell of a single atom within a solid is essentially the same as when it is isolated in the gaseous state; the incomplete d shell of an atom in a metal has the highest nett electron spin consistent with the number of electrons therein.
2. The exchange integral between d shells of adjacent atoms is of such a sign as tends always to lead to antiferromagnetic alignment of the d shell spins.
3. The spin of an incomplete d shell is strongly coupled to the spin of the conduction electrons, and this coupling tends to align the incomplete d shells in a ferromagnetic manner.

The type of magnetic structure that will prevail for a particular

transition metal will depend upon the relative magnitudes of the various types of coupling.

The exchange energy due to the direct coupling of the d shells of adjacent atoms may be represented by $\frac{1}{2}\alpha S_d^2$ per atom. Here S_d is the average localized spin component per atom in Bohr magnetons, and α is a positive exchange constant which decreases rapidly with a decreasing amount of overlap of the d shells of adjacent atoms.

The s - d spin coupling results in an energy term of the form $-\beta S_d S_c$, where S_c is the nett magnetization of the conduction electrons in Bohr magnetons per atom. The coefficient β is positive and is the order of magnitude of one electron volt.

Since, in the Zener model, there is a nett conduction electron/magnetization S_c there must be an additional term in the energy expression to represent the increase in Fermi kinetic energy. Provided the inbalance in conduction electron spin distribution is small the additional energy term may be written $\frac{1}{2}\gamma S_c^2$. The coefficient γ is related to the Fermi energy E, and the number of conduction electrons per atom n by the relation $\gamma = 2E/3n$.

The total spin energy E_s is thus

$$E_s = \tfrac{1}{2}\alpha S_d^2 - \beta S_d S_c + \tfrac{1}{2}\gamma S_c^2 \qquad (2.33)$$

Since the conduction electron contribution to the entropy of the system is negligible, the equilibrium value of S_c is that which minimizes E_s. Hence, differentiating we obtain

$$S_c = (\beta/\gamma) S_d \qquad (2.34)$$

Substitution in (2.33) gives the equilibrium value

$$E_s = \tfrac{1}{2}(\alpha - \beta^2/\gamma) S_d^2 \qquad (2.35)$$

In order for ferromagnetism to occur the coefficient $(\alpha - \beta^2/\gamma)$ must be negative. When the coefficient is positive an antiferromagnetic structure will result.

Zener computed values of β^2/γ for the ferromagnetic elements iron, cobalt and nickel and compared them with the measured Weiss factors. The computed values increase in the series Fe, Co, Ni in the same manner as do the empirical factors, but are somewhat larger. The discrepancy is however in the direction demanded by the postulate that direct exchange between adjacent d shells is always antiferromagnetic.

The original Zener theory is oversimplified, but it is important in that it drew attention to the fact that indirect exchange interactions might contribute to the internal field. The Zener mechanism for polarizing the conduction electrons by the exchange interaction with the d electrons of the paramagnetic ion considers only first order energy perturbations which lead to the physically unreasonable result of a coupling independent of distance. A more complete theory of s - d interaction has been developed by Ruderman and Kittel (1954), Kasuya (1956) and Yosida (1957). The Ruderman-Kittel-Kasuya-Yosida (RKKY) theory shows that the spin density $\rho\pm(r)$ is completely modified by the first order perturbation of the wave functions, and is of the form

$$\rho\pm(r) = \frac{n}{V} \mp \frac{1}{V}\frac{(3n)^2}{E} 2\pi J(0) N^{-1} \sum_n F(2k_m|\underline{r} - \underline{R}_n|) S_n^z \qquad (2.36)$$

where $2n$ is the number of conduction electrons in the volume V. E is the Fermi energy, and k_m is the maximum wave vector for the unpolarized state. $J(\underline{k} - \underline{k}')$ is the exchange integral between the conduction electrons and the d core spin of the paramagnetic ions. N is the number

of lattice points, $\underline{r}$ is a position vector, $\underline{R}_n$ is the position vector of the paramagnetic ions, and S_n^z is the spin operator of a paramagnetic ion with the z axis taken as the axis of spin quantization. The function F(x) oscillates and is of the form

$$F(x) = (x \cos x - \sin x)/x^4 \qquad (2.37)$$

The polarization is concentrated about the position of the paramagnetic ion, but oscillates and diminishes with distance. The periodicity of the oscillations, which correspond to ferromagnetic and antiferromagnetic coupling, depend upon the wave vector k_m and consequently the conduction electron concentration, since $n = (V/6\pi^2)k_m^3$.

The RKKY interaction has been most successful in explaining the magnetic properties of the rare earth metals, for which the experimental data clearly indicates that the exchange must be long range and oscillatory in real space. In addition, the incomplete 4f shells may be considered as highly localized inside closed outer shells.

In the transition metals the situation is not nearly so simple, as there are conflicting views as to the degree of localization of the 3d electrons. However, Yosida (1957) applied the theory with some success to some experimental results obtained on dilute Cu - Mn alloys, and Mattis (1965) has tabulated the molecular field constants expected for ordered transition metal alloys with s.c., f.c.c., and b.c.c. structures in which the magnetic atoms are sufficiently far apart for the d shell overlaps to be unimportant.

Although the exchange mechanisms so far considered are applicable to many materials, it is evident that many ordered stoichiometric

compounds exist in which it is unlikely that any of the above mechanisms are responsible for the magnetic coupling. In particular, in the transition metal oxides, the atoms that are strongly coupled antiferromagnetically are quite definitely separated by intervening, supposedly non-magnetic, oxygen ions. The accepted mechanism for exchange spin coupling in such materials was first suggested by Kramers (1934), and subsequently developed as the theory of 'Superexchange' principally by Anderson (1950, 1959, 1963).

The postulated superexchange mechanism in MnO, for example, involves the intervening O^{2-} ion. It is supposed that in the ground state the 2 p electrons on the O^{2-} ion are in identical orbitals and are consequently antiparallel. Although there is no direct overlap of Mn 3d wavefunctions there is a finite probability that a p electron will be transferred into the d shell of the magnetic ion. As the transfer could only occur into an empty d orbital the remaining p electron would be spin parallel to the full d orbits, and would interact by an assumed antiferromagnetic interaction with the Mn ion on the other side. The resulting configuration would be antiferromagnetic.

The superexchange theory developed by Anderson may only be rigorously applied to insulating compounds. Another exchange mechanism was proposed by Zener (1951), and extended by Anderson and Hasegawa (1955) and de Gennes (1960), in order to correlate the electrical conducting and magnetic properties of the mixed valency manganites of perovskite structure such as $(La_{1-x}Ca_x)(Mn^{3+}_{1-x}Mn^{4+}_x)O_3$. Compounds at the extreme ends ($x = 0,1$) are antiferromagnetic and semiconducting, but in the region

$0.2 < x < 0.4$ the conductivity is high and the materials are ferromagnetic.

The replacement of La^{3+} ions by Ca^{2+} ions results in a corresponding number of Mn^{3+} ions being replaced by Mn^{4+} ions. The migration of these Mn^{4+} ions, which is accomplished by an Mn^{4+} ion capturing an electron from a neighbouring Mn^{3+} ion gives rise to the electrical conductivity. However the actual mechanism of electron transfer is important since the Mn ions are separated by intervening O^{2-} ions. Zener in his theory of 'double exchange', postulated that the electron transfer must be through the agency of the intervening O^{2-} ion, and visualized it as a simultaneous transfer of electrons, from the Mn^{3+} ion to the O^{2-} ion, and from the O^{2-} ion to the Mn^{4+} ion on the other side. If the transfer does not change the spin of the electrons, and the intra-atomic exchange is sufficiently strong that only those configurations, where the spin of the carrier and the local ionic spin are parallel, are important, then electrons will be able to hop from one ion to the next only when the two ionic spins are not antiparallel. This obviously leads to a parallel spin coupling of the order of magnitude of the transfer integral causing the electrons' motion. Thus the conducting mixed valency manganites have ferromagnetic components and the insulating ones do not. De Gennes has shown that if the pure material is antiferromagnetic a canted arrangement is the most stable in the mixed material.

2.9 Summary

In conclusion it may be said that the mechanisms responsible for magnetic ordering are broadly understood. The superexchange mechanism is

predominant in many insulating compounds, and in the rare earth metals, where the 4f electrons are closely bound inside outer closed shells, the oscillating RKKY interaction is most appropriate. In the transition metal alloys, where the electronic structure is not so clearly defined, localized, band, and intermediate models have all been applied with varying degrees of success to the different systems.

CHAPTER 3

X-ray and neutron diffraction

3.1 The geometry of diffraction

When a beam of X-rays or neutrons is scattered by a crystal, reinforcement of the diffracted beam occurs at angles θ given by the Bragg equation

$$2d \sin\theta = m\lambda \qquad (3.1)$$

where d is the separation of the scattering planes, λ is the wavelength of the radiation, and m is the order of the reflection.

In the cubic system the separation of planes (hkl) is given by

$$d = a/(h^2 + k^2 + l^2)^{1/2} \qquad (3.2)$$

where a is the lattice parameter of the unit cell, and h, k, l are the Miller indices of the reflecting planes. Combination of equations (3.1) and (3.2) give the Bragg equation for a cubic lattice

$$\sin^2\theta = \frac{\lambda^2}{4a^2}(h^2 + k^2 + l^2) \qquad (3.3)$$

3.2 X-ray diffraction

In X-ray diffraction, the fundamental scattering mechanism is the interaction between the X-radiation and the charge of the electrons. The scattering amplitude thus increases with the atomic number of the scattering atom.

The intensity of a beam of X-rays diffracted by a cylindrical powder sample is given by the formula

$$I \propto \frac{1 + \cos^2 2\theta}{\sin\theta \sin 2\theta} jF^2A(\theta) \qquad (3.4)$$

The formula is made up of the following parts.

1. The Lorentz-polarization factor $(1 + \cos^2 2\theta)/(\sin\theta \sin 2\theta)$ contains the Lorentz factor $1/\sin 2\theta$ which is a measure of the probability that a particular plane will be in a reflecting position, and the polarization factor which arises because, although the incident beam may be unpolarized, the diffracted beam is polarized and the effect on the intensity is proportional to $(1 + \cos^2 2\theta)$. In addition, in most detecting arrangements, only a fraction proportional to $1/\sin\theta$ of the radiation scattered at an angle θ is measured.

2. The multiplicity factor j is the number of cooperating planes of the same form for the particular reflection being measured.

3. The absorption factor $A(\theta)$ is a complicated function of θ, the radius r, and the linear absorption coefficient μ of the specimen, but values have been tabulated by Bradley (1935) as functions of θ and μr.

4. The structure factor $F(hkl) = \sum_r f_r(hkl) \exp 2\pi i(hx_r + ky_r + lz_r)$, where the atomic scattering factor $f_r(hkl)$ is the ratio of the amplitude of the wave scattered by an atom to that scattered by a single electron. f is proportional to the atomic number of the scattering atom at small angles θ, but falls off as a function of $(\sin\theta)/\lambda$ due to the spatial distribution of the electrons. The calculated values are tabulated in the International Tables for X-ray Crystallography, Volume 3, together with the correction to be applied when the wavelength of the incident radiation is near an absorption edge.

At finite temperatures the atoms execute vibrations about their

equilibrium positions with the result that the atomic scattering factor is reduced by a factor $\exp(-B\sin^2\theta/\lambda^2)$, where

$$B = \frac{6h^2}{Mk\Theta}\left\{\frac{\phi(x)}{x} + \frac{1}{4}\right\} \qquad (3.5)$$

h is Planck's constant, k is Boltzmann's constant, Θ is the Debye temperature and M is the mass of the atom. $x = \Theta/T$ where T is the temperature of the crystal.

The above expression for the temperature factor only applies strictly to monatomic cubic crystals, but reasonable agreement can usually be obtained for polyatomic crystals by using a mean value for Θ. Values of Θ for the elements are tabulated in the International Tables for X-ray Crystallography, Volume 3, and the functions $\exp(-B\sin^2\theta/\lambda^2)$, and $(\phi(x)/x + 1/4)$ in Volume 2.

The amplitude and phase of the resultant wave scattered from a series of planes (hkl) is obtained from the algebraic sum of the waves scattered by the individual atoms, and is

$$F(hkl) = \sum f_r(hkl) \exp 2\pi i(hx_r + ky_r + lz_r) \qquad (3.6)$$

where x_r, y_r, and z_r, are the coordinates of the r^{th} atom, and the summation is over one unit cell.

3.3 Neutron diffraction

The wavelength λ associated with a particle of mass m and velocity v is

$$\lambda = h/mv \qquad (3.7)$$

Neutrons which have attained thermal equilibrium in a reactor at a temperature T will have a mean kinetic energy given by

$$\frac{1}{2}m\overline{v^2} = \frac{3}{2}kT \qquad (3.8)$$

where $\overline{v^2}$ is the mean square velocity.

Combination of equations (3.7) and (3.8) gives the wavelength corresponding to the root mean square velocities as

$$\lambda = h/(3mkT)^{1/2} \qquad (3.9)$$

The wavelength corresponding to 20°C is ~1.5 A, which is just the right wavelength for diffraction by crystalline solids.

The intensity of a beam of unpolarized neutrons, scattered at an angle θ by a powder sample in the form of a vertical circular cylinder fully bathed in the neutron beam, is given by the relation

$$I \propto j F^2 A(\theta)/\sin\theta \sin 2\theta \qquad (3.10)$$

The relation is identical in form to equation (3.4) for X-rays, but without the polarization factor. $A(\theta)$, the absorption factor, varies very slowly with angle, and for most materials can be ignored. The geometrical structure factor is identical to that for X-rays, but the atomic scattering factor f is replaced by the appropriate nuclear or magnetic scattering length.

3.4 Nuclear scattering of neutrons

The fundamental scattering body in nuclear scattering is the nucleus, and this leads to the immediate result that, since the dimensions of the nucleus are small compared with the wavelength of the incident thermal neutrons, the scattering is isotropic, and there is no form factor fall-off with $(\sin\theta)/\lambda$.

The neutron scattering power of a nucleus is usually expressed in terms of a scattering length b, which is determined by the boundary conditions at the surface of the nucleus. At present b cannot be

TABLE 3.1 Neutron and X-ray scattering data for the constituent elements of the Heusler alloys. (From Bacon, 1962).

Element	Atomic Number	Neutrons b (10^{-12}cm)	X-rays f_x(10^{-12}cm)
Al	13	0.35	3.65
Si	14	0.42	3.95
Ti	22	-0.34	6.2
Mn	25	-0.36	7.0
Co	27	0.25	7.6
Ni	28	1.03	7.9
Cu	29	0.79	8.2
Ga	31	0.72	8.8
Ge	32	0.84	9.0
Pd	46	0.59	12.9
In	49	0.36	13.9
Sn	50	0.61	13.9
Sb	51	0.54	14.2

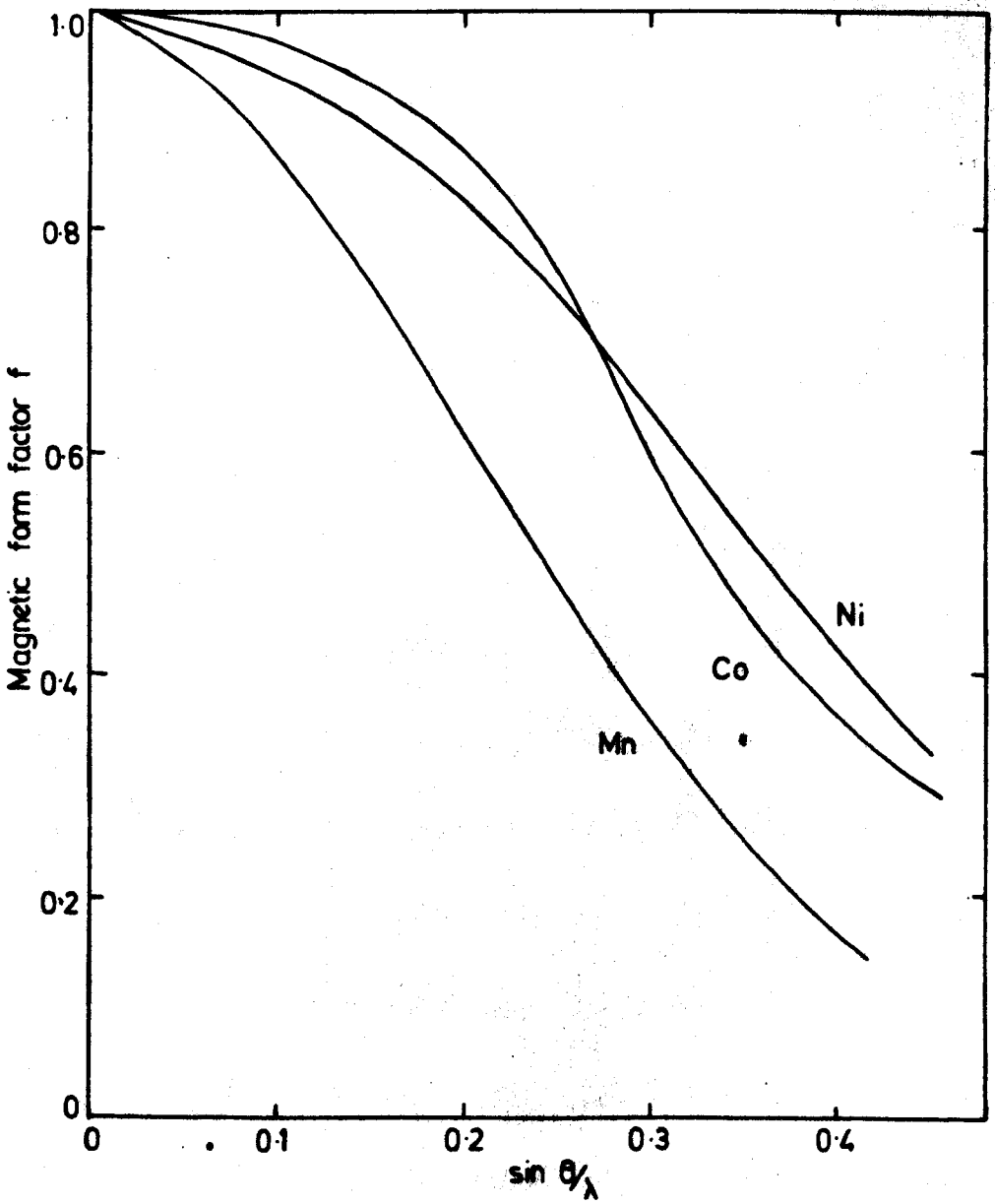

Fig. 3·1 Neutron magnetic form factors for :

Mn from Corliss, Elliott and Hastings(1956)

Co from Nathans and Paoletti (1959)

Ni from Nathans, Shull, Shirane and Andresen (1959)

calculated, but is often expressed in terms of the potential and resonance levels in the compound nucleus. The potential term is always positive, but the resonance term may take negative values. Consequently, in contrast to X-rays, b does not increase steadily with atomic number, but behaves erratically, taking both positive and negative values, and different values for different isotopes. The experimentally determined values of b for the constituent elements of the Heusler alloys are shown in table (3.1) together with the corresponding X-ray data.

The erratic behaviour of the scattering lengths has its advantages. Whereas it is difficult to distinguish between the Mn atoms and other transition metal elements by X-ray diffraction, it is particularly easy with neutrons because of the negative scattering length of Mn. This makes neutron diffraction a particularly useful technique for investigating the degree of order of Heusler type alloys.

3.5 Magnetic scattering of neutrons

In addition to its mass, a neutron possesses a spin 1/2, and a magnetic moment of 1.9 nuclear magnetons. The interaction of this moment with that of a magnetic atom produces an additional magnetic scattering of the neutron. Since the magnetic scattering is due to the unpaired electrons, and not the nucleus, the magnetic scattering amplitude, p, exhibits a form factor fall-off with $(\sin\theta)/\lambda$. The magnetic form factors used for Mn, Co, and Ni are shown in figure (3.1).

Halpern and Johnson (1939) have shown that randomly oriented paramagnetic ions have a differential magnetic scattering cross-section $d\sigma_{pm}$ per atom given by

$$d\sigma_{pm} = \frac{2}{3} S(S+1)\left(\frac{e^2\gamma}{mc^2}\right)^2 f^2 \qquad (3.11)$$

where S is the spin quantum number of the scattering atom, e and m are the electronic charge and mass respectively, c is the velocity of light, γ is the magnetic moment of the neutron in nuclear magnetons, and f is the magnetic form factor.

Since the paramagnetic atoms are randomly oriented, the magnetic scattering is entirely incoherent and adds to the background of the powder diffraction pattern. In ordered magnetic materials the magnetic moments are oriented in a regular manner, and the differential magnetic scattering cross-section per ordered atom is given by

$$d\sigma_m = q^2 S^2 (e^2\gamma/mc^2)^2 . f^2 \qquad (3.12)$$

where $\underline{q}$ is the magnetic interaction vector defined by

$$\underline{q} = \underline{\varepsilon}(\underline{\varepsilon} \cdot \underline{\mu}) - \underline{\mu} \qquad (3.13)$$

$\underline{\varepsilon}$ is a unit scattering vector normal to the reflecting planes, and $\underline{\mu}$ is a unit vector in the direction of the magnetic moment.

The magnetic scattering amplitude p is defined as

$$p = (e^2\gamma/mc^2)Sf \qquad (3.14)$$

and hence equation (3.12) may be rewritten

$$d\sigma_m = q^2 p^2 \qquad (3.15)$$

Halpern and Johnson have shown that there is no coherence between magnetic and nuclear scattering of unpolarized neutrons and the total scattering cross-section $d\sigma$ is thus

$$d\sigma = b^2 + q^2 p^2 \qquad (3.16)$$

i.e., the intensities are added.

The total scattered intensity for any reflection is obtained by calculating the total structure factor F for the unit cell. The nuclear structure factor F_n is given by

$$F_n = \sum_r b_r \exp 2\pi i(hx_r + ky_r + lz_r) \qquad (3.17)$$

and the magnetic structure factor F_m by

$$F_m = \sum_r p_r \exp 2\pi i(hx_r + ky_r + lz_r) \qquad (3.18)$$

The resultant intensity is proportional to F^2 which is given by

$$F^2 = F_n^2 + q^2 F_m^2 \qquad (3.19)$$

Now from equation (3.13),

$$q^2 = 1 - (\underline{\varepsilon} \cdot \underline{\gamma})^2 = \sin^2\alpha \qquad (3.20)$$

where α is the angle between $\underline{\varepsilon}$ and $\underline{\gamma}$. Thus if q^2 is known for a particular reflection, the orientation of the magnetic moments may in principle be determined. However, for polycrystalline materials only a mean value of q^2 from all reflecting planes of the same form is obtained, and the most that can be calculated is the orientation of the moments with respect to the unique axis. If no unique axis exists, as in a cubic crystal for example, it is impossible to determine the moment orientations from measurements on polycrystalline samples using unpolarized neutrons.

In antiferromagnetic materials the magnetic unit cell is usually twice the size of the chemical unit cell, and consequently the magnetic and nuclear diffraction peaks are not superimposed, but in ferromagnetic

materials the magnetic and chemical unit cells are usually the same size and the magnetic and nuclear peaks are superimposed at the same Bragg angle. The magnetic and nuclear contributions to the diffraction peaks may be determined by three methods. The best method is to vary q^2. This may be done by applying a magnetic field, sufficiently large to saturate the sample, along or perpendicular to the scattering vector. In the first case $q^2 = 0$, and in the second $q^2 = 1$, and the difference between the two diffraction patterns is the magnetic scattering. If suitable magnetic fields are not available measurements may be made above and below the Curie temperature, but this method suffers from the disadvantage that other parameters may change with temperature, and corrections have to be applied. The third method is to compare the intensities of diffraction lines at low and high angles. At low angles the magnetic contribution may be large, but there is a rapid fall off in magnetic contribution with angle due to the magnetic form factor, and high angle lines have virtually no magnetic component. The disadvantage of this method is that intensities cannot be measured as accurately at high angles.

3.6 Magnetic scattering by spiral spin systems

The previous discussions have been concerned with magnetic scattering from ferromagnetic or antiferromagnetic materials in which all the magnetic atoms are aligned positively or negatively along a single direction. However, it has been shown by neutron diffraction studies that other more complicated ordered arrangements can occur. In particular, spiral spin arrangements, in which the magnetic moments in

successive planes are rotated through angles other than multiples of 180°, are observed.

In order to predict the magnetic scattering due to the additional moment orientations it is necessary to generalize equation (3.18) and to define a complex structure factor $\underline{F}_m$, where

$$\underline{F}_m(hkl) = \sum_r p_r \underline{q}_r \exp 2\pi i(hx_r + ky_r + lz_r) \qquad (3.21)$$

where $\underline{q}_r$ is the magnetic interaction vector for the r^{th} atom. Replacing $\underline{q}_r$ by the full vector expression of equation (3.13), and substituting in (3.21) gives

$$\underline{F}_m(hkl) = \sum_r p_r(\underline{\epsilon}(\underline{\epsilon} \cdot \underline{\nu}_r) - \underline{\nu}_r) \exp 2\pi i(hx_r + ky_r + lz_r) \qquad (3.22)$$

The positions and intensities of the magnetic reflections resulting from a particular spiral spin system may be calculated by substituting the appropriate values in equation (3.22) and carrying out the summation.

There are many possible spiral spin configurations, three of which are illustrated in figure (3.2), but the neutron diffraction patterns arising from them are characterized by the appearance of pairs of satellite magnetic reflections about the conventional Bragg positions.

For a simple screw spiral such as is illustrated in figure (3.2a), with the magnetic vector rotating about the [uvw] axis through an angle ϕ from one plane to the next, satellites to the Bragg reflection (hkl) occur at angles corresponding to the generally non-integral indices $(h \pm u\Delta, k \pm v\Delta, l \pm w\Delta)$, where $\Delta = \phi/2\pi$.

If there is only one type of magnetic atom (i.e. $p_r = p$), then the intensities of the normal ferromagnetic or antiferromagnetic Bragg reflections are proportional to q^2p^2, with q^2 given by equation (3.20).

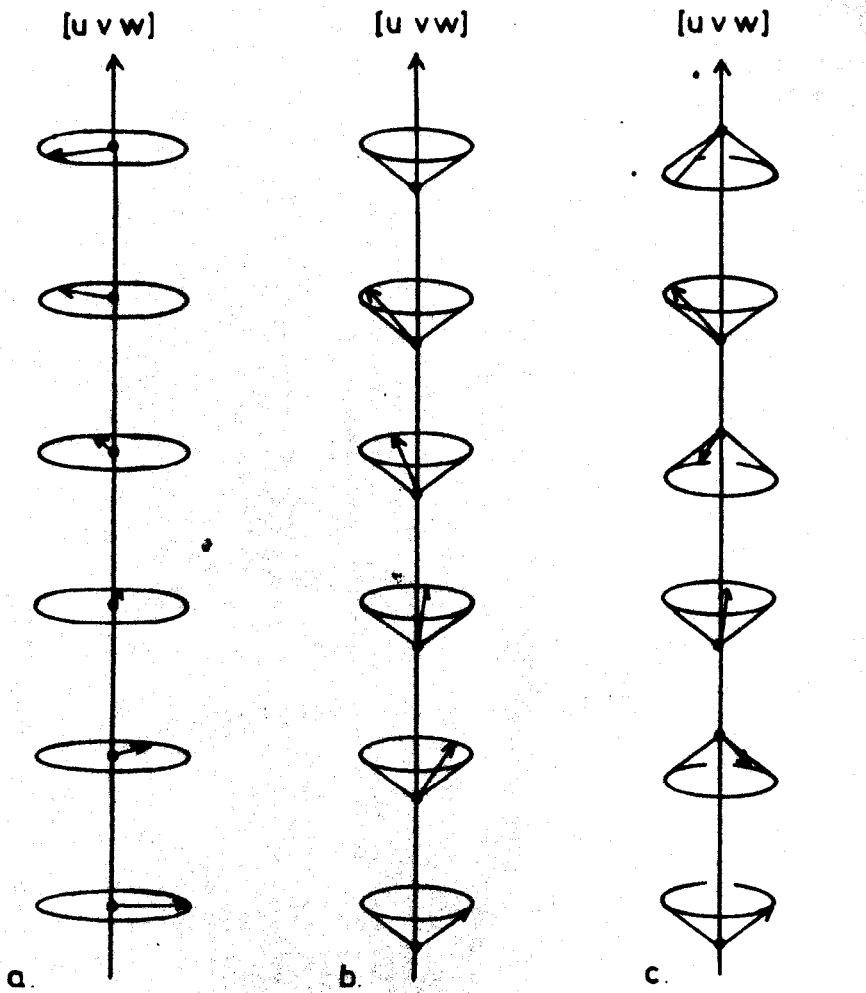

Fig 3.2 Spiral spin configurations

For a spiral spin configuration q^2 is replaced by a mean value averaged over all values of $\underline{q}_r$ of magnitude

$$\overline{q^2} = (1 + \cos^2\eta)/4 \qquad (3.23)$$

where η is the angle between the spiral axis and the scattering vector.

3.7 The structure factors for a Heusler alloy

The chemical structure of the Heusler alloys is shown in figure (1.2). It is best considered as comprising 4 interpenetrating f.c.c. sublattices A,B,C,D with coordinates (0 0 0), (1/4 1/4 1/4), (1/2 1/2 1/2) and (3/4 3/4 3/4) respectively, as in figure (1.1). The structure factor for 4 such interpenetrating sublattices is non-zero when the Miller indices of the reflecting planes are either all odd, or all even. The even planes may be divided into 2 groups, $(h + k + 1)/2$ odd, and $(h + k + 1)/2$ even. The generalized structure factors for the 3 groups are then

$$\left.\begin{array}{lll} \text{All odd} & F(111) = \left|4\left\{(f_A - f_C)^2 + (f_B - f_D)^2\right\}^{1/2}\right| \\ (h + k + 1)/2 \text{ odd} & F(200) = \left|4(f_A - f_B + f_C - f_D)\right| \\ (h + k + 1)/2 \text{ even} & F(220) = \left|4(f_A + f_B + f_C + f_D)\right| \end{array}\right\} \qquad (3.24)$$

where f_A, f_B, f_C, and f_D are the atomic scattering factors for the atoms on the respective sublattices.

F(111) and F(200) contain difference terms and correspond to the order dependent superlattice lines. F(220) is the sum of the constituent scattering factors and is independent of order. As we shall only be concerned with relative intensities, the factors x4 may be neglected.

The structure factors for an ordered Heusler alloy, X_2YZ, thus

become

$$\left.\begin{aligned} F(111) &= \left| f_Y - f_Z \right| \\ F(200) &= \left| 2f_X - (f_Y + f_Z) \right| \\ F(220) &= \left| 2f_X + f_Y + f_Z \right| \end{aligned}\right\} \quad (3.25)$$

3.8 The structure factors for a Cl_b type alloy

In addition to the Heusler alloys with the composition X_2YZ, another series of alloys at the composition XYZ has been investigated. These alloys have a structure very similar to that of the Heusler alloys, but with one sublattice vacant. The structure is illustrated in figure (3.3). The structure factors may be obtained from equation (3.24) by substituting $f_C = 0$. Hence

$$\left.\begin{aligned} F(111) &= \left| \left(f_X^2 + (f_Y - f_Z)^2 \right)^{1/2} \right| \\ F(200) &= \left| f_X - (f_Y + f_Z) \right| \\ F(220) &= \left| f_X + f_Y + f_Z \right| \end{aligned}\right\} \quad (3.26)$$

3.9 Order-disorder in ternary alloys

The state of long-range order of a binary alloy AB is conveniently described in terms of a long-range order parameter S, where

$$S = \frac{\text{(No. of A atoms on sublattice A) - (No. of A atoms on sublattice A when randomly ordered)}}{\text{(No. of A atoms on sublattice A when fully ordered) - (No. of A atoms on sublattice A when randomly ordered)}}$$

S defined in this manner is a useful parameter in that it is possible to infer, with some quantitative precision, some of the important features of the configurational state to which it is appropriate. In particular, the intensities of the superlattice lines are proportional

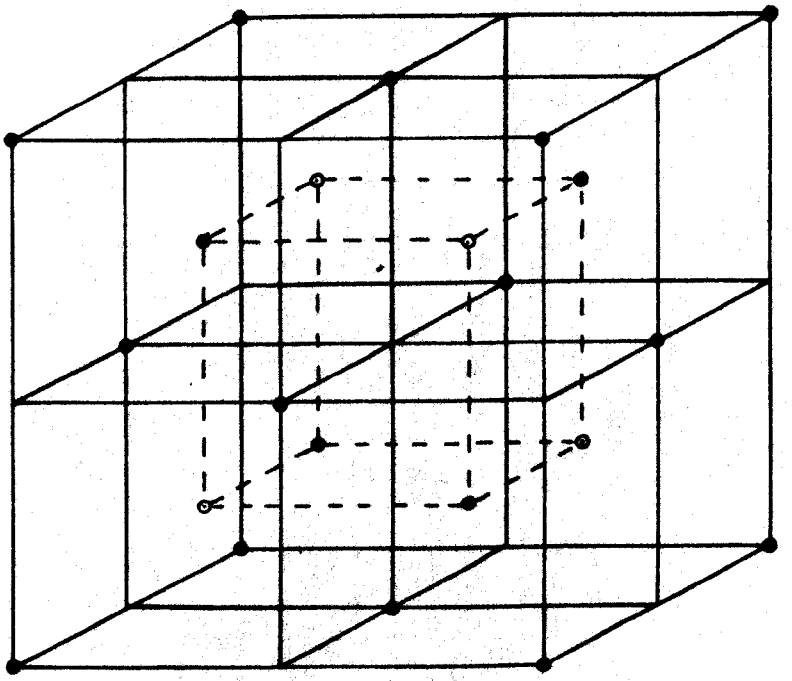

Fig. 3·3 The Cl_b Structure

to S^2.

It is not possible to describe the state of order of a ternary alloy with only one order parameter except in the particular case when the disorder is perfectly random. In practice, energy considerations often dictate that the probability of one type of atom disordering is not equal to that of another, and then a set of ordering parameters is required. Unfortunately, their determination from superlattice line intensity measurements is usually difficult and ambiguous. A limited but infommative solution may be obtained by considering only a restricted number of ways in which the alloy is likely to disorder. Table (3.2) illustrates seven such ways in which an alloy with the Heusler composition X_2YZ might be arranged on 4 interpenetrating f.c.c. sublattices. α, the 'Disordering parameter' is the fraction of either Y or Z atoms not on their correct sublattices.

(1) is the arrangement of atoms in the ordered Heusler structure.

(2) and (4) represent a state of disorder between only one X sublattice and the Y or Z sublattice respectively. As disorder of this type proceeds the initial state of order is replaced by another state of order, represented by $\alpha(2,4) = 1$, with X atoms on A and B sublattices say, and Y and Z atoms on C and D respectively. This structure is illustrated in figure (1.1), structure (2).

(3) and (5) represent the atomic arrangements to be expected if disorder occurs between any of the X atoms and either of the Y or Z atoms respectively. Maximum disorder of this form occurs at $\alpha(3,5) = 0.75$, but again this is order of another form, the DO_3 (Fe_3Al type) structure.

TABLE 3.2 The arrangements of the atoms of an alloy X_2YZ on 4 interpenetrating f.c.c. sublattices A, B, C, D, for the principal idealized types of disorder. (The disordering parameter α is the fraction of either Y or Z atoms not on their correct sublattices.)

Type of disorder	Sublattice A	Sublattice B	Sublattice C	Sublattice D
1. Complete order	X	Y	X	Z
2. (X - Y) disorder	$(1-\alpha)X + \alpha Y$	$(1-\alpha)Y + \alpha X$	X	Z
3. (X-Y-X) disorder	$(1-\frac{\alpha}{2})X + \frac{\alpha}{2}Y$	$(1-\alpha)Y + \alpha X$	$(1-\frac{\alpha}{2})X + \frac{\alpha}{2}Y$	Z
4. (X - Z) disorder	$(1-\alpha)X + \alpha Z$	Y	X	$(1-\alpha)Z + \alpha X$
5. (X-Z-X) disorder	$(1-\frac{\alpha}{2})X + \frac{\alpha}{2}Z$	Y	$(1-\frac{\alpha}{2})X + \frac{\alpha}{2}Z$	$(1-\alpha)Z + \alpha X$
6. (Y - Z) disorder	X	$(1-\alpha)Y + \alpha Z$	X	$(1-\alpha)Z + \alpha Y$
7. (X-Y-X-Z) disorder	$(1-\frac{2}{3}\alpha)X + \frac{\alpha}{3}(Y+Z)$	$(1-\alpha)Y + \frac{\alpha}{3}(2X+Z)$	$(1-\frac{2}{3}\alpha)X + \frac{\alpha}{3}(Y+Z)$	$(1-\alpha)Z + \frac{\alpha}{3}(2X+Y)$

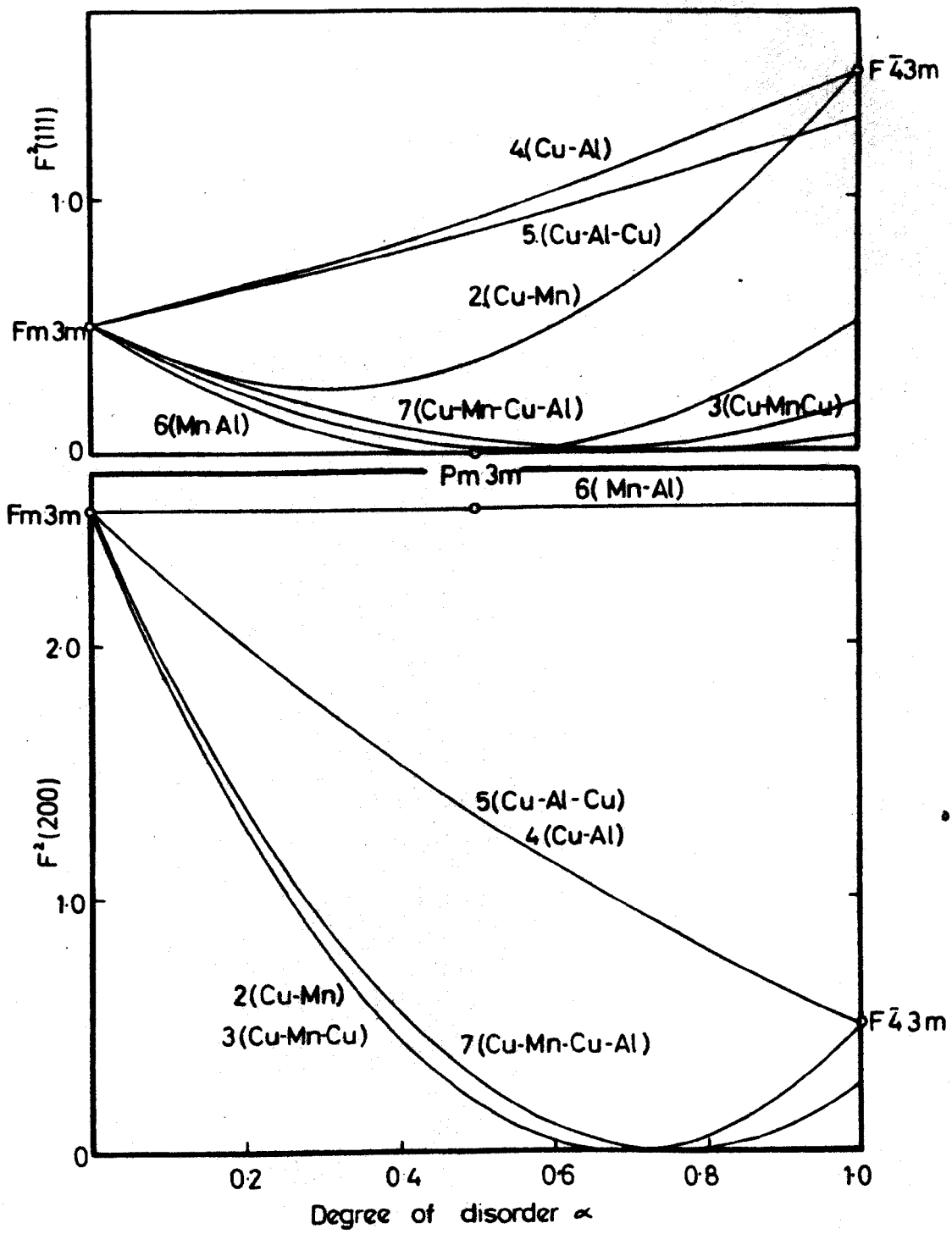

Fig. 3·4 Neutron diffraction structure factor $(F)^2$ for Cu_2MnAl versus degree of disorder α

(6) is the atomic arrangement when disorder occurs between the Y and Z atoms only. Maximum disorder of this form occurs at $\alpha(6) = 0.5$ and corresponds to the ordered B2 (CsCl type) structure.

(7) represents random disorder. Complete disorder, $S = 0$, occurs at $\alpha(7) = 0.75$.

The effects of the various types of disorder on the nuclear superlattice line intensities of Cu_2MnAl are shown in figure (3.4). It is of interest to note that, in marked contrast to binary alloys, disorder can occur in such a manner as to result in an increase in intensity of either the odd or even superlattice lines.

It is found that in general one of the above types of disorder predominates in alloys at the Heusler composition, and the state of order can usually be satisfactorily described in terms of some degree of preferential disorder, together with a small amount of random disorder. The type of order that predominates, if any, is usually clear from graphs of F^2 versus α. In particular, disorder of type (6) which often occurs in alloys containing Al, Ga, or In is easily recognized as it only affects the odd superlattice lines. A comparison of neutron diffraction, and X-ray diffraction data is usually sufficient to determine unambiguously the state of order in a Heusler alloy.

The determination of the state of order of the Cl_b type alloys is usually more complex since they are effectively quaternary alloys with with 3 types of atoms and one vacancy distributed on 4 sublattices. In addition, there are 3 possible ways in which the atoms may be arranged in the Cl_b structure. The 3 possibilities are shown in table (3.3).

However, provided the state of order is high, it is possible to distinguish between the 3 ordered configurations and to determine with some confidence the type of disorder present.

TABLE 3.3 The 3 possible arrangements of an alloy XYZ on 4 interpenetrating f,c.c. sublattices A, B, C, D, assuming that one sublattice (C say) is vacant, and there is no disorder.

	Sublattice A	Sublattice B	Sublattice C	Sublattice D
1.	X	Y	-	Z
2.	Y	Z	-	X
3.	Z	X	-	Y

CHAPTER 4

Experimental techniques

4.1 Alloy preparation

All the alloys were prepared in an essentially similar manner from spectrographically pure elements supplied by Johnson Matthey & Co. Ltd. The 5, 10, or 20 g ingots were made by melting the constituent elements together in the appropriate proportions in an argon arc furnace. After the initial melt the alloys were turned over and remelted 3 times, whenever possible, in order to ensure good mixing. Because on occasions the alloys were very brittle and shattered on remelting the first melt was always mixed as thoroughly as possible. Care was always taken to minimize any loss by vaporization. When the boiling point of one constituent was lower than the melting point of another, as is that of Sb below that of Pd or Co, half of the Mn was first melted with the Sb, and the rest with the Pd or Co. The two halves were then melted together with minimal loss of material. Ingots were inspected and weighed after removal from the furnace, and if for any reason any undue oxidation or change in weight had occurred, the melt was discarded.

The densities of the ingots were measured, and then the ingots were crushed. About four large pieces were ground down into roughly ellipsoidal ring-balance specimens approximately 3.5 mm long by 1.6 mm diameter. The remainders were crushed to powders in a hardened steel mortar. A ring-balance specimen and small amounts of powder were sealed off under

vacuum in two small quartz tubes. The samples were annealed for at least 24 hours at temperatures between 500°C and 1000°C depending upon the alloy. One sample was quenched into iced water, and the other was slow-cooled to room temperature, usually over 36 hours. X-ray photographs were taken of powder samples before annealing, after quenching, and after slow-cooling, and any changes noted. The photographs taken before annealing were always to some extent blurred due to the severe cold working needed to produce the powder, but the principal lines could usually be distinguished. The intensities and positions of the lines on the photographs were compared with those calculated for a Heusler alloy of that composition and density. If one or all of the photographs appeared to indicate a Heusler alloy type structure, the rest of the sample was sealed off under vacuum and given a similar heat treatment.

4.2 Structural analysis

The structures of the alloys were initially investigated using X-ray diffraction techniques. For most of the work a standard 9 cm Unicam Debye-Scherrer camera was used.

A glass fibre of about 100 microns radius was coated with a thin layer of Canada balsam and evenly covered with a thin layer of the finest fraction of the powder. The specimen was mounted on the rotator at the geometrical centre of the camera, and an X-ray diffraction photograph was taken using Ilford G industrial X-ray film in a van Arkel mounting. Iron radiation, with a manganese beta filter, was usually used in order to avoid fluorescence. The Bragg angles of the lines were

determined from measurements of the positions of the lines using a Cambridge Universal measuring machine. Lattice parameters were determined accurately from Nelson-Riley extrapolations of a_0 versus $\frac{1}{2}(\cos^2\theta/\sin\theta + \cos^2\theta/\theta)$. Line intensities were estimated visually or were measured on a Joyce-Loebel micro-densitometer, depending upon the accuracy required. If the superlattice lines were expected to be very weak, photographs were taken using a Philips 11.46 cm powder camera with fine collimation.

Low temperature powder photographs were taken using a Philips camera modified by Dr. F. H. Combley through which vapour, from a freely boiling liquid nitrogen container, could be passed at various rates. The temperature was measured using a thermocouple close to the specimen.

Accurate determinations of the magnetic and chemical structures of the alloys, including qualitative estimates of degrees of order were made using neutron diffraction techniques.

Neutron diffraction facilities were provided on the DIDO high flux reactor at A.E.R.E., Harwell, by arrangement with Professor G. E. Bacon. Some initial work was done on the small BADGER diffractometer, but most of the results were obtained on the larger high resolution CURRAN diffractometer shown diagrammatically in figure (4.1).

The collimated beam of slow neutrons falls on the monochromating crystal, and the monochromated beam is channelled through the shielding to the centre of the spectrometer table. The emergent beam has a wavelength of 1.056 A, and is of rectangular cross-section approximately $1\frac{1}{2}$" x $\frac{1}{2}$". The intensity of the diffracted beam scattered by the specimen is measured by the B^{10} enriched BF_3 proportional counter.

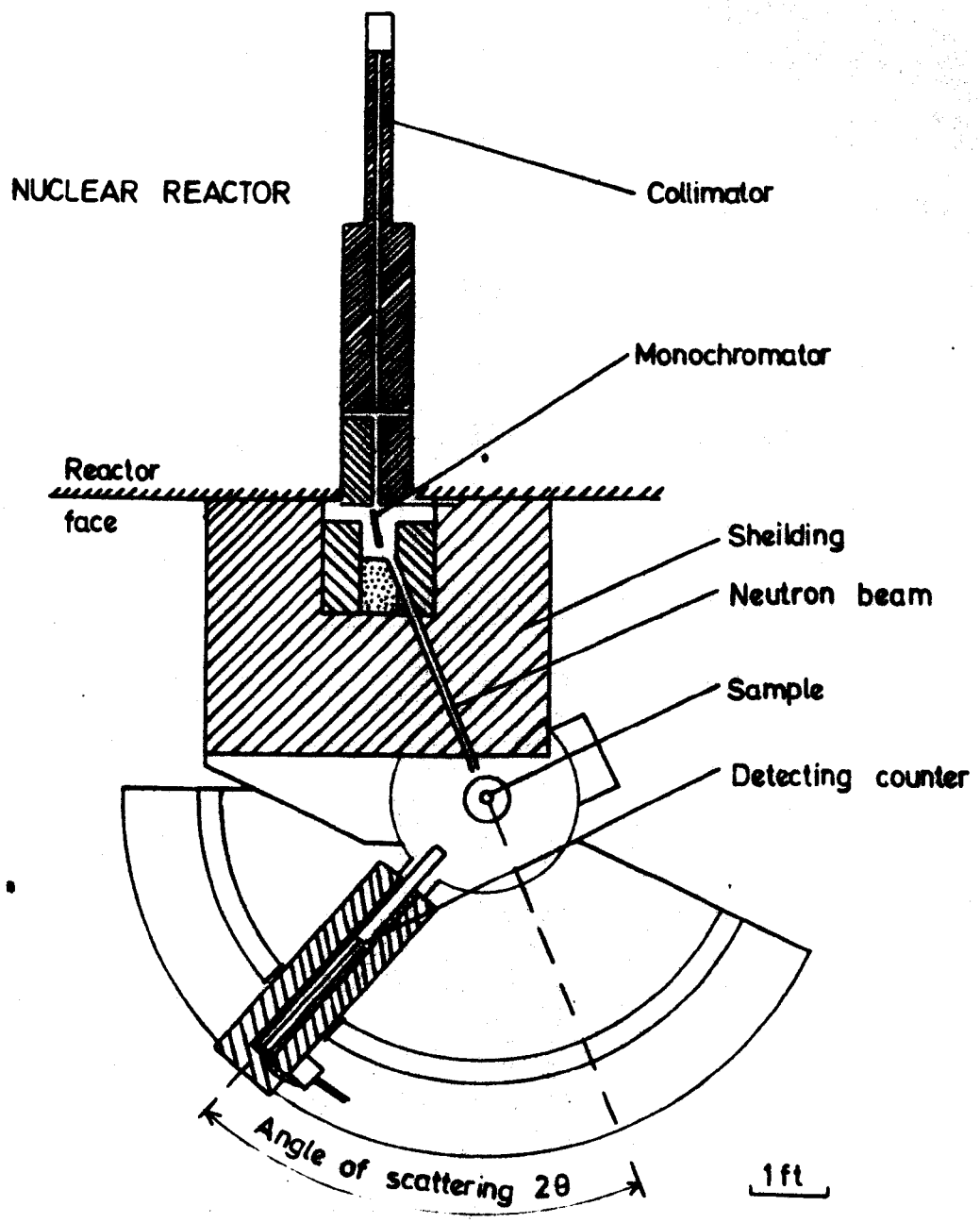

Fig. 4·1 The general layout of the Curran spectrometer at the Harwell reactor DIDO showing some details of the collimator and shielding (Bacon 1962)

The counter rotates in a horizontal plane about a vertical axis through the centre of the sprectometer table, and is programmed to count at a fixed position until a preset monitor count is reached. The counter then steps round through a small predetermined angle and then repeats the count. The procedure is continued until a preset terminating angle is reached. The counting is automatic and is recorded, together with the counter angle and temperature, on a digital print out. A typical monitor count is of the order of 4×10^6 neutrons at intervals of $1/5^\circ$.

The specimens were in the form of powders which were enclosed in thin walled cylindrical cans. The initial work was done in copper cans since the cryostat used had copper and stainless steel tails, but this had the grave disadvantage that the (111) line of Cu usually fell on, or close to, the (220) normalizing line of the alloy. When a vanadium tailed cryostat and vanadium walled furnace became available the work was done in titanium-zirconium null-matrix cans. Room temperature and furnace runs were done in large cans approx. 3.8 cm x 1 cm diam., with a sample volume approx. 3 cm^3. Cryostat runs were done in smaller cans approx. 1 cm^3 volume.

The furnace consisted of a simple electric heater fitted with a cylindrical vanadium heat shield which encircled the specimen. Temperatures up to $150^\circ C$ could be readily achieved.

The cryostat was constructed for use at liquid helium temperature, but was equally suitable for use at liquid nitrogen temperature. The specimen was attached to the end of a thick copper rod which was in good thermal contact with the bottom of the innermost coolant container.

Three sets of vanadium radiation shields encircled the specimen which quickly attained the temperature of the coolant. If it was necessary to compare room and low temperature diffraction patterns, the room temperature run was done in the empty cryostat. The coolant was then introduced without moving the cryostat. This enabled almost direct comparisons to be made since the specimen remained in exactly the same position and, apart from the temperature, the physical environment of the specimen was unchanged.

Unfortunately there were no facilities available for applying a saturating magnetic field to the specimens, so magnetic structure determinations were usually made by comparison of the diffraction patterns above and below the ordering temperature. In some of the alloys, particularly those containing cobalt, the Curie temperatures were too high to permit this, and the magnetic and chemical structures had to be deduced from room temperature data only. Fortunately, in most cases, both the magnetic and nuclear structure factors were such as to make this method quite accurate.

4.3 Magnetic measurements

The magnetic properties of the alloys investigated were very varied, and two Sucksmith ring-balances were found to be the most suitable measuring instruments.

Magnetization measurements were made on the ferromagnetic alloys at 11 applied fields up to 16000 Oe, over a temperature range 77°K to approx. 1000°K, using a ring-balance basically as described by Sucksmith (1939).

The susceptibilities of paramagnetic and antiferromagnetic alloys were measured at 3 applied fields, 3430, 7030, and 9900 Oe, over the temperature range 77°K to approx 520°K, using a 'paramagnetic' ring-balance as described by Sucksmith (1929).

Both balances are essentially similar, and depend for their operation upon the measurement of the force F_z exerted upon a specimen of magnetic moment M in a non-uniform magnetic field. F_z is related to the vertical field gradient by the equation

$$F_z = M \frac{\partial H}{\partial z} \qquad (4.1)$$

For a ferromagnetic specimen of mass m, and specific magnetization σ_{HT}, the equation becomes

$$F_z = m\sigma_{HT} \frac{\partial H}{\partial z} \qquad (4.2)$$

and for a paramagnetic material of susceptibility χ, it may be written

$$F_z = m\chi H \frac{\partial H}{\partial z} \qquad (4.3)$$

Because of the difficulty of measuring $\frac{\partial H}{\partial z}$ accurately both instruments are calibrated using pure materials of known magnetization or susceptibility. A small, approximately ellipsoidal, specimen of spectrographically pure iron is used to calibrate the ferromagnetic balance, and a cylindrical sample of spectrographically pure palladium for the paramagnetic balance.

In order to ensure that the calibration is valid for all specimens, ferromagnetic measurements must be made in a region of the field where the gradient $\frac{\partial H}{\partial z}$ is constant and the change in absolute value of the field is small. This is achieved by situating the specimen at the centre of the magnet pole-pieces that have been stepped as in figure (4.2a).

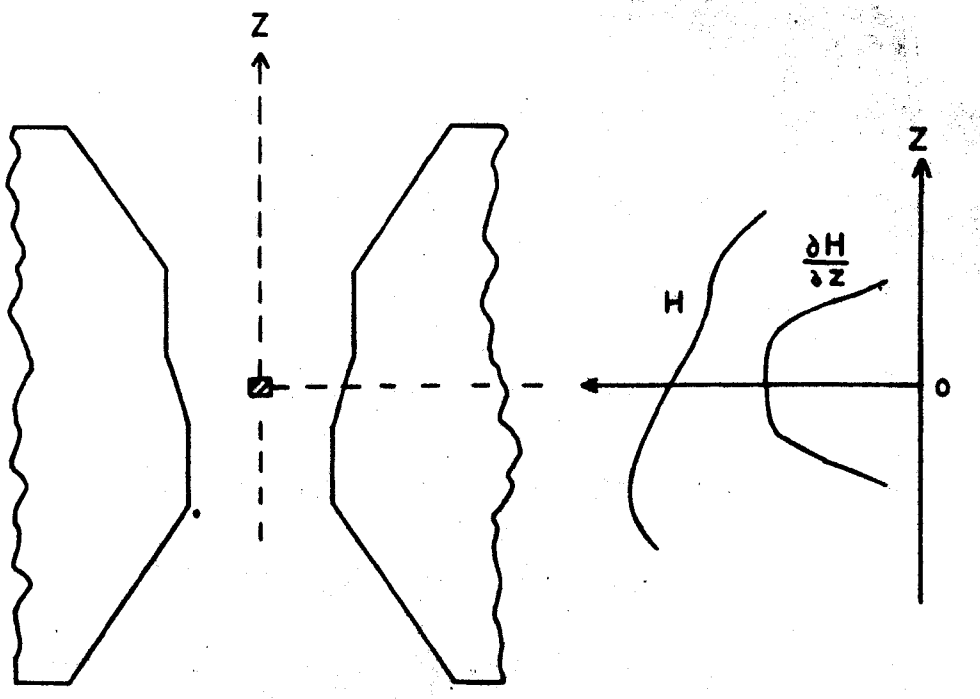

a. Pole-tips and magnetic field for ferromagnetic measurements.

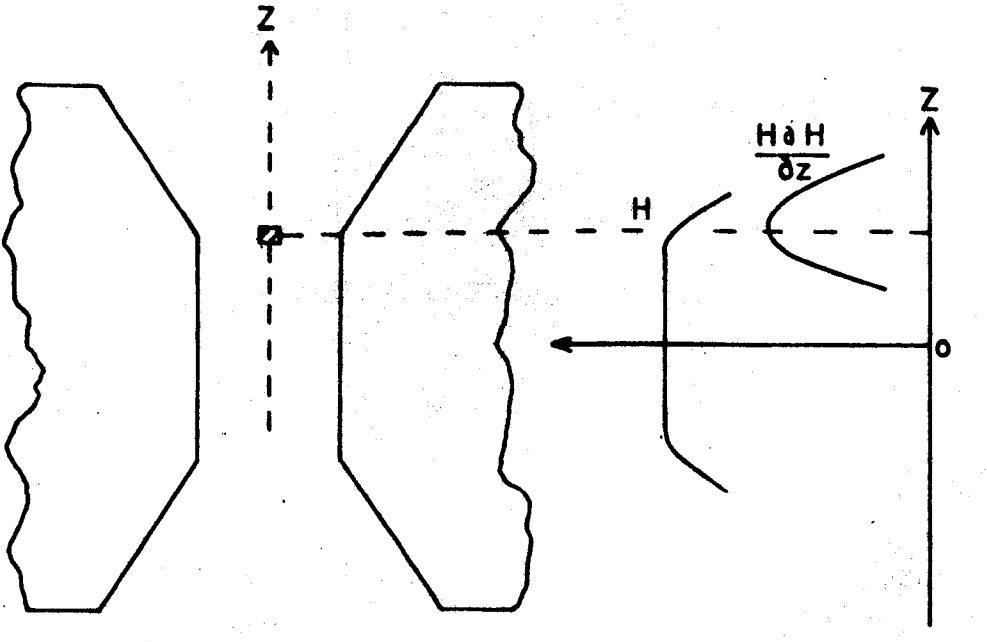

b. Pole-tips and magnetic field for susceptibility measurements

Fig. 4·2

The centre sections of the pole-pieces are inclined at approx. 5° to the vertical, giving a small, effectively uniform field gradient over the volume of the specimen.

In order to be able to compare susceptibilities directly, the specimen must be in a region of the field where $H\frac{\partial H}{\partial z}$ is constant. As the materials to be investigated have small and substantially field independent susceptibilities a region over which there is a steep field gradient may be used. A suitable position is shown in figure (4.2b).

The force F_z exerted on the specimen is measured by the deformation produced in a ring of beryllium-copper strip, supported at the top, and subject to the force at the bottom. The experimental arrangement is shown in figure (4.3).

The angle turned through by a tangent to the ring is, to a first approximation, given by the equation

$$\phi = F_z r^2 \theta \cos\theta / 4EI \qquad (4.4)$$

where r is the radius of the ring, I is its moment of inertia of cross-section, and E is Young's modulus. θ is the angle between the tangent and the vertical. A maximum in ϕ occurs at about $\theta = 49^{\circ}$ when

$$\phi_m = 0.140 r^2 F_z / EI \qquad (4.5)$$

Plane mirrors are fixed at the positions $\theta = 49^{\circ}$, and the ring distortion is measured using an optical lever.

4.4 The electromagnets

The magnetic fields necessary to produce saturation in the ferromagnetic materials, and sufficiently large field gradients to enable the susceptibility of non-ferromagnetic materials to be measured, were produced

by 4" electromagnets designed by Sucksmith and Anderson (1956). Energising currents of up to 13 amps were supplied via a Westinghouse rectifier from a 3-phase Variac controlled supply. The pole-tips were in the form of truncated cones tapering to approx. 3.5 cm, with a cone angle 57°. The pole-gap was approx. 2 cm.

The magnet was mounted on an adjustable tripod base, and the whole assembly could be moved horizontally along a track, in order to facilitate adjustment and specimen changing.

4.5 The ring-balances

The ferromagnetic balance consisted of a circular ring, approx. 5 cm diam., of beryllium-copper strip 3 mm wide x·2 mm thick, supported in a vertical plane at its highest point. A quartz tube approx. 30 cm x 2 mm diam. was attached vertically to the lowest part of the ring. A copper specimen holder was attached to the bottom end of the rod with Autostic adhesive. Lateral constraint was provided by the 2 flat spirals, S, which prevented the specimen from being pulled sideways without affecting the linearity of the relationship between image displacement and applied force. Light from a distant straight filament lamp was reflected by the 2 mirrors, and focussed by the lens L to an image in the focal plane of a travelling microscope capable of vertical traverse, and measuring to 0.01 mm. The ring assembly was enclosed in an airtight glass dome with optically flat windows, enabling the whole system to be evacuated. Damping was provided by light vanes dipping into silicone vacuum oil.

The paramagnetic balance differed from the ferromagnetic balance in

that it was required to measure much smaller forces. The ring was 0.1 mm thick, and thinner spirals were used. The rod was made from light German silver tube, but the weight was still such as to cause excessive distortion of the ring. Increased damping was achieved by making the damping 'vanes' in the form of light hollow drums. The large surface area provided the additional damping, and the upthrust reduced the ring distortion without adding to the rigidity of the system.

4.6 Temperature control

Temperatures between 77°K and room temperature were obtained using a low temperature attachment devised by Crangle and Martin (1959). The arrangement is shown in figure (4.4). It consists of 2 co-axial tubes, closed at their ends, and capable of evacuation. The outer tube is of thin walled German silver tube, and in operation is immersed in the shaped Dewar vessel which is normally filled with liquid nitrogen. The inner tube is of thin walled German silver tube down to the point Y, where it is joined to the copper bottom. A small heater is set inside the copper bottom, and a controlled heat leak is provided by the copper bridge at X. The space between the 2 tubes is normally evacuated. Helium exchange gas is contained in the inner container enabling the specimen at Z to achieve almost the same temperature as the copper bottom. Temperature control is achieved by balancing the heat input from the heater against the controlled leak through the bridge.

High temperature measurements, up to 1000°K, were carried out under vacuum in the narrow cylindrical water-cooled furnace illustrated in figure (4.5). The inner quartz tube, internal diameter 8 mm, carries

windings of nichrome strip, closely wound over the specimen region. The strip is firmly attached with Autostic cement, and is insulated from the brass water jacket with asbestos paper. The heat capacity of the furnace is small, enabling equilibrium temperatures to be attained with rapidity. A temperature of 1000°K could be maintained with a heat input of approx. 50 watts. Additional water cooling is provided on the main body of the ring balance to prevent heat from reaching the spirals.

The paramagnetic balance incorporated a 'Pallador' thermocouple, electrically insulated in fine quartz tubes threaded down the balance rod. The measuring junction was adjacent to the specimen, and the fixed junction was in melting ice. Pallador was used because of its small susceptibility, and large thermal e.m.f. over the range 77°K to approx. 520°K. The thermocouple e.m.f. was measured using a Tinsley potentiometer coupled to a Pye Scalamp galvanometer. Susceptibility measurements were made at only 3 field values, and the temperature could be kept steady to within 1° over the short time necessary.

A chromel-constantan thermocouple was used in the ferromagnetic balance as neither of the constituents are ferromagnetic, and it gives a large thermal e.m.f. over the range 77°K to above 1000°K. As magnetization measurements were made at 11 applied fields, the temperature had to be held steady for about 5 minutes. This was achieved by fine manual adjustment of the heater current, with the thermocouple e.m.f. displayed on a 0 - 10 mV pen recorder. When potentials above 10 mV were being measured, potentials in steps of 10 mV were backed off using a Tinsley potentiometer, and only the difference was displayed on the recorder.

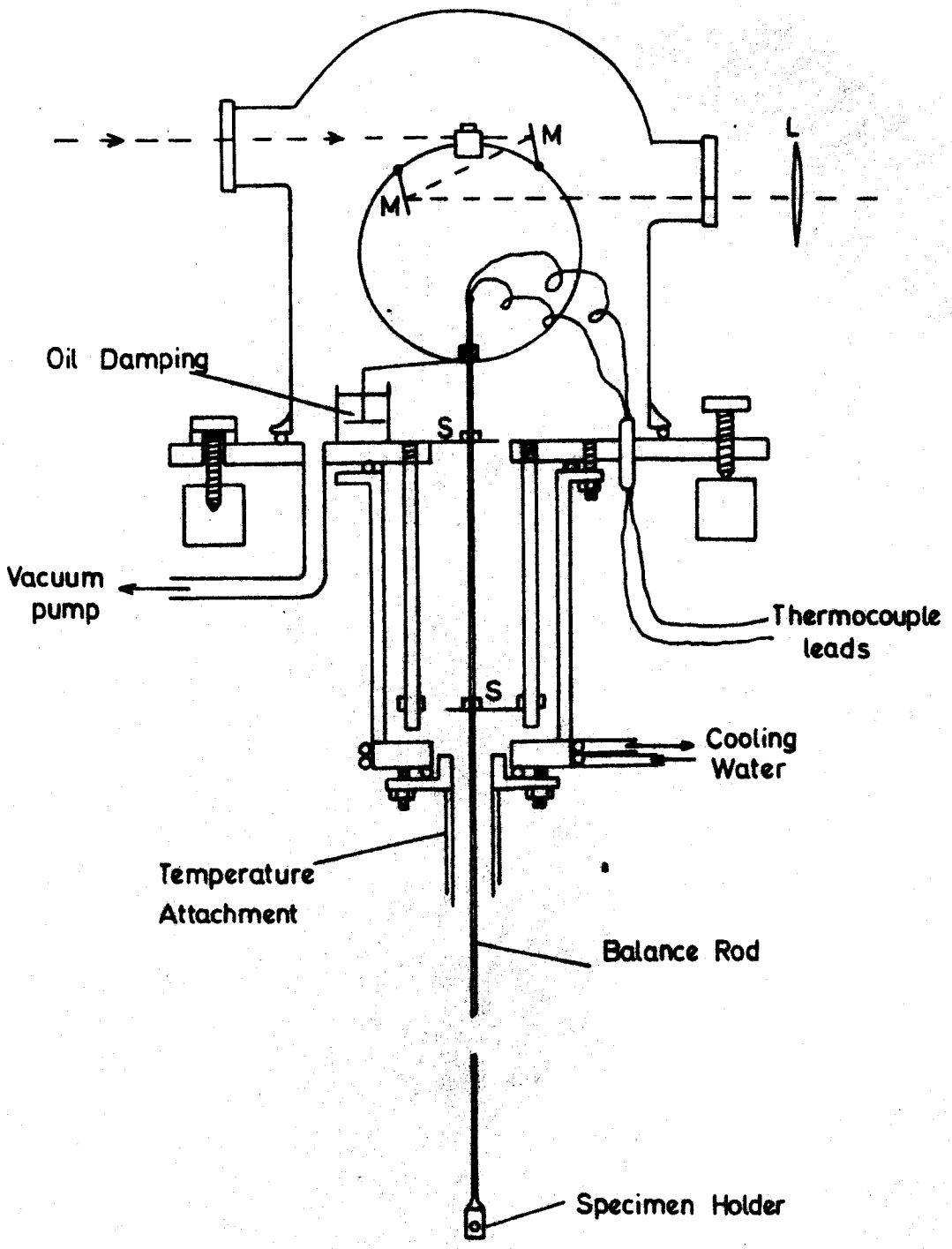

Fig. 4·3 Main Ring Balance Assembly

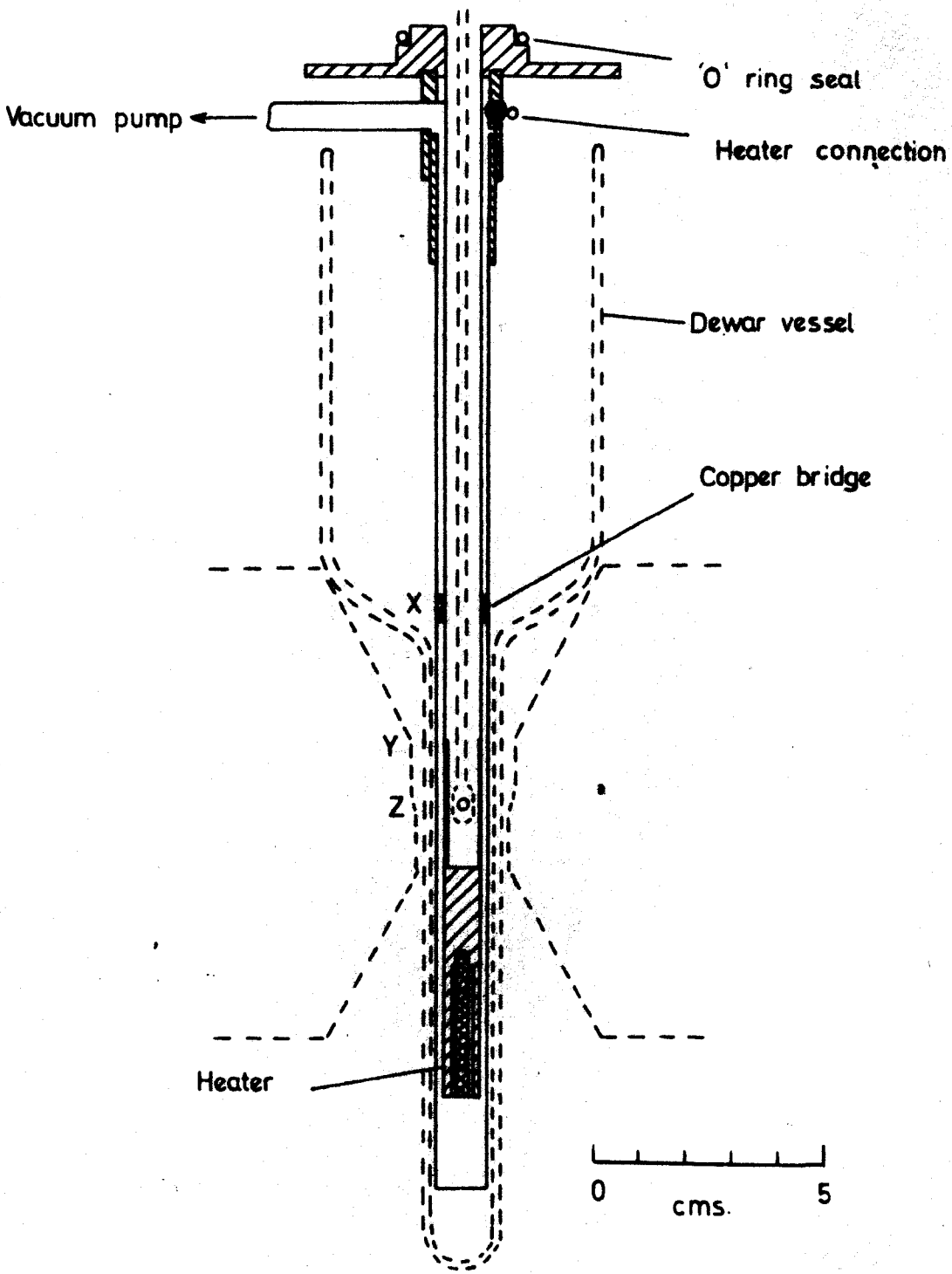

Fig 4.4 Low Temperature Attachment

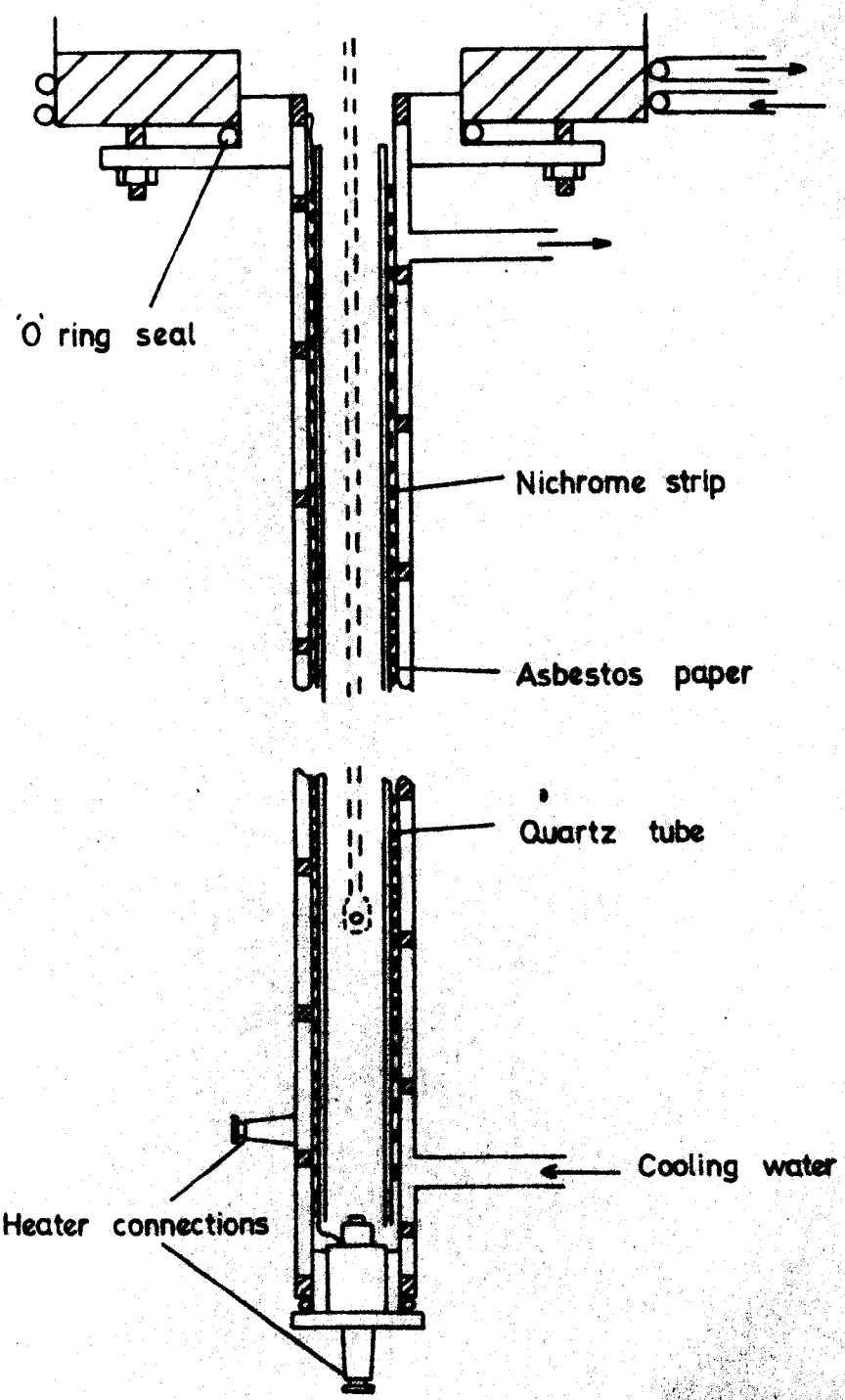

Fig. 4.5 Furnace Attachment

4.7 Alignment and operation of ring-balances

The specimen holder, containing a standard specimen, was centred visually in the pole-gap. A long focus microscope was then used to observe the movement of the specimen when the field was switched on and off. Horizontal adjustments were made until no sideways movement could be detected. The position of optimum field gradient for the ferromagnetic balance was obtained by adjusting the vertical height of the magnet until the position of maximum deflection was found. The horizontal adjustment was then rechecked. The optimum position of constant $H\partial H/\partial z$ for the paramagnetic balance, shown in figure (4.2b), was also obtained by a vertical traverse.

The magnetic fields at the specimen positions were measured for a series of values of energizing currents up to a maximum of 13 amps using a Pye Scalamp fluxmeter, and a search coil of 30 cm^2 turns.

Box corrections were obtained by measuring the deflection of the empty specimen holder in several applied fields. The linearity of the instruments was checked by comparing the deflections produced by different masses of standard specimens. When paramagnetic measurements were made, small weights were always added to the ring in order to ensure that the rest position did not change for specimens of different mass. Alignment checks were repeated periodically, and calibration runs were made before and after each complete experimental run.

4.8 Analysis of results

The ferromagnetic specimens were polished to an approximately ellipsoidal shape using fine emery paper. Demagnetizing corrections were estim-

ated for the appropriate axial ratios using the demagnetizing factors given by Stoner (1945). The effective field H is related to the applied field H_A by the relation

$$H = H_A - N\rho\sigma_{HT} \tag{4.6}$$

where N is the appropriate demagnetizing factor, ρ is the density, and σ_{HT} is the specific magnetization in a field H at temperature T.

Magnetic isothermals were plotted over a wide range of temperature, and values of the spontaneous magnetization, σ_{0T}, were obtained. At low temperatures σ_{0T} was obtained by linear extrapolation, but near the Curie temperature σ_{0T} was derived from σ^2 versus H/σ plots. (Kouvel 1957). At low temperatures, extrapolation to $0^\circ K$ was made using the relation

$$\sigma_{0T} = \sigma_{00}(1 - \alpha T^{3/2}) \tag{4.7}$$

The results were converted to Bohr magnetons per 'molecule', p, using the expression

$$p = M\sigma_{00}/N\beta \tag{4.8}$$

where M is the 'molecular weight', N is Avogadro's number, and β is the Bohr magneton.

Susceptibility, and reciprocal susceptibility versus temperature curves were plotted for paramagnetic and antiferromagnetic alloys. Néel temperatures were measured, and paramagnetic Curie temperatures were extrapolated. Bohr magneton numbers were obtained from the slope of the reciprocal susceptibility curve using equation (2.13).

CHAPTER 5

Experimental results - Cu_2MnX and CuMnX

5.1 Introduction

The Heusler alloys containing copper were the first to be investigated and have since been the subject of many investigations. The magnetic results of most observers agree to within 10%, but it is difficult to determine which are the most reliable because the magnetic properties depend critically upon the alloy structures, and quantitative measurements of the extents of order are not usually given. The best available data on the alloys is summarized below.

5.2 Cu_2MnAl

The most complete magnetization data on this alloy is given by Endo et al (1964), and Oxley (Thesis, 1964). The alloys were prepared by quenching from 800°C followed by an anneal between 100°C and 200°C for over 100 h. The results are summarized in table (5.1).

TABLE 5.1

a_0 (A)	σ_{00}(emu/g)	μ_{00} (μ_B)	θ_F (°K)
5.95	97 ± 4	3.7 ± 0.2	600 ± 10

Felcher et al (1963) investigated a specimen that had undergone a similar heat treatment using neutron diffraction techniques at room temperature. A magnetic field of 12000 Oe was used to separate the magnetic and nuclear scattering contributions. They were able to show

that the alloy was highly ordered with a long-range order parameter S = 0.98, and the magnetic moment, at least to within 0.1 μ_B, was attributed to the Mn atom.

Kimura et al (1962) have shown that at 750°C the alloy has the B2 (CsCl type) structure, and Ohoyama and Webster (To be published) have shown from resistivity measurements made during rapid cooling that the transition temperature for Mn - Al ordering is 650°C.

Sucksmith and Bates (1923) measured the gyromagnetic ratio, and Lande splitting factor g = 2, and hence concluded that the magnetic properties were due to the spin, and not the orbital motion of the electrons.

Potter (1929) showed from single crystal torque measurements that the easy direction of magnetization is [111] .

5.3 Cu_2MnIn

An alloy at about the composition Cu_2MnIn was investigated by Coles, Hume-Rothery, and Myers (1949). The alloy was ferromagnetic as cast, and its magnetic properties were insensitive to heat treatment. The alloy had the Heusler structure, but with a small amount of an additional phase.

The alloy was reinvestigated by Oxley (Thesis, 1964), and his results for a specimen quenched from 525°C are summarized in table (5.2).

TABLE 5.2

a_0 (A)	σ_{00}(emu/g)	μ_{00} (μ_B)	Θ_F (°K)
6.2	74 ± 2	4.0 ± 0.1	520 ± 5

5.4 Cu_2MnSn

Taglang and Fournier investigated the phase changes in the alloy Cu_2MnSn, and two successive transformations were observed. The Heusler structure is only stable above 650°C, but may be retained at room temperature by very rapid quenching.

Oxley (Thesis, 1964) reinvestigated the alloy and his results are shown below in table (5.3).

TABLE 5.3

a_0 (A)	σ_{00}(emu/g)	μ_{00} (μ_B)	θ_F (°K)
6.17	76 ± 2	4.1 ± 0.1	(530)

The measured Curie temperature is an estimated value because the Heusler structure is not stable at that temperature, and precipitation of a non-magnetic phase occurs.

5.5 Cu_2MnSb and CuMnSb

Heusler, Starck and Haupt (1903) reported that an alloy containing Cu, Mn, and Sb was ferromagnetic, but the ferromagnetism they detected was probably due to the presence of binary alloys of Mn and Sb.

Oxley et al (1962) reported that an alloy at the composition Cu_2MnSb had the Heusler structure but exhibited some antiferromagnetic characteristics. A maximum in the susceptibility was observed at 38°K, but Curie-Weiss behaviour was not observed above that temperature. However, Oxley (Thesis, 1964) later suggested that the alloy was probably a mixture of CuMnSb and Cu.

Nowotny and Glatzl (1952) showed from X-ray diffraction measurements

that CuMnSb was probably ordered in the Cl_b type structure with a lattice parameter 6.05 k.X., but they were unable to distinguish positively between the Cu and Mn sites.

20 g ingots were prepared for the present investigation at the compositions CuMnSb and Cu_2MnSb by arc melting with losses in melting of 1.9% and 1.0% respectively. The CuMnSb was annealed at 725°C, and the Cu_2MnSb at 600°C for 24 h before quenching. X-ray diffraction photographs of the two alloys appeared to be identical apart from a few extra lines on the Cu_2MnSb photograph. The additional lines were indexed as f.c.c. with a lattice parameter 3.68 A. The measured lattice parameters are compared with those calculated from density measurements im table (5.4).

TABLE 5.4

Alloy	Density (g/cm^3)	a_0 (A)	
		from Density	Measured
CuMnSb	6.8	6.2	6.097
Cu_2MnSb	7.1	5.7	6.097
Cu + CuMnSb	7.1	(3.61)	3.68
		6.2	6.097

Good agreement is shown for CuMnSb, and similar agreement is also observed for Cu_2MnSb if it is assumed to be a mixture of Cu and CuMnSb.

The proposed structures were confirmed by measuring the X-ray diffraction line intensities with a microdensitometer. The measured

and calculated intensities are compared in table (5.5).

TABLE 5.5

hkl	Debye-Scherrer line intensities Cu(Kα)			
	Calculated			Measured
	1. CuMn-Sb	2. CuMnSb-	3. Cu-MnSb	CuMnSb
111	39	31	70	37
200	32	40	0.1	32
220	100	100	100	(100)
311	19	15	33	19
222	9	11	0.1	8
400	16	16	16	14

hkl	Cu_2MnSb			Cu
	Calculated	Measured		Calculated
	$L2_1$	Main lines	Extra lines	f.c.c.
111	13	42	22	22
200	4	30	10	~10
220	100	(100)	5	6
311	7	~17	5	7
222	2	7	2	2
400	16	15	1	~1

It is seen that CuMnSb has the Cl_b type structure (1) as illustrated in table (3.3), although structure (2) cannot be entirely eliminated. It is clear that Cu_2MnSb does not have the Heusler structure, but consists of CuMnSb and Cu.

Some additional very faint lines were observed on both CuMnSb and Cu_2MnSb photographs. They could not be satisfactorily indexed, but their intensities were only about 1/2% of the intensities of the main lines.

The neutron diffraction patterns of the two alloys at 77°K are shown in figure (5.1). The 2 patterns are very similar except for the increased width and intensities at the (220) and (311) positions on the Cu_2MnSb pattern due to the superposition of the (111) and (200) lines respectively of copper. The calculated and measured intensities are compared in table (5.6).

TABLE 5.6

hkl	Nuclear intensities		
	Calculated	Measured	
	CuMnSb / Cu	CuMnSb	Cu_2MnSb
111	258	226	(226)
200	37.8	29	28
220/111	97.0/40.3	(97)	(97)/161
311/200	218 /23.0	161	(161)/116
222	17.3	15	11
400	25.1	26	27

CuMnSb has the Cl_b structure (1) with a small amount of random disorder, equivalent to α(Random) $\simeq$ 0.06, or S = 0.92. The calculated intensities are not shown for structure (2), because this structure may be definitely eliminated as the calculated intensities are very much

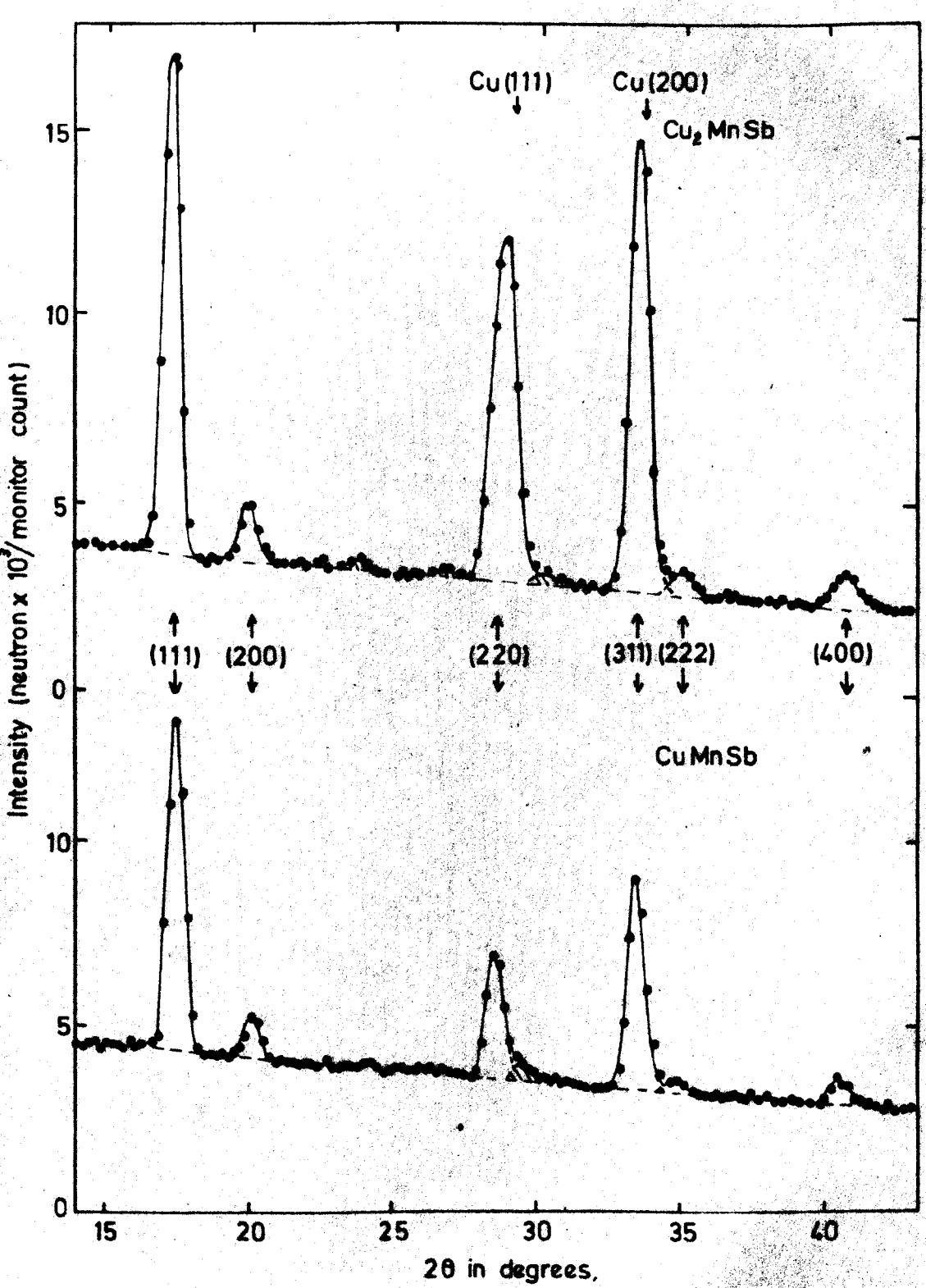

Fig. 5·1 Neutron diffraction patterns of Cu MnSb and Cu_2MnSb at 77°K

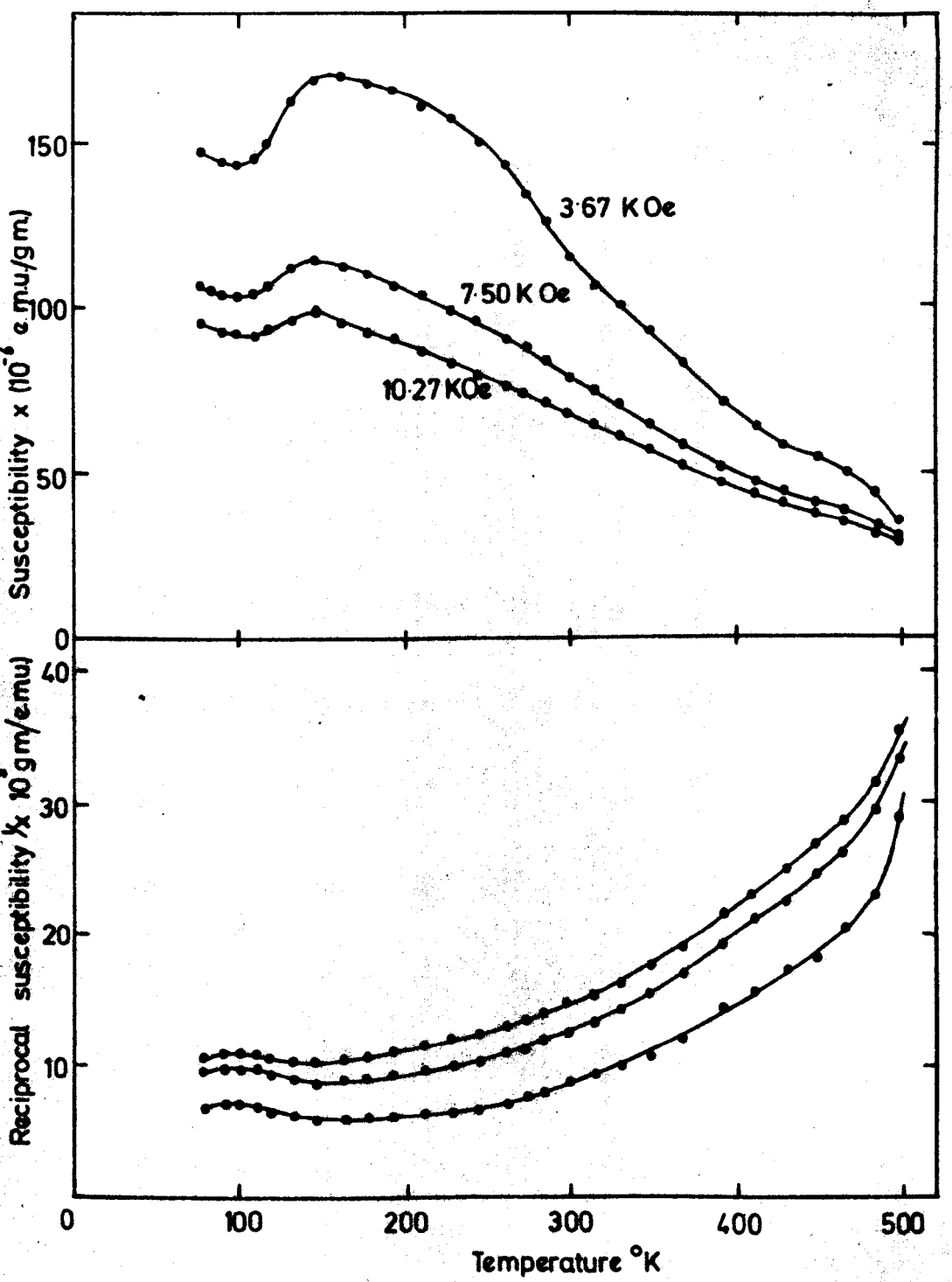

Fig. 5·2 Susceptibility and reciprocal susceptibility versus temperature for the alloy CuMnSb

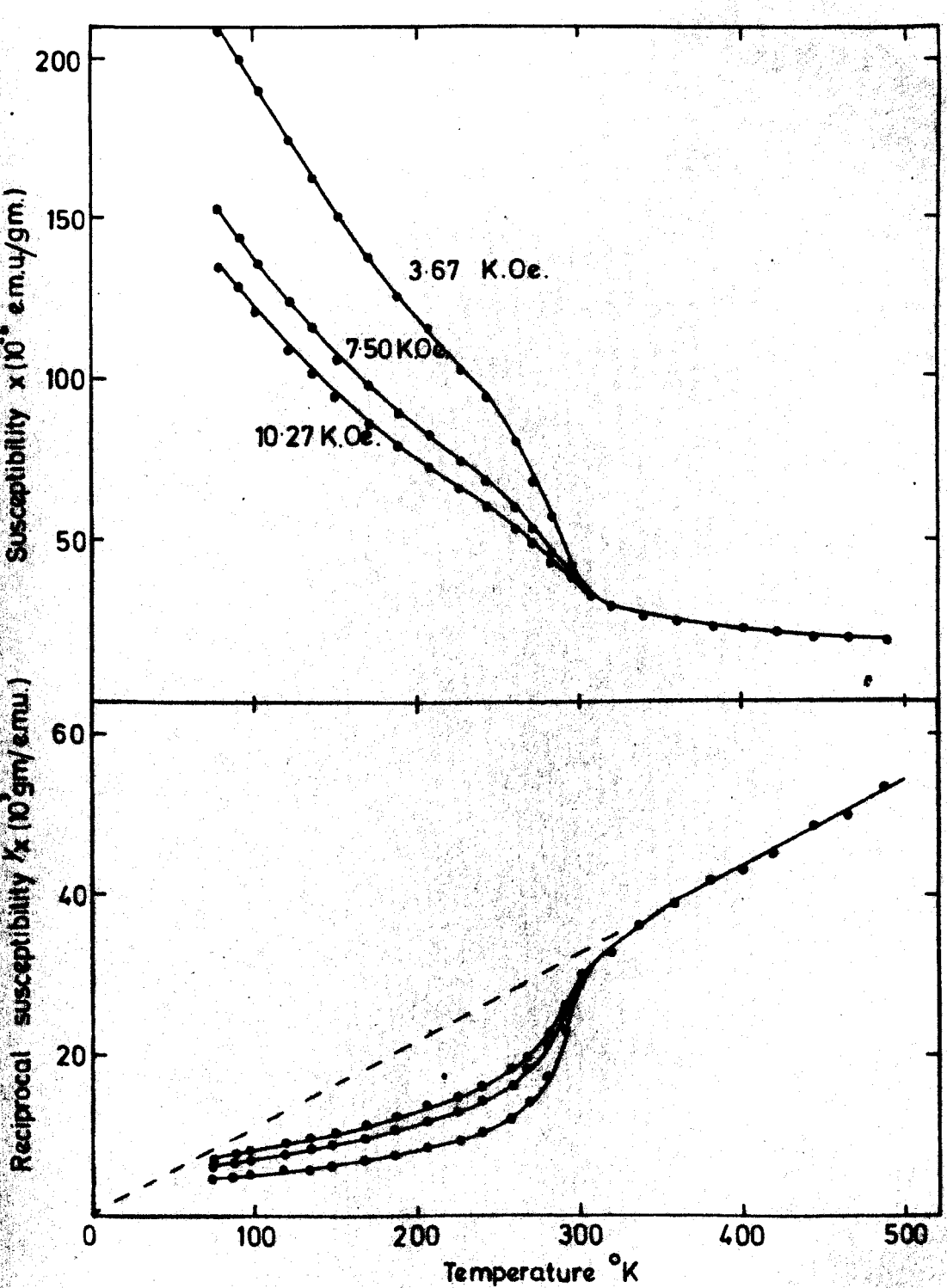

Fig. 5·3 Susceptibility, and reciprocal susceptibility versus temperature for the alloy Cu_2MnSb

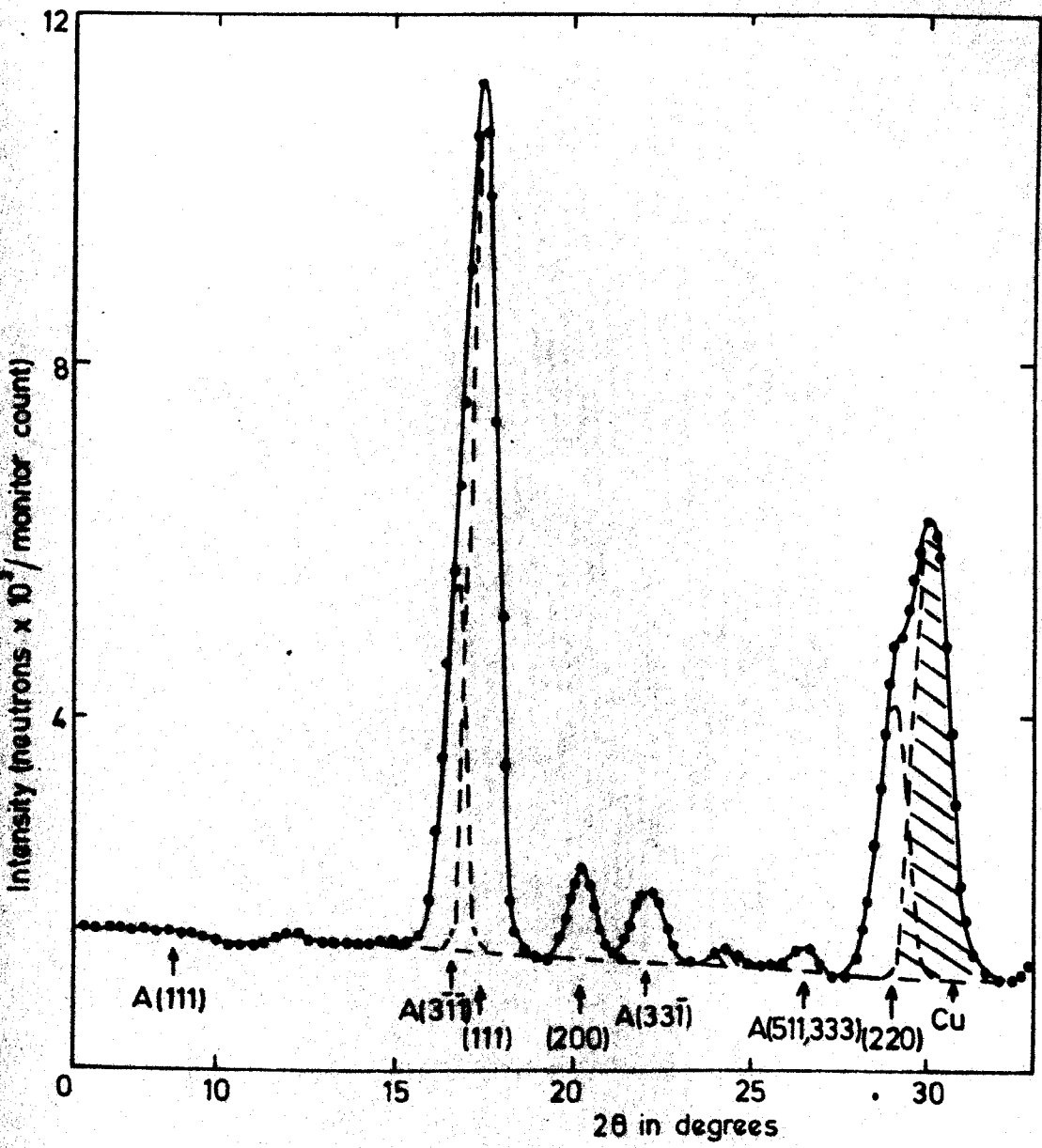

Fig. 5·4 Neutron diffraction pattern of CuMnSb at 4·2°K

different. It is also confirmed that Cu_2MnSb consists of CuMnSb + Cu, but the Cu lines are about 4 times as intense as expected. This can only be due to contamination from the copper supporting rod. Both alloys also show very weak additional peaks that could not be readily indexed.

The susceptibility and reciprocal susceptibility versus temperature curves for the two alloys are shown in figures (5.2) and (5.3). Both alloys show a field dependency over much of the measured range that is characteristic of a small amount of ferromagnetic impurity.

At temperatures above 350°K Cu_2MnSb follows a Curie-Weiss law, but at lower temperatures the effects of a small amount of ferromagnetic impurity are noticed. An estimate of the ferromagnetic contribution was obtained by subtracting the susceptibility predicted from Curie-Weiss behaviour from the measured susceptibilities. The impurity has a Curie temperature of 310 ± 10°K, and a spontaneous magnetization σ_{00} = 0.38 emu/g Cu_2MnSb. But, below 150°K the measured susceptibility is less than that expected for a mixture of a paramagnetic and a ferromagnetic, which is understandable if the CuMnSb exhibits some antiferromagnetism below approximately 150°K.

The CuMnSb differs from the Cu_2MnSb, in that the ferromagnetic impurity has a Curie temperature approximately 510°K, and the antiferromagnetic characteristics are more pronounced. A maximum in susceptibility occurs at 150 ± 10°K, but there is also a minimum at 100°K.

The neutron diffraction patterns at 77°K show no antiferromagnetic peaks, but the diffraction pattern of CuMnSb at 4.2°K shown in

(5.4) does. Antiferromagnetic peaks are observed at the $(3\bar{1}\bar{1})$, $(33\bar{1})$, (511) positions for a magnetic unit cell with twice the dimensions of the chemical unit cell. The (111) reflection expected at the angle $2\theta = 8.84^{\circ}$ is absent, indicating that $q^2(111) = 0$. Since the magnetic unit cell is twice the size of the chemical unit cell, then assuming the magnetic moments are confined to the Mn atoms, adjacent Mn atoms along the cube axes are oppositely aligned. Also, since $q^2(111) = 0$, the magnetic symmetry must be rhombohedral with the magnetic moments aligned parallel and antiparallel to the unique [111] axis, as in FeO (Shull et al, 1951). The calculated and measured magnetic intensities are compared in table (5.7).

TABLE 5.7

hkl $a = 2a_0$	q^2	Magnetic intensities	
		Calculated $\mu = 4.2\ \mu_B$	Measured
111	0	0	0
$3\bar{1}\bar{1}$	32/33	118	117
$33\bar{1}$	32/57	30	29
511,333	32/81, 0	8	9

The agreement between the measured and calculated intensities is excellent, indicating that the postulated structure is correct, and the magnetic moment of $4.2 \pm 0.2\ \mu_B$ at $4.2^{\circ}K$ is confined to the Mn atoms. Unfortunately, no neutron diffraction measurements were made on Cu_2MnSb at $4.2^{\circ}K$, and so no direct magnetic structure comparisons can be made. However, the other results indicate that the two alloys are essentially

similar. The differences in the susceptibility curves are probably due to the slightly different ferromagnetic impurities resulting from the different compositions and heat treatments.

CHAPTER 6

Experimental results - Ni_2MnX and NiMnX

6.1 Ni_2MnAl

Raynor (1944) discovered a ternary phase in the Ni-Mn-Al system at the composition $Ni_4Mn_{11}Al_{60}$ together with an additional metastable phase of undetermined composition. Robinson (1952, 1954) showed that the alloys had an orthorhombic unit cell.

Tsuboya and Sugihara (1961) discovered a ferromagnetic $\mathcal{H}$ phase in the composition range 25-50 at.% Mn, 10-30 at.% Ni, and 40-52 at.% Al, with a B2 structure. The other phases existing at compositions adjoining the $\mathcal{H}$ phase did not exhibit ferromagnetism.

A 20 g ingot was made at the composition Ni_2MnAl with a loss in weight on melting of 1.6%. Samples were annealed at 800°C for 24 h, after which one was quenched, and the other was slow-cooled over 36 h. X-ray photographs taken of the two samples were identical. The measured and calculated results are compared in table (6.1).

TABLE 6.1

Density g/cm^3	a_0 from density	a_0 Measured	$F^2(\theta = 0)$ Calculated (111)	(200)	(220)	Structure
			144	324	8836	$L2_1$
6.7	5.8 A	5.821 A	234	144	8836	$F\bar{4}3m$
			0	324	8836	B2

The lattice parameters are in excellent agreement. The even superlattice lines were of the expected intensity for a Heusler alloy at this composition, but the odd superlattice lines were not visible. Ni_2MnAl has thus either the $L2_1$ structure with a large amount of Mn-Al disorder, or the B2 structure which is equivalent to complete Mn-Al disorder. Several weak lines, indexed as b.c.c. with a_0 = 3.21 A, were also observed.

The reciprocal susceptibility versus temperature curves for the quenched and slow-cooled alloys are shown in figure (6.1). The two alloys behaved a little differently. Above 300°K, both alloys are paramagnetic, but the slow-cooled alloy has the greater susceptibility. Below 300°K the deviation from Curie-Weiss behaviour indicates some form of antiferromagnetic alignment, but the field dependency is complex. In the quenched alloy, the susceptibility increases with field below 300°K. The susceptibility of the slow-cooled alloy increases with field up to 215°K, but decreases with field in the region 215 to 300°K. A possible explanation of the latter may be the presence of minute amounts of ferromagnetic phase formed during slow-cooling. The additional phase could be due to very small regions of Mn-Al order which, like Ni_2MnGa and Ni_2MnIn, might be ferromagnetic, or it could be due to a sub-microscopic precipitate.

Neutron diffraction measurements were made on the quenched alloy at 77°K and 293°K. The diffraction patterns are shown in figure (6.2). The measured intensities were corrected for the effects of temperature using a mean atomic weight of 50, and a Debye temperature 378°K. The

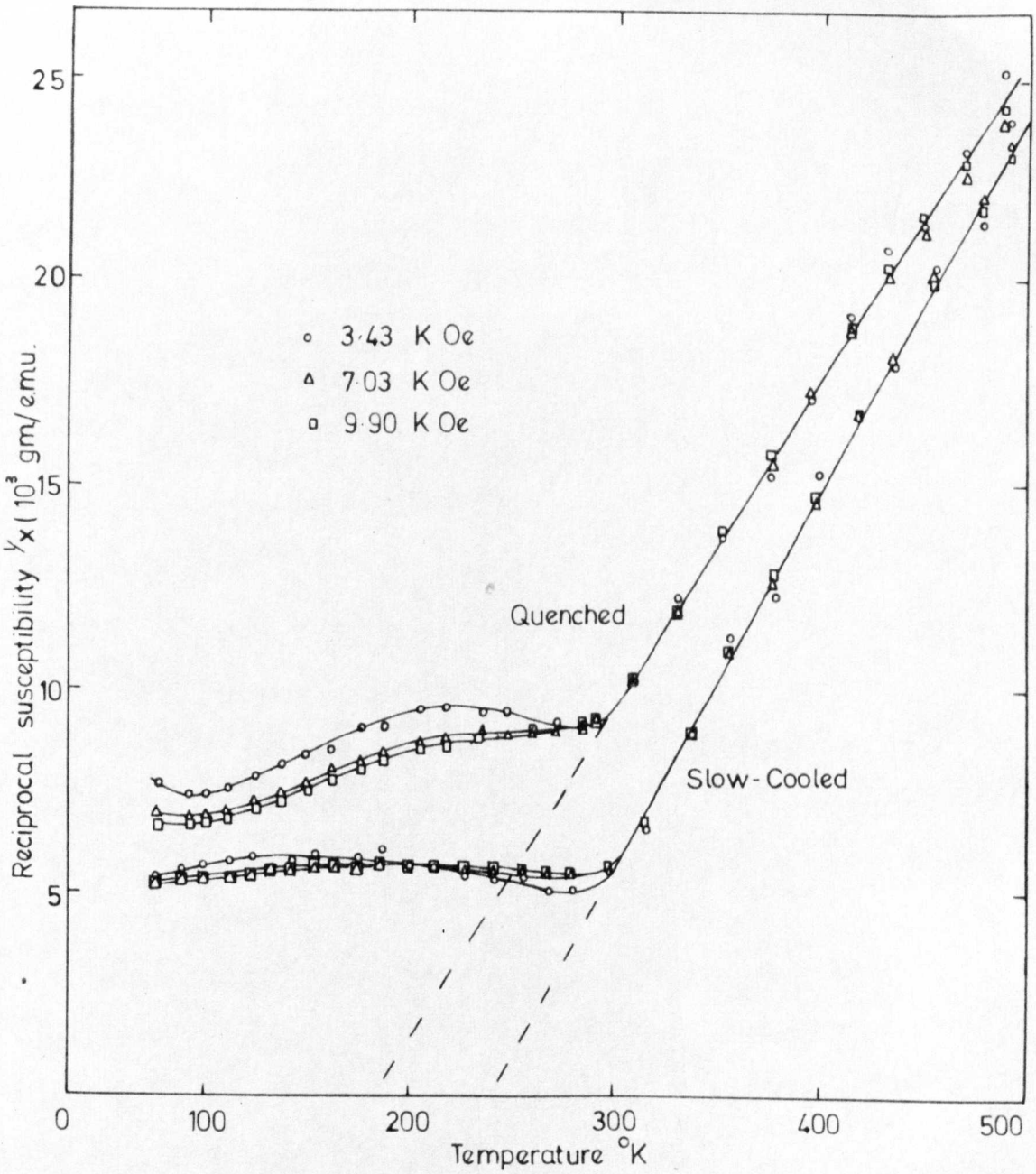

Fig. 6·1 Reciprocal susceptibility versus Temperature for the alloy Ni_2MnAl when Slow Cooled and Quenched, for three applied fields.

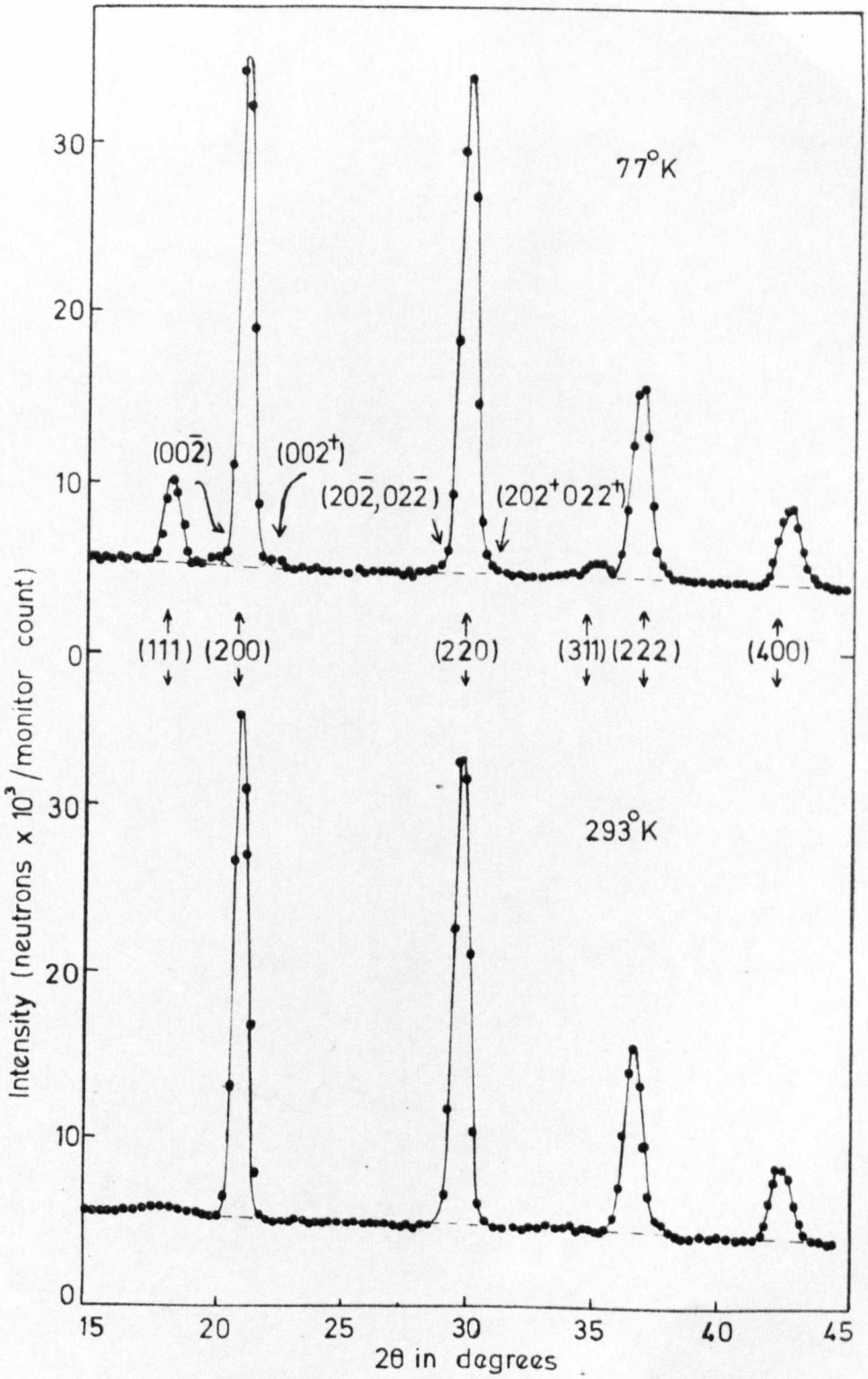

Fig. 6·2 Neutron diffraction patterns of Ni_2MnAl at 293°K and 77°K

intensities of the measured nuclear lines are compared with the calculated intensities in table (6.2).

TABLE 6.2

hkl	Nuclear intensities		
	Calculated		Measured
	$L2_1$	B2	(Mean)
111	82.3	0	0
200	397	397	356
220	396.6	396.6	(396.6)
311	70.1	0	0
222	183	183	184
400	103	103	90

It is seen that the alloy is highly ordered in the B2 structure. The 2 small peaks observed at the (111) and (311) positions at 293°K are magnetic rather than nuclear in origin. This may be shown from the ratio of their intensities, and in addition, the susceptibility results indicate the onset of antiferromagnetism at 300°K.

The diffraction pattern at 77°K shows antiferromagnetic peaks at the (111) and (311) positions, but in addition there are satellites to the (200) line, and a broadening at the base of the (220) line. The presence of both antiferromagnetic and satellite lines indicates that the magnetic moment configuration has antiferromagnetic and spiral components, such as is exhibited by the antiferromagnetic cone spiral shown in figure (3.2c). The measured magnetic intensities are compared

in table (6.3) with intensities calculated on the assumption that the magnetic moments are confined to the Mn atoms, and the structure is as in figure (3.2c), with the spiral axis [111] .

TABLE 6.3

	2θ		Magnetic intensities	
hkl	Measured	Calculated $\Delta = 1/9$	Measured	Calculated $\mu_{77} = 4.3$ $\beta = 30^{\circ}$
111	18.13	18.15	62	61.8
311	35.16	35.15	15	14.6
200^{-}	19.80	19.86	4.5	5.4
200^{+}	22.20	22.20	5.5	4.7
220^{-}	~28.5	28.2	~ 2	2.0
$2\bar{2}0^{\pm}$	-	30.1	-	2.0
220^{+}	~31.0	31.5	~2	1.4

The intensities of the antiferromagnetic lines (111) and (311) are in excellent agreement with the calculated results assuming a fundamental component $\mu \cos \beta = 3.73\ \mu_B$, where β is the cone 1/2 angle. Satisfactory agreement is obtained for the (200) satellite lines if it is assumed that the spiral component $\mu \sin \beta = 2.16\ \mu_B$, and hence $\beta = 30^{\circ}$. The unresolved (220) satellite lines are also of the right order of magnitude.

The positions of the satellite lines are in reasonable agreement with the calculated angles assuming $\Delta = 1/9$, and a spiral axis [111] . However, only slight changes in position and intensity would be expected for other spiral axes, (e.g. [100]) and consequently the spiral axis

cannot be defined unambiguously from this data. But, providing the spiral axis is [100], [110], or [111], then $\Delta = 1/9$, which corresponds to a rotation $\phi = 20^{\circ}$ between adjacent antiparallel spins along the spiral axis.

The magnetic properties of Ni_2MnAl are summarized in table (6.4).

TABLE 6.4

θ_N	$\mu_{0,77}$	μ_{00}	Spin angle	Cone 1/2 angle
^{o}K	μ_B	Extrapolated	ϕ	β
300 ± 10	4.3 ± 0.2	4.4 ± 0.3	20 ± 1.5°	30 ± 3°

6.2 Ni_2MnGa

Hames (1960) reported that an alloy at the composition Ni_2MnGa was ferromagnetic and probably had the $L2_1$ structure with a lattice parameter 5.85 A.

A 20 g ingot was made at the composition Ni_2MnGa with a loss in weight on melting of 0.5%. The alloy was annealed at 800°C for 24 h, and then quenched. The calculated and measured X-ray results are shown in table (6.5).

TABLE 6.5

Density	a_0 from	a_0	$F^2(\theta = 0)$ Calculated			Structure
g/cm^3	density	Measured	(111)	(200)	(220)	
			36	0	12544	$L2_1$
8.2	5.82 A	5.825 A	18	36	12544	$F\bar{4}3m$
			16	16	12544	DO_3

The lattice parameters are in excellent agreement. The odd superlattice lines were very weak, but the even lines were absent, in agreement with Hames' suggestion that the alloy has the Heusler structure.

The magnetic isothermals are shown in figure (6.3), and the magnetization curves in figure (6.4). The principal magnetic features are summarized in table (6.6).

TABLE 6.6

θ_F ^oK	Transition Temperature ^oK	σ_{00} (emu/g) (Extrapolated)	μ_{00} μ_B
379 ± 3	227 ± 2	96 ± 3	4.17 ± 0.2

Typical ferromagnetic behaviour is observed down to 227°K, but at that temperature the alloy becomes more difficult to saturate. The change occurs over a very small temperature interval, and is reversible.

An X-ray photograph taken with a modified powder camera at 190°K showed a tetragonal structure, a = 5.920 A, c = 5.591 A, and c/a = 0.944. It is to be expected that the magnetic and crystallographic changes are related, and occur together at 227°K.

Neutron diffraction patterns recorded at 293 and 77°K are shown in figure (6.5). The measured intensities were corrected for the effects of temperature using a mean atomic weight of 61, and a Debye temperature 310°K. The measured and calculated intensities at 293°K are compared in table (6.7).

Excellent agreement exists between the measured and calculated intensities if it is assumed that there is a small amount of random

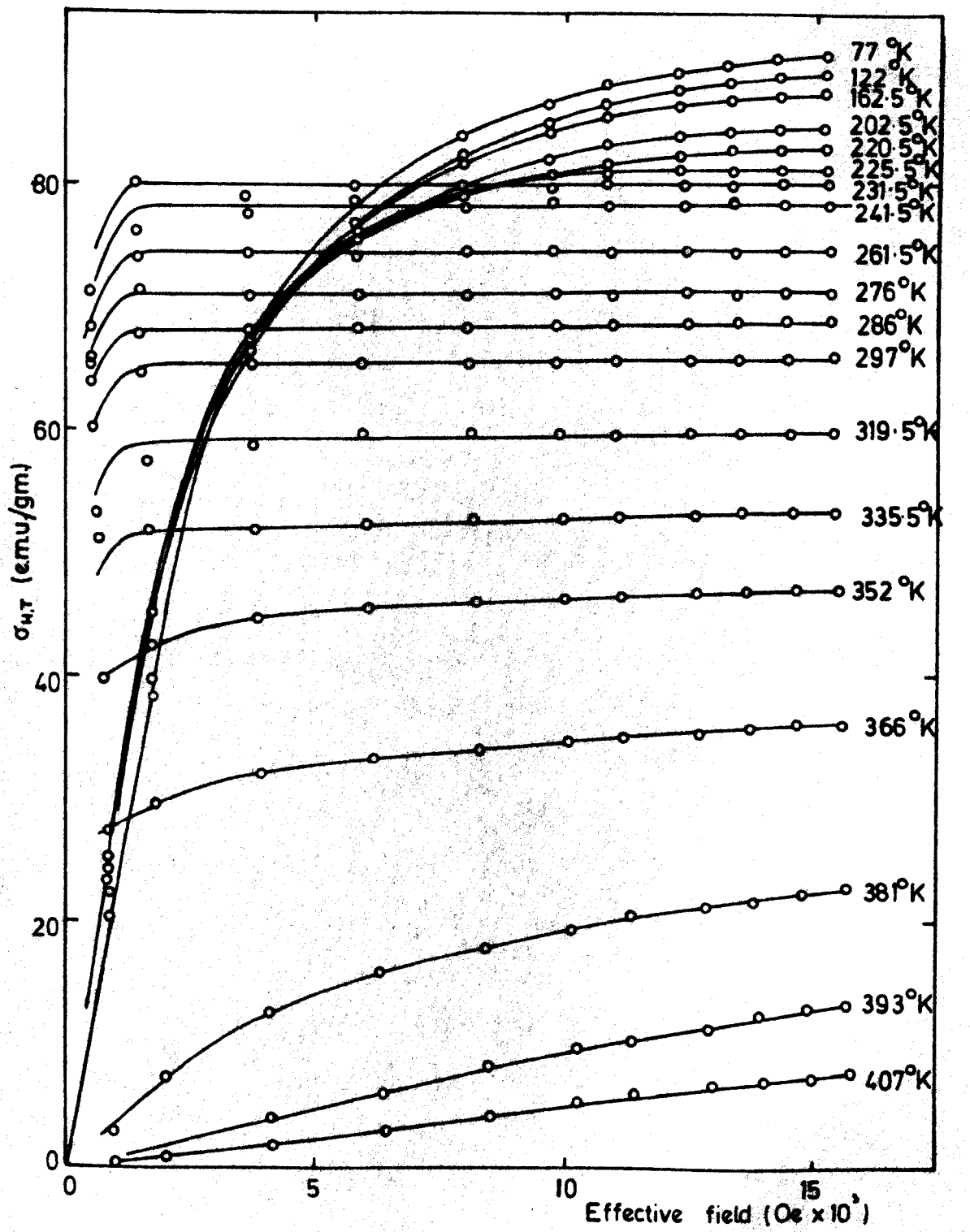

Fig. 6.3 Magnetic isotherms of Ni_2MnGa

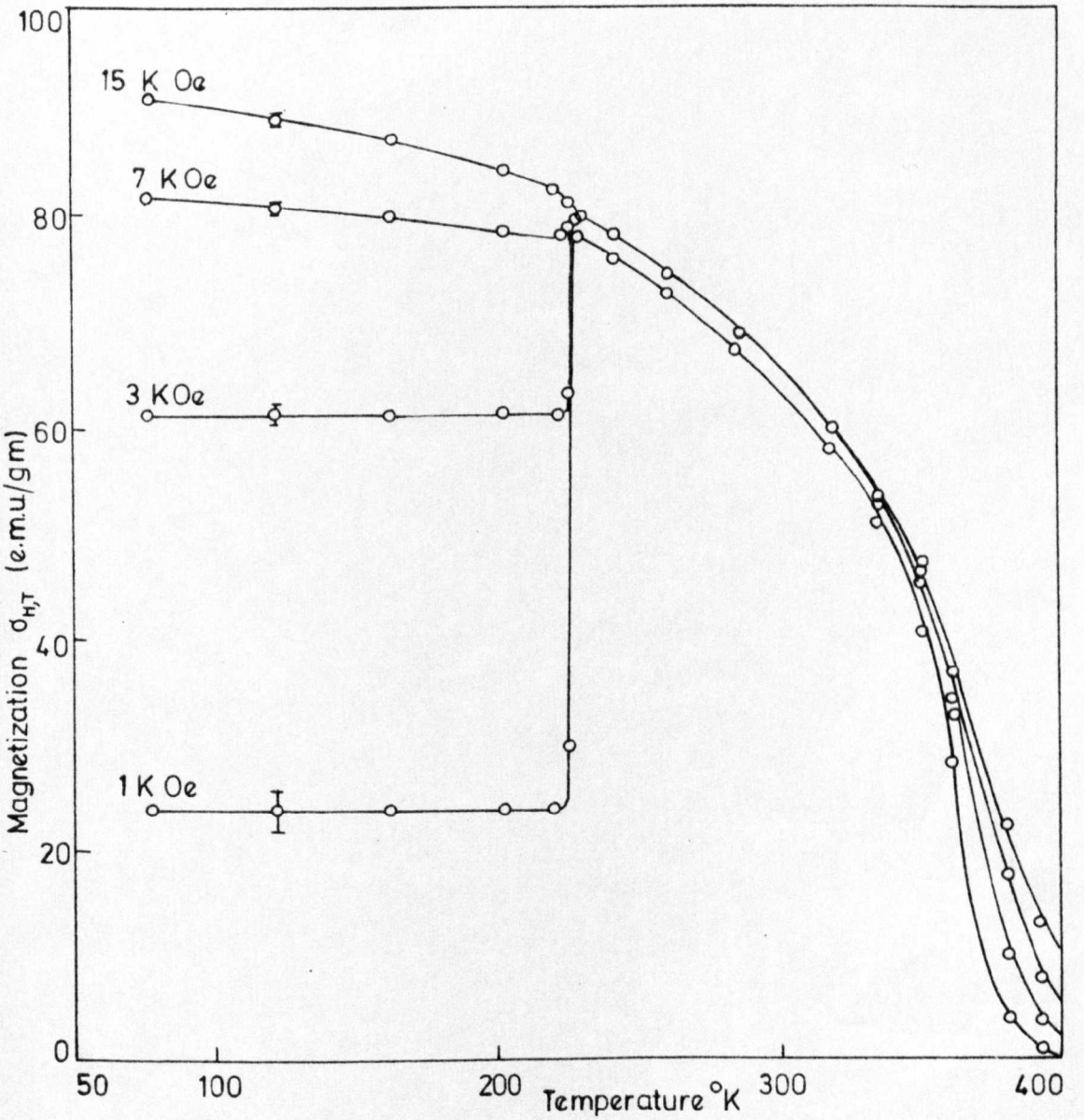

Fig. 6·4 Magnetization $\sigma_{H,T}$ versus temperature for several fields for the alloy Ni_2MnGa

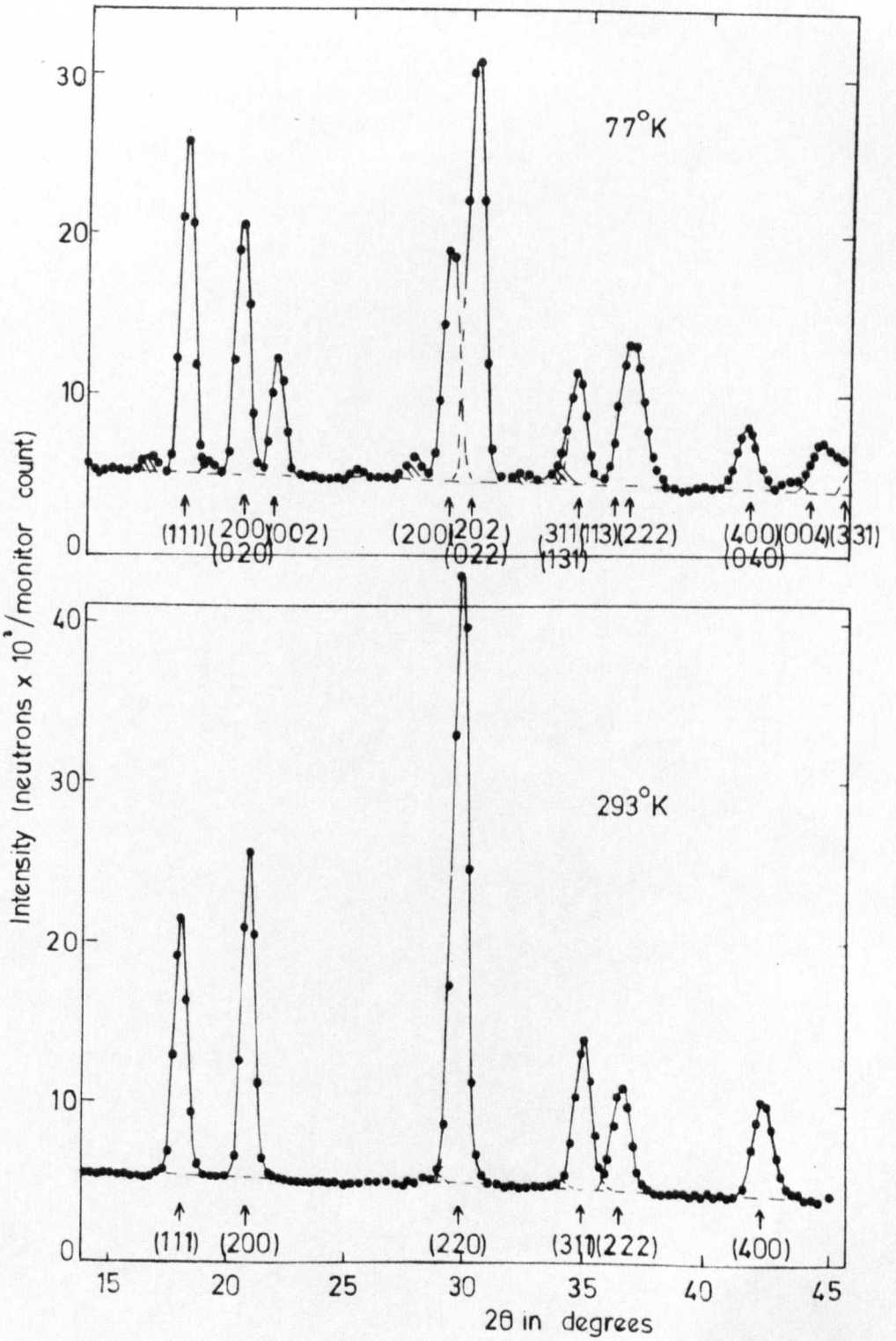

Fig. 6·5 Neutron diffraction patterns of Ni_2MnGa at 293°K and 77°K

disorder equivalent to S = 0.97, and the entire magnetic moment is confined to the Mn atoms.

TABLE 6.7

hkl	Calculated intensities $\mu_{0,293} = 2.90$		Measured
	$L2_1$	S = 0.97	intensities
111	228	203	200
200	287	255	254
220	563	563	(563)
311	171	152	154
222	126	112	117
400	144	144	127

The low temperature diffraction pattern shows clearly the change to a tetragonal structure, but it is noticed that in addition there are several extra weak lines. In view of the behaviour of Ni_2MnAl it might be expected that these lines are magnetic in origin, but this is most unlikely since they do not occur in satellite pairs, and there is no apparent form factor fall off with angle. The low temperature X-ray photograph was inspected again very carefully and some additional very faint lines were seen, but there was no exact correlation with the extra neutron lines.

The low temperature neutron diffraction intensities are compared in table (6.8). It is seen that the 3 sets of calculated intensities, corresponding to 3 different moment orientations, do not differ very much, but the best agreement is obtained if it is assumed that the

moments are aligned along arbitrary [111] axes.

TABLE 6.8

hkl	Calculated intensities (S = 0.97) $\mu_{0,77} = 4.1$			Measured intensities
	[001]	[010/100]	[111]	
111	237	235	236	242
200/020	198	181	187	187
002	73	87	83	83
220	201	196	197	(199)
202/022	369	369	371	(368)

It is difficult to explain the presence of the weak additional lines on the low temperature diffraction pattern, particularly as the quantitative agreement of the main lines is so good. Further X-ray and neutron diffraction measurements over a wider temperature range would be of value in determining their origin.

6.3 $\underline{Ni_2MnIn}$

Hames (1960) reported that Ni_2MnIn was ferromagnetic at room temperature and probably had the $L2_1$ structure with lattice parameter $a_0 = 6.07$ A.

A 20 g ingot was made at the composition Ni_2MnIn with a loss in weight on melting of 1.2%. After being annealed for 24 h, part of the sample was quenched, and the remainder was slow-cooled over 36 h. X-ray photographs taken of the 2 samples were identical. The measured and calculated results are compared in table (6.9).

The lattice parameters are in good agreement. Both sets of superlattice lines were clearly visible, with the odd superlattice lines in

general a little stronger than the adjacent even superlattice lines, as expected for the $L2_1$ structure.

TABLE 6.9

Density g/cm^3	a_0 from density	a_0 Measured	$F^2(\theta = 0)$ Calculated (111)	(200)	(220)	Structure
			576	324	16900	$L2_1$
8.4	6.1 A	6.068 A	450	576	16900	$F\bar{4}3m$
			484	484	16900	DO_3

The magnetic isothermals are shown in figure (6.6), and the corresponding magnetization curve in figure (6.15). The principal magnetic features are summarized in table (6.10).

TABLE 6.10

θ_F (°K)	σ_{00} (emu/g)	μ_{00} (μ_B)
323 ± 4	85.5 ± 1	4.40 ± 0.05

Neutron diffraction patterns recorded at 293 and 77°K are shown in figure (6.7). The measured intensities, corrected for the effects of temperature using a mean atomic weight 72 and a Debye temperature 306°K, are compared with the calculated intensities in table (6.11). The calculated intensities for the $F\bar{4}3m$ and DO_3 structures are not shown, but are very different from the measured values. The calculated intensities are calculated on the assumptions that there is a small amount of random disorder, corresponding to S = 0.95, and the magnetic moments are confined to the Mn atoms. The agreement between the measured

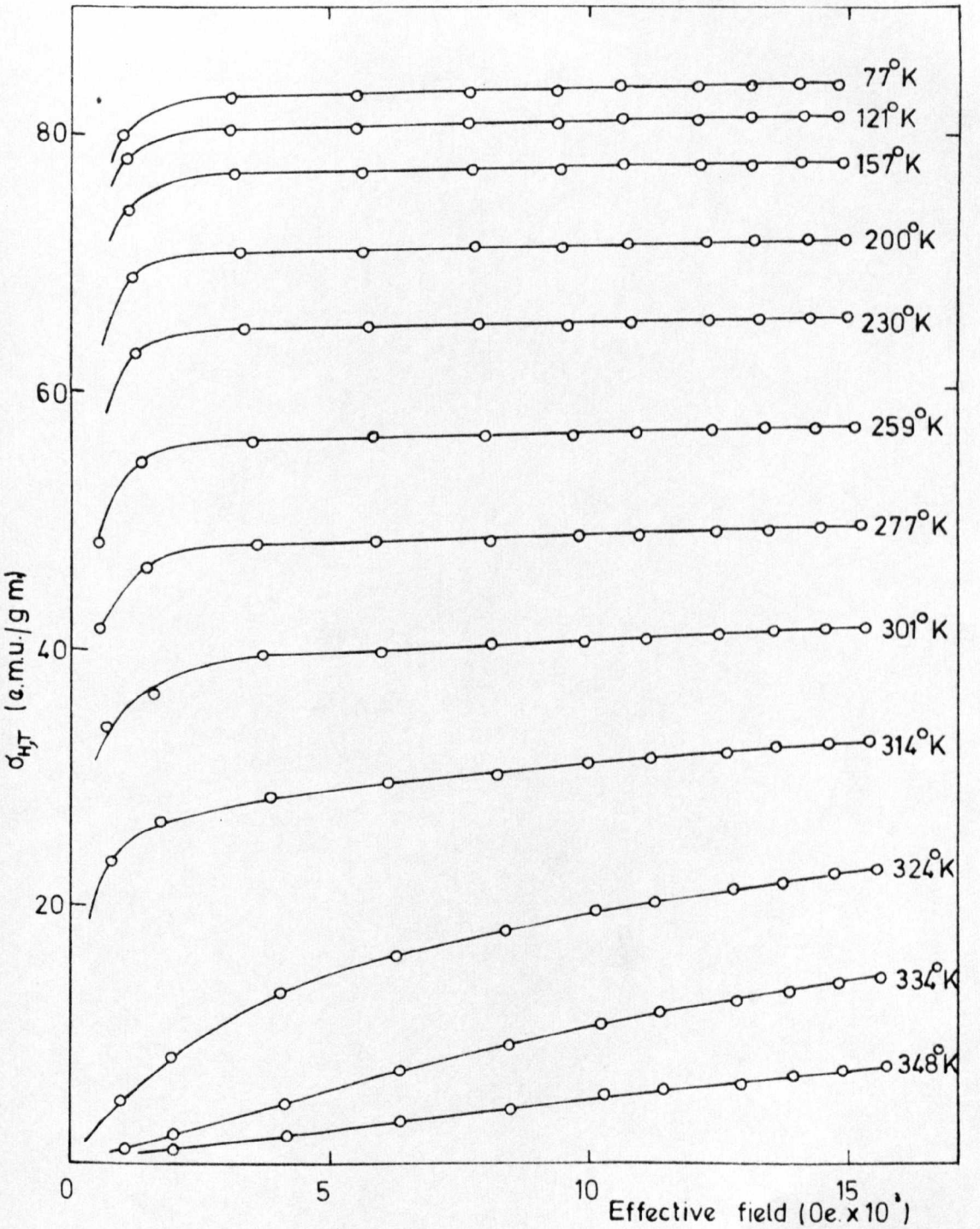

Fig. 6.6 Magnetic isotherms of Ni_2MnIn

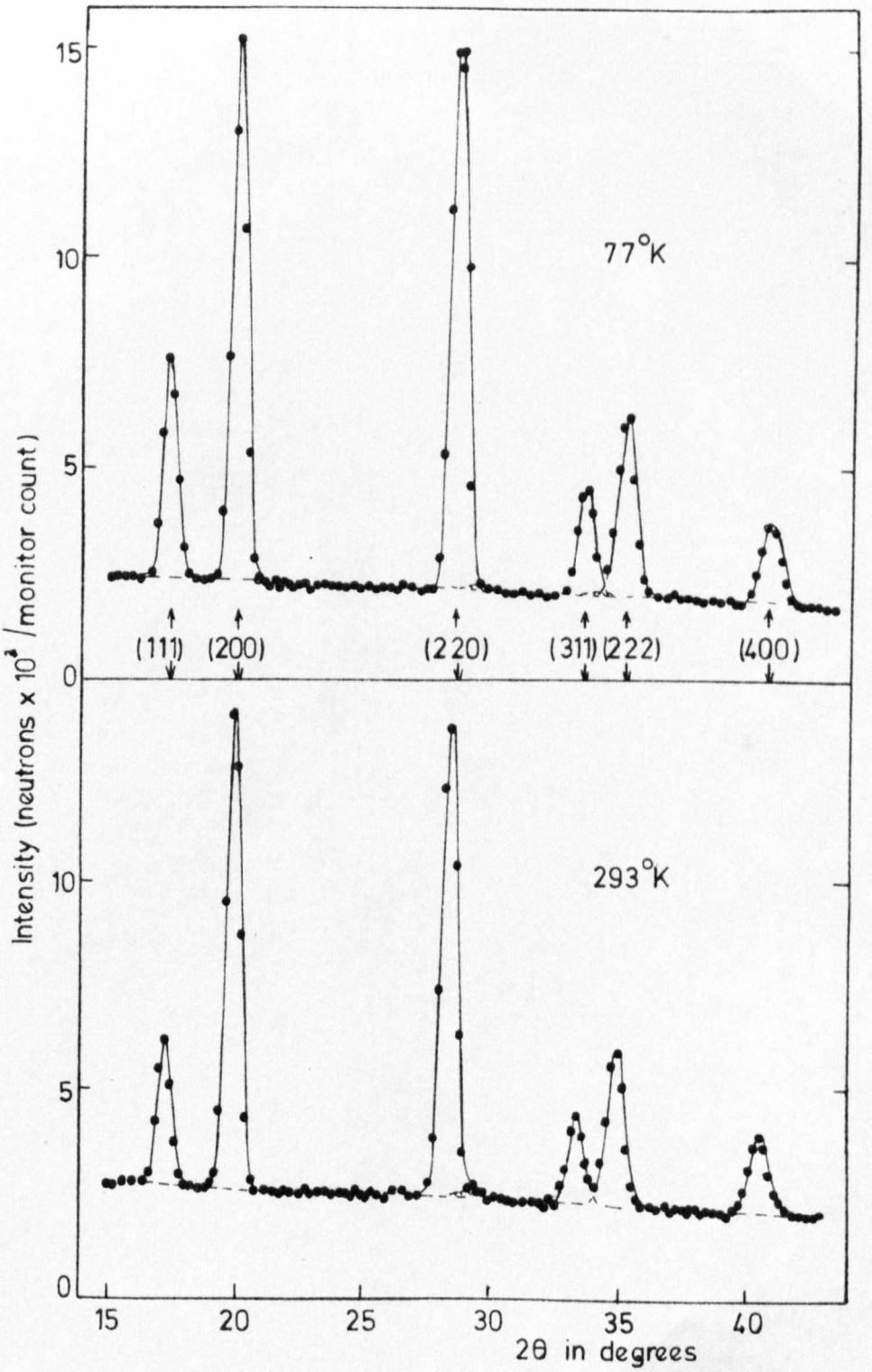

Fig 6·7 Neutron diffraction patterns of Ni_2MnIn at 293°K and 77°K

and calculated intensities, particularly at 77°K supports these assumptions.

TABLE 6.11

hkl	Calculated intensities S = 0.95		Measured intensities	
	$\mu_{0,77} = 4.27$	$\mu_{0,293} = 2.16$	77°K	293°K
111	160	101	162	125
200	411	383	407	408
220	460	441	(460)	(441)
311	89	73	94	87
222	176	172	172	169
400	114	113	89	99

6.4 Ni_2MnSn

Castelliz (1953) reported that Ni_2MnSn had the $L2_1$ structure, homogeneous along a narrow section $Ni_2Mn_xSn_{2-x}$, with $1 \leqslant x \leqslant 1.6$ and lattice parameter 5.986 kX at $x = 1$. But, due to the small difference between the atomic scattering factors of Ni and Mn, the Ni and Mn sites could not be determined with any certainty, and Kripyakevich et al (1954) reported that Ni_2MnSn had the DO_3 type structure.

Oxley (1964) reported that the alloy was ferromagnetic with a saturation moment $\mu_{0,0} = 3.98\ \mu_B$.

A 20 g ingot was made at the composition Ni_2MnSn with a loss in weight on melting of 0.9%. After annealing at 800°C for 24 h samples were quenched and slow-cooled respectively. X-ray photographs taken of the two samples were identical. The measured and calculated results

are compared in table (6.12).

TABLE 6.12

Density g/cm^3	a_0 from density	a_0 Measured	$F^2(\theta = 0)$ Calculated (111)	(200)	(220)	Structure
			625	361	17161	$L2_1$
8.9	6.0 A	6.052 A	493	625	17161	$F\bar{4}3m$
			529	529	17161	DO_3

The lattice parameters are in good agreement. Both sets of superlattice lines were clearly visible and of the expected intensity, with the odd superlattice lines in general slightly stronger than adjacent even superlattice lines.

The magnetic isothermals are shown in figure (6.8), and the corresponding magnetization curve in figure (6.15). The principal magnetic features are summarized in table (6.13).

TABLE 6.13

θ_F (^oK)	σ_{00} (emu/g)	μ_{00} (μ_B)
344 ± 3	77.7 ± 1	4.05 ± 0.05

The neutron diffraction pattern recorded at 293^{o}K is shown in figure (6.9). Debye temperature corrections were made using a mean atomic weight of 72, and an estimated Debye temperature 306^{o}K. The measured and calculated values are compared in table (6.14).

The DO_3 structure is clearly inappropriate, but reasonable agreement is achieved with the calculated intensities for the $L2_1$ structure

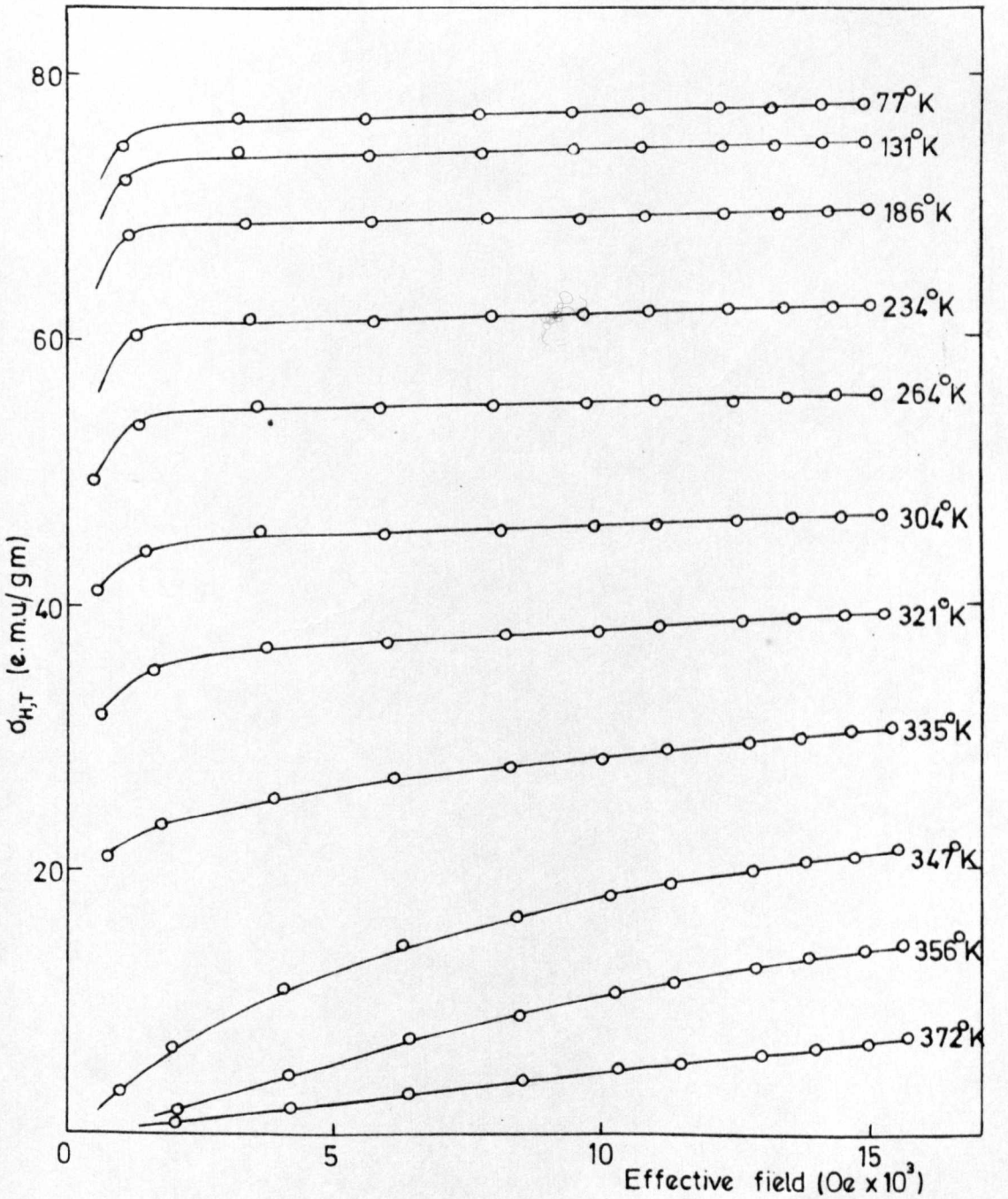

Fig. 6·8 Magnetic isotherms of Ni_2MnSn

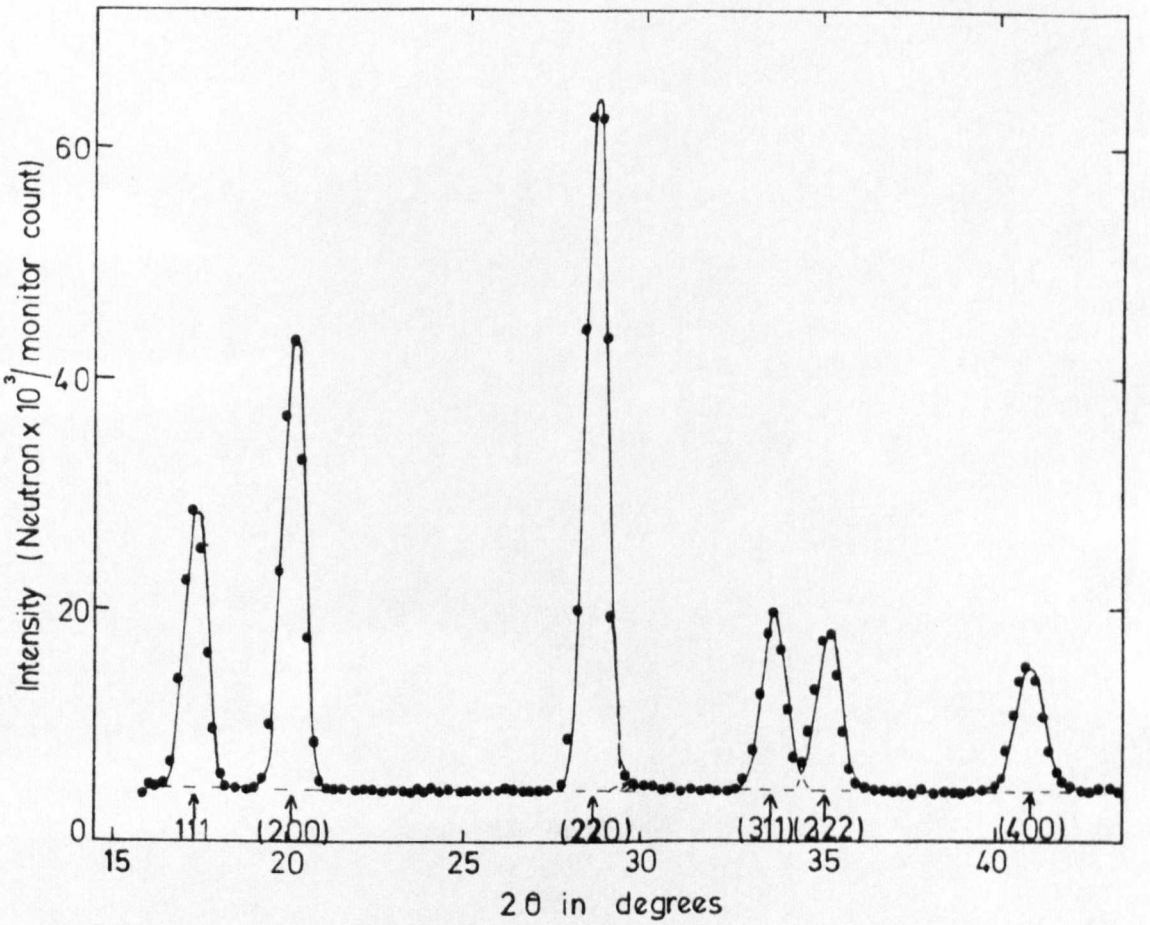

Fig. 6·9 Neutron diffraction pattern of Ni_2MnSn at 293°K

if it is assumed that the entire magnetic moment resides on the Mn atoms.

TABLE 6.14

hkl	Calculated intensities			Measured intensities
	Nuclear		$L2_1$ (total)	
	$L2_1$	DO_3	$\mu_{0,293} = 2.53$	
111	167	0.3	199	226
200	328	0.2	344	353
220	573	573	583	(583)
311	141	0.2	149	162
222	151	0.1	153	153
400	140	140	141	142

6.5 Ni_2MnSb

Castelliz (1951) investigated a series of alloys in the Ni-Mn-Sb system and found a continuous transition from NiMnSb to Ni_2MnSb. The alloy at the composition Ni_2MnSb had a lattice parameter 6.001 kX, a Curie temperature 140°C, and a saturation moment $\mu = 3.5\ \mu_B$. Under certain conditions of heat treatment, some of the alloys had bends in their σ, T curves typical of a 2 phase magnetic structure.

A 20 g ingot was made at the composition Ni_2MnSb. After annealing at 800°C for 24 h, one sample was quenched and another was slow-cooled. An X-ray photograph taken of the quenched sample was as expected for a Heusler alloy at this composition. The results are shown in table (6.15).

The X-ray photograph taken of the slow-cooled specimen exhibited a

few additional lines, and the main lines were slightly blurred, indicating the formation of an additional phase at some intermediate temperature.

TABLE 6.15

Density g/cm^3	a_0 from density	a_0 Measured	$F^2(\theta = 0)$ Calculated (111)	(200)	(220)	Structure
			676	400	17424	$L2_1$
9.0	6.0 A	6.000 A	538	676	17424	$F\bar{4}3m$
			576	576	17424	DO_3

The magnetic isothermals for the quenched alloy are shown in figure (6.10) and the spontaneous magnetization curve in figure (6.15). The principal features are summarized in table (6.16).

TABLE 6.16

θ_F (°K)	σ_{00} (emu/g)	μ_{00} (μ_B)
360 ± 4	62.1 ± 1	3.27 ± 0.05

The shape of the σ, T curve differs from that of most ferromagnets in that the approach to the Curie point is only gradual. In addition, the measured magnetic moment is significantly less than that of most other Heusler alloys.

The neutron diffraction pattern recorded at 293°K is shown in figure (6.11), and the measured and calculated intensities are compared in table (6.17). Debye temperature corrections were made using a mean atomic weight 74, and a Debye temperature 314°K. The agreement is

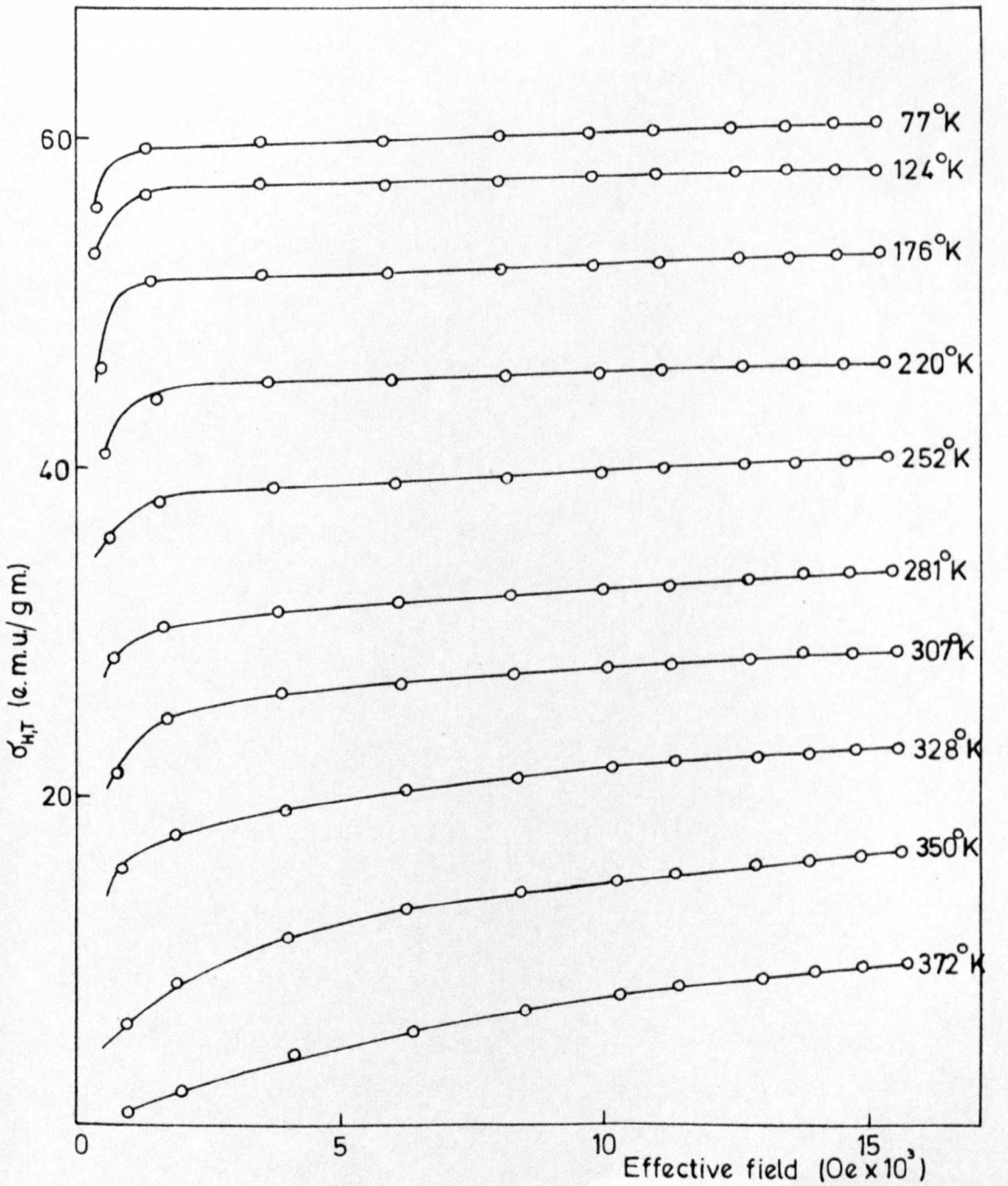

Fig. 6.10 Magnetic isotherms of Ni_2MnSb

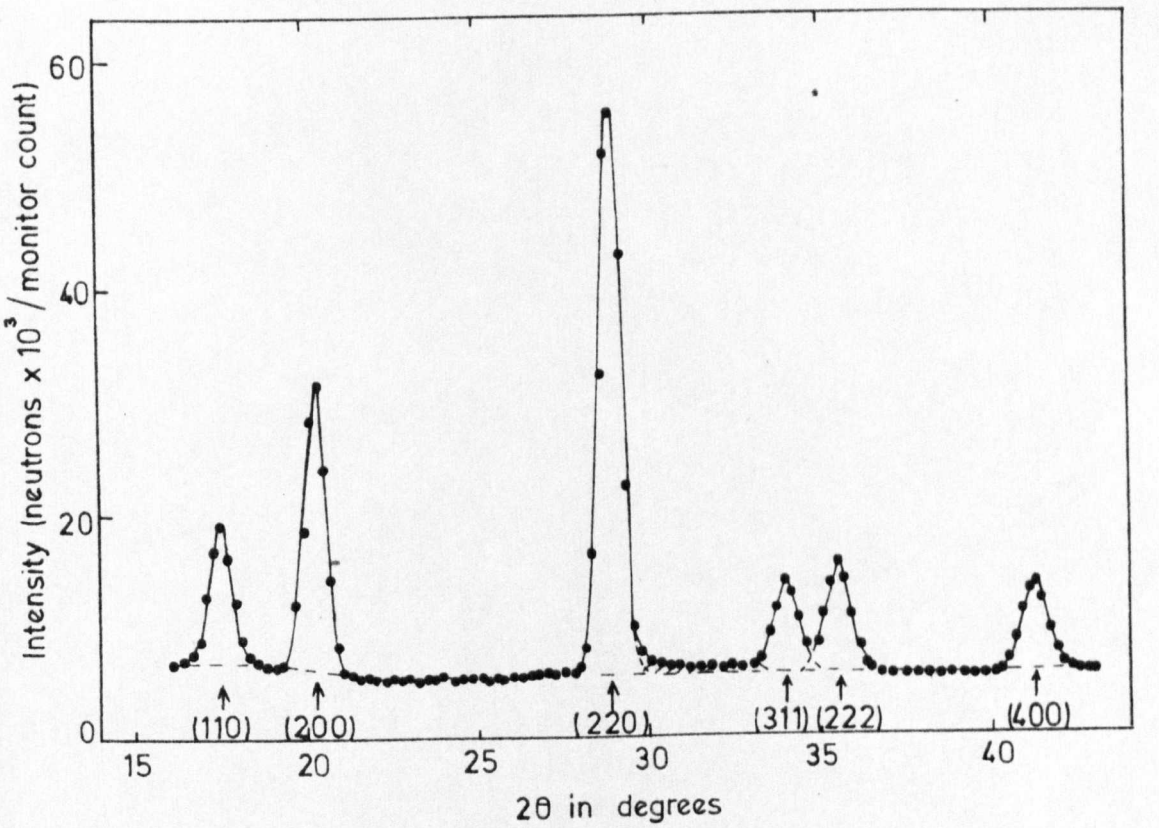

Fig. 6·11 Neutron diffraction pattern of Ni_2MnSb at 293°K

sufficient to show that the alloy has basically the $L2_1$ structure, and the results are consistent with the assumption that the moments are confined to the Mn atoms.

TABLE 6.17

hkl	Calculated intensities		Measured intensities
	Nuclear $L2_1$	S = 0.90 $\mu_{0,293}$ = 1.55	
111	142	116	128
200	348	265	238
220	503	506	(506)
311	120	92	95
222	160	121	123
400	130	130	113

Better agreement could be achieved if it is assumed that the presence of a small amount of additional phase results in a departure from stoichiometry. The additional phase, if ferromagnetic, could be the cause of the unusual shape of the magnetization curve.

6.6 NiMnSb

Castelliz (1951) reported that the alloy at the composition NiMnSb had the Cl_b structure with a lattice parameter 5.903 kX. The alloy was ferromagnetic with a Curie temperature 450°C, and a saturation moment 3.8 μ_B.

A 20 g ingot was made at the composition NiMnSb with a loss in weight on melting of 2%. The alloy was annealed at 800°C for 48 h and then

quenched. An X-ray photograph was taken, and the results are shown in table (6.18). The calculated F^2 values for the 3 possible Cl_b structures are shown for comparison.

TABLE 6.18

Density g/cm^3	a_0 from density	a_0 Measured	$F^2(\theta = 0)$ Calculated (111)	(200)	(220)	Structure Cl_b
			1460	2304	10816	1. NiMn-Sb
7.5	5.92 A	5.929 A	1154	2916	10816	2. NiMnSb-
			2604	4	10816	3. Ni-MnSb

The lattice parameters are in good agreement, and the superlattice lines were of the intensity expected for structure (1), although structure (2) could not be entirely ruled out. No additional lines were observed. The magnetic isothermals are shown in figure (6.12) and the spontaneous magnetization curve in figure (6.13). The principal magnetic features are summarized in table (6.18).

TABLE 6.18

θ_F (°K)	σ_{00} (emu/g)	μ_{00} (μ_B)
735 ± 5	96.3 ± 1	4.05 ± 0.05

The neutron diffraction pattern taken at 293°K is shown in figure (6.14) and the measured and calculated intensities, corrected for the effects of temperature using a mean atomic weight of 78 and an estimated Debye temperature of 294°K, are compared in table (6.19).

The excellent agreement confirms that the alloy has the Cl_b

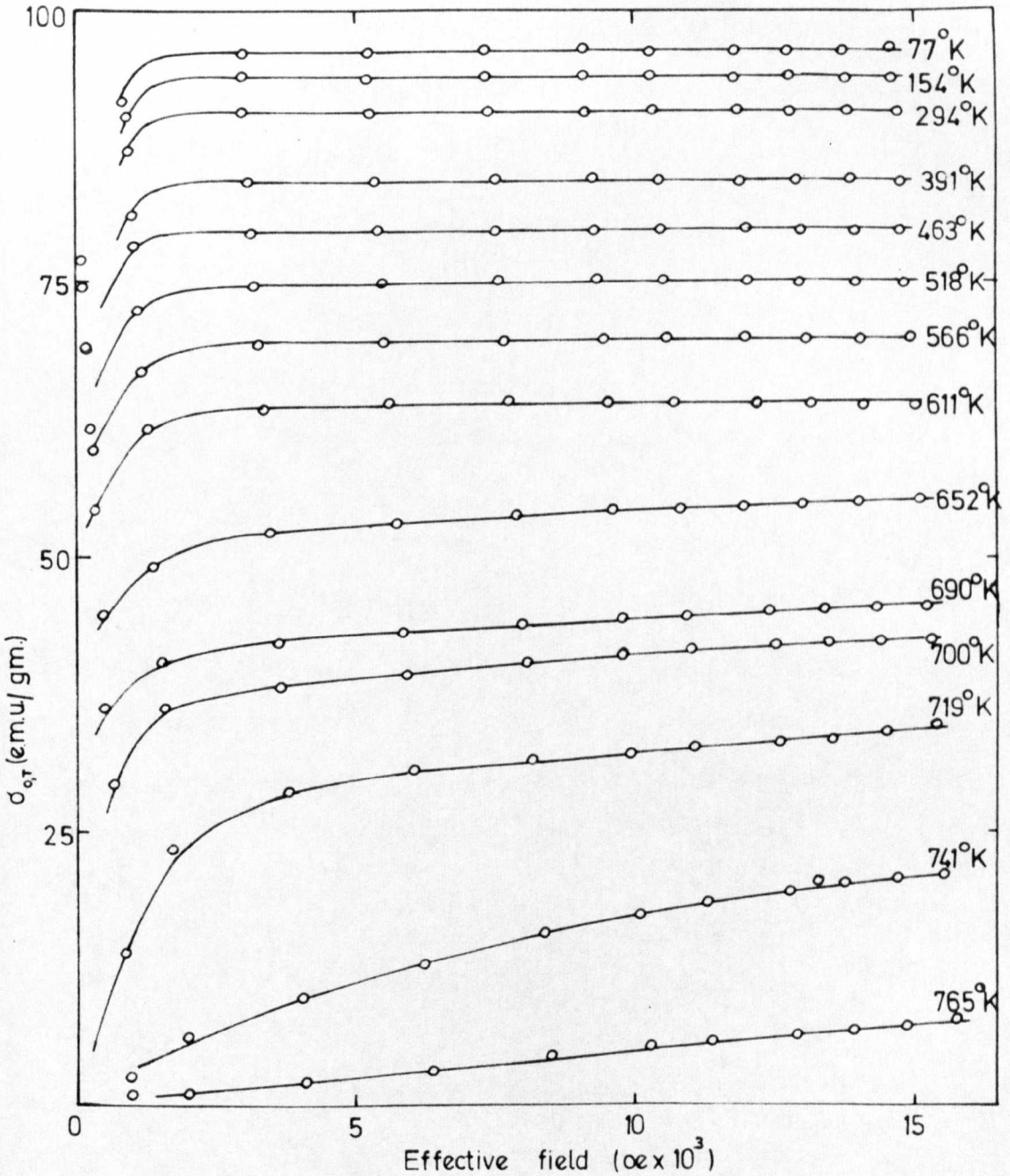

Fig 6·12 Magnetic isotherms of Ni MnSb

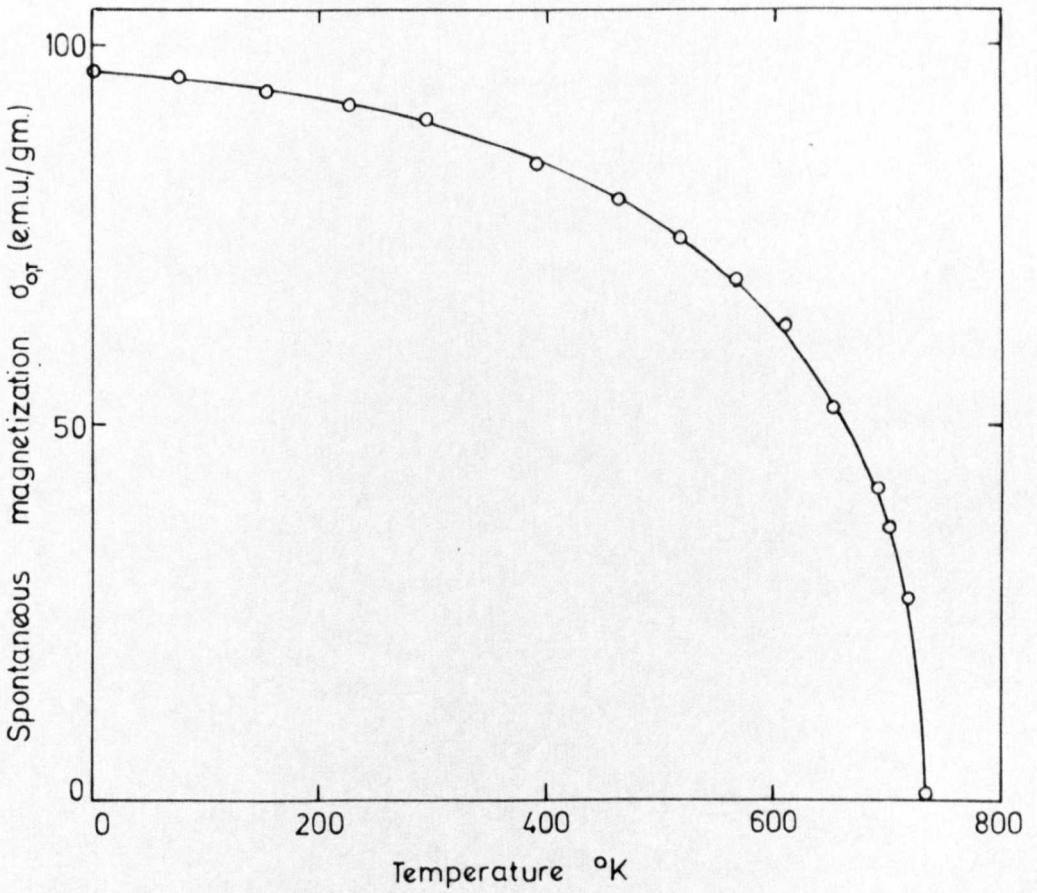

Fig. 6.13 Spontaneous magnetization $\sigma_{o,T}$ versus temperature for the alloy Ni Mn Sb.

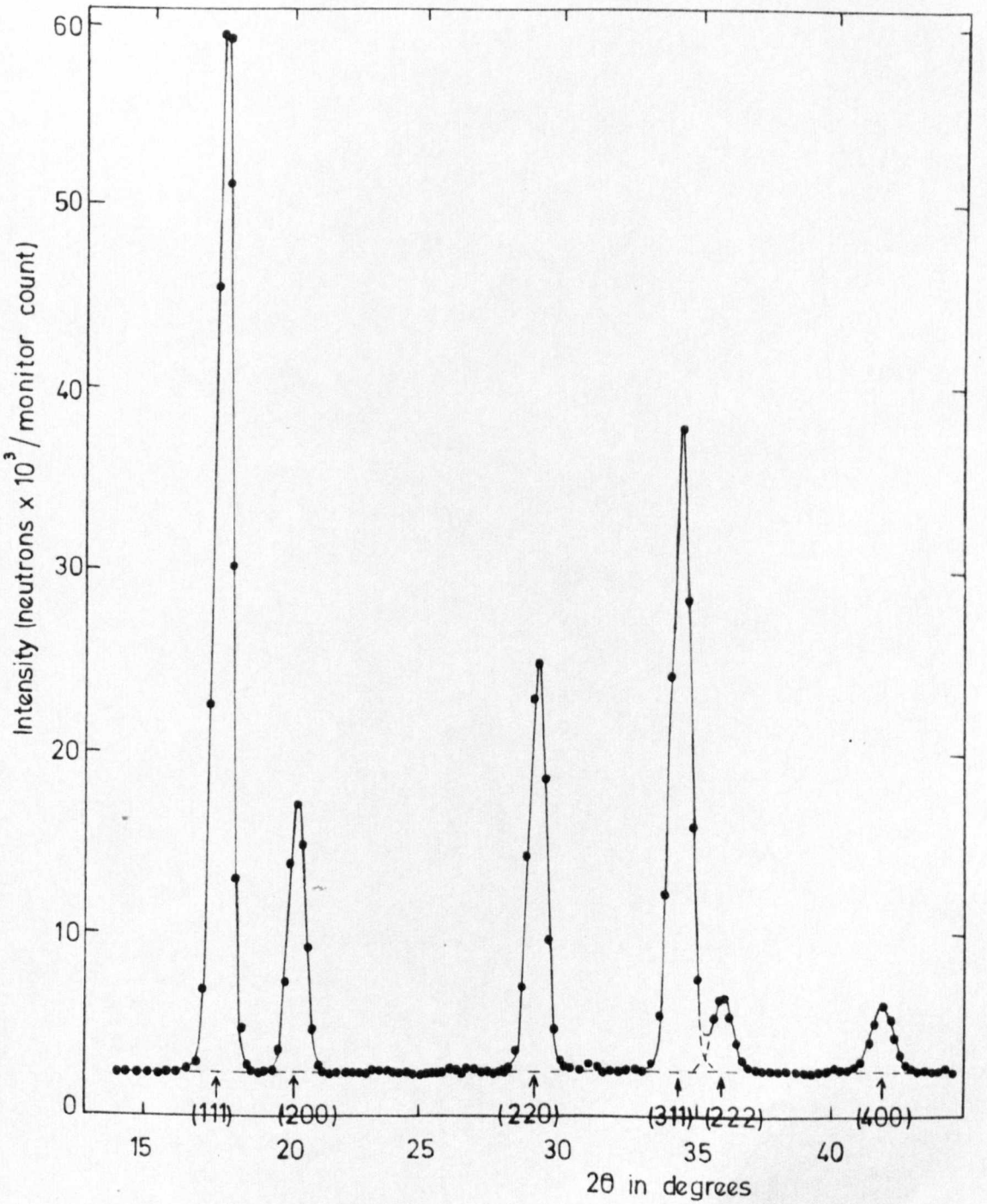

Fig. 6.14 Neutron diffraction pattern of NiMnSb at 293°K

structure (1), with a small amount of random disorder, and the magnetic moments are confined to the Mn atoms.

TABLE 6.19

	Total intensities			
	Calculated $\mu_{0,293} = 3.78$			
hkl	Cl_b 1. NiMn-Sb	Cl_b 2. NiMnSb-	S = 0.985 1. NiMn-Sb	Measured
111	386	130	374	379
200	102	391	99	99
220	161	161	161	(161)
311	286	70	277	274
222	36	169	35	35
400	38	38	38	37

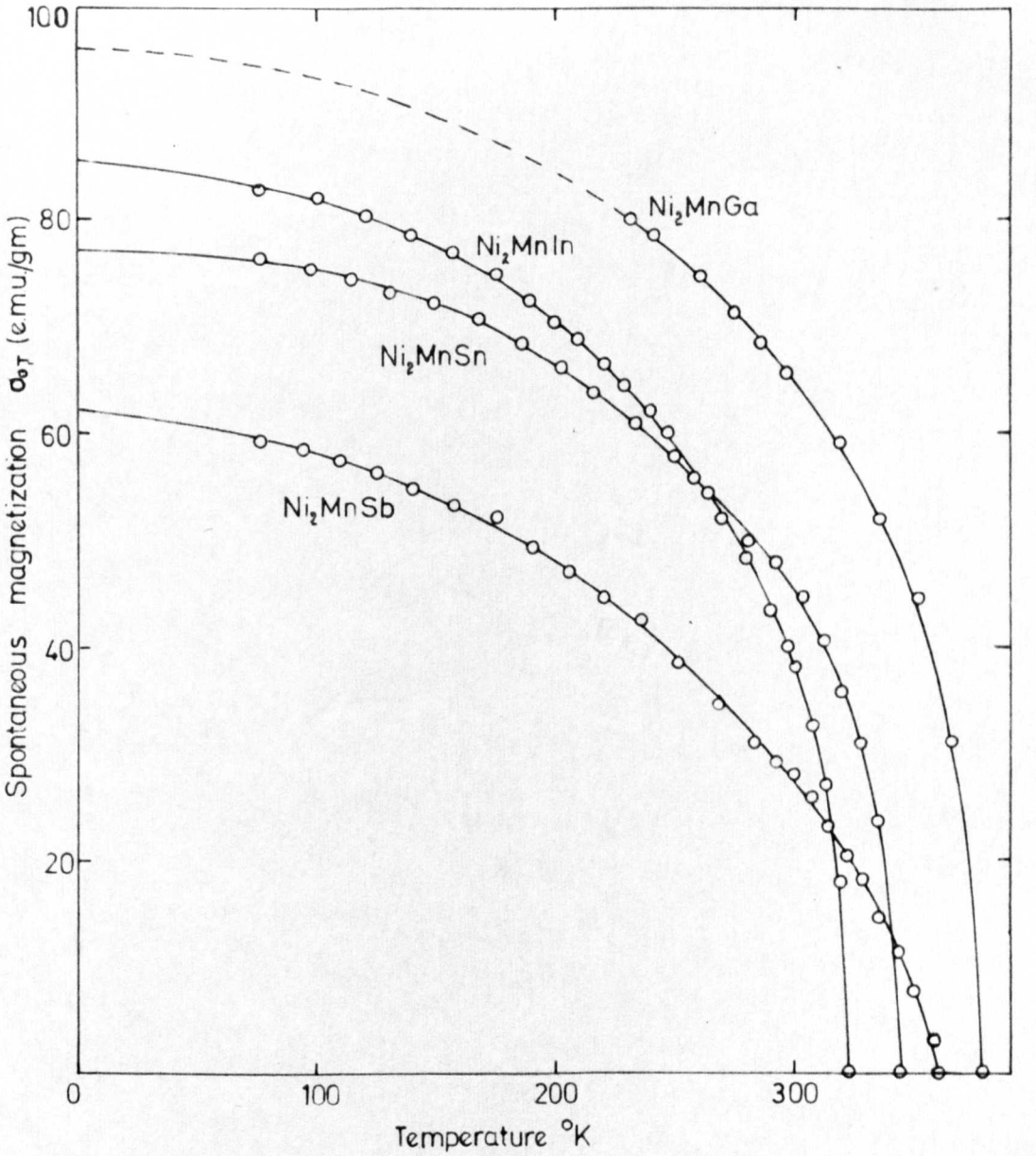

Fig. 6·15 Spontaneous magnetization σ_{oT} versus temperature for the alloys Ni_2MnGa, Ni_2MnIn, Ni_2MnSn, and Ni_2MnSb.

CHAPTER 7

Experimental results - Co_2MnX and CoMnX

7.1 Co_2MnAl

Alloys in the ternary system Co-Mn-Al have been investigated by Raynor (1945), but only in the Al rich region with up to 5.6% Mn and 4.0% Co.

A 20 g ingot was made at the composition Co_2MnAl with a loss in weight on melting of 2.4%. The alloy was annealed at 720°C for 24 h, and then quenched. An X-ray photograph was taken and the measured and calculated results are compared in table (7.1).

TABLE 7.1

Density g/cm^3	a_0 from density	a_0 Measured	$F^2(\theta = 0)$ Calculated (111)	(200)	(220)	Structure
			144	256	8464	$L2_1$
6.90	5.77 A	5.756 A	340	144	8464	$F\bar{4}3m$
			0	256	8464	B2

The lattice parameters are in reasonable agreement, but the odd superlattice lines were absent, indicating a B2 structure or a large amount of preferential Mn-Al disorder. In addition there were a few extra weak lines which were indexed as f.c.c. with a lattice parameter 3.628 A.

The alloy lost an unusually large amount of weight on melting, and this could have been mainly Al. If so, this would be expected to leave vacancies in the $L2_1$ or B2 structure, or an excess of Co and Mn.

Schneider and Wunderlich (1949) investigated the binary Co-Mn system and have shown that at most compositions the structure is f.c.c., and at 57 At.% Mn the lattice parameter is 3.628 A.

As the intensities of the additional lines were only approximately 1% of the intensity of the main lines, the proportion of additional phase is also only approximately 1%. This is about the amount that would be expected if the main loss in weight on melting was Al.

The magnetic isothermals for the alloy are shown in figure (7.1), and the resulting spontaneous magnetization curve in figure (7.17). The principal magnetic features are summarized in table (7.2).

TABLE 7.2

θ_F (^oK)	σ_{00} (emu/g)	μ_{00} (μ_B)	$\mu_{0,293}$ (μ_B) Co	$\mu_{0,293}$ (μ_B) Mn
697 ± 3	112.1 ± 1	4.01 ± 0.04	0.61 ± 0.1	2.50 ± 0.2

The neutron diffraction pattern recorded at 293°K is shown in figure (7.2). The (111) and (311) peaks, which for the ordered Heusler alloy would be the most intense, are extremely weak, indicating that the alloy has the Heusler structure, but with a very large amount of preferential Mn-Al disorder. No additional peaks corresponding to the extra lines on the X-ray photograph were observed. This reinforces the suggestion that they were due to a small amount of binary Co-Mn alloy, since such an alloy would have an extremely small neutron scattering factor, and 1% would not be discernable from the background.

The total magnetic moment at 293°K is 3.72 μ_B, but it is not known

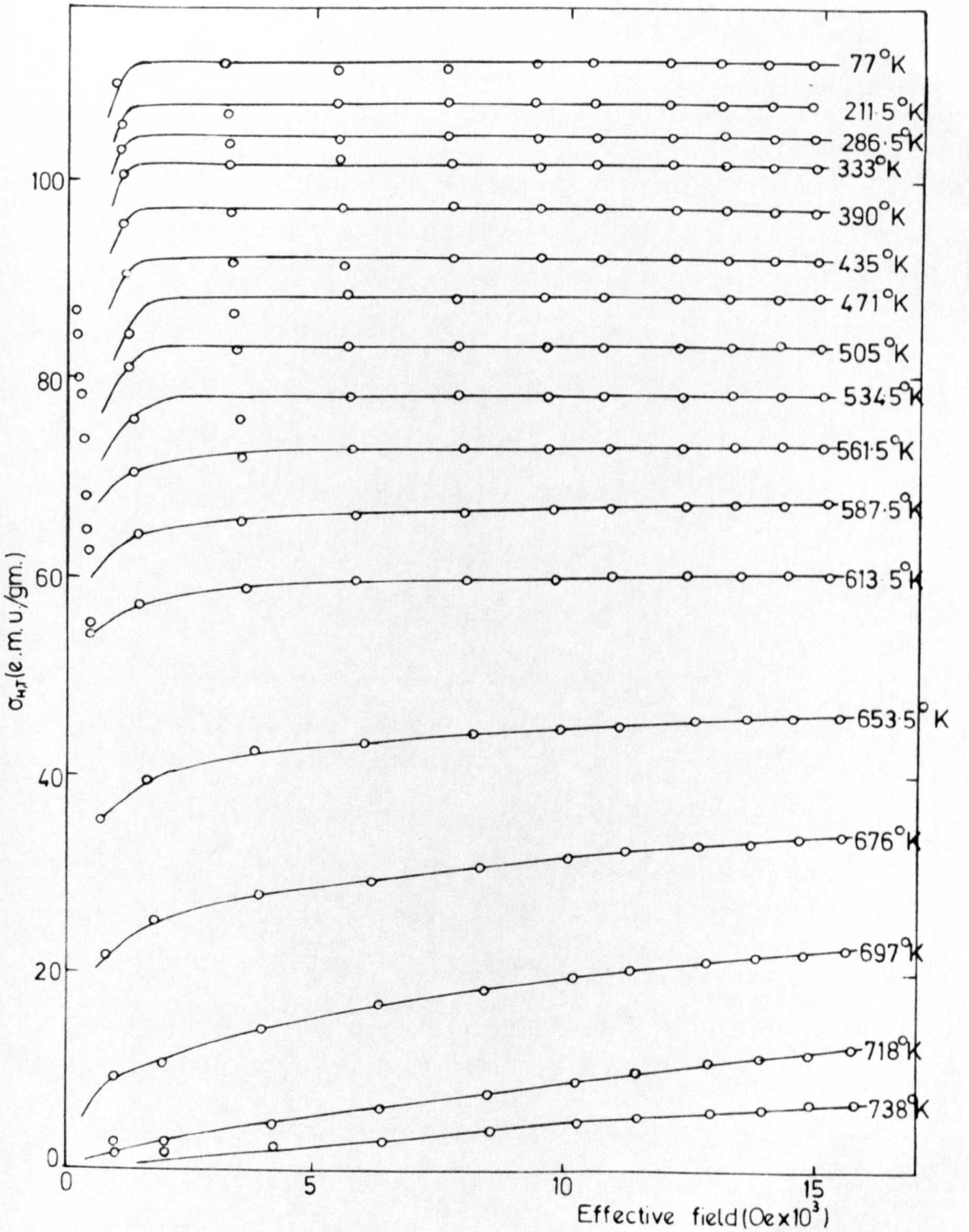

Fig 7·1 Magnetic isotherms of Co_2MnAl

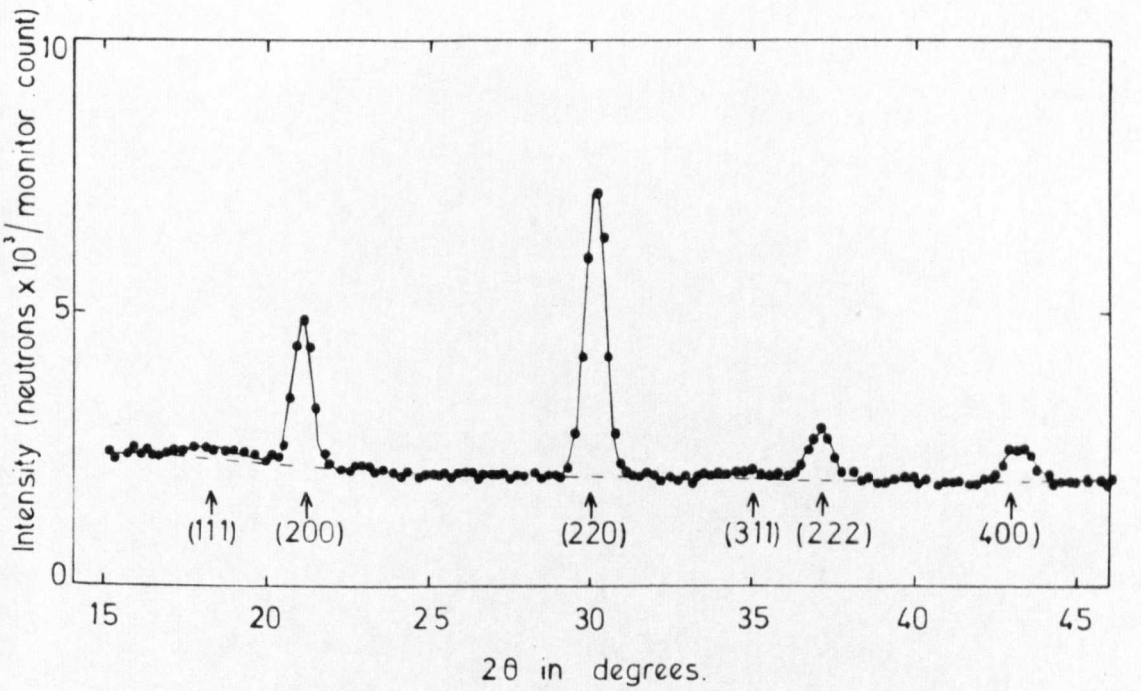

Fig. 7 2 Neutron diffraction pattern of Co_2MnAl at 293°K

what proportion is due to the Co atoms, and what is due to the Mn atoms. Furthermore, as Co and Mn have different magnetic form factors, the size of the magnetic contribution to the (220) line is not known. It is thus not possible to use the intensity of the (220) line directly for normalization purposes. However, since the ratios of the nuclear intensities of superlattice lines of the same group are not affected by disorder, and knowing the total magnetic moment, it is possible to derive approximate values for the magnetic contributions to the (200) and (222) superlattice lines. Resubstitution, followed by a regression analysis to obtain the best fit between measured and calculated intensities, resulted in the intensities shown in table (7.3).

TABLE 7.3

hkl	Calculated intensities			Measured intensities
	Nuclear	$\mu(Co) = 0.61$, $\mu(Mn) = 2.50$		
	$L2_1$	$L2_1$	S = 0.93 $\alpha(Mn-Al) = 0.4$	
111	80.8	107.7	4.1	4.9
200	23.6	25.2	22.0	22.0
220	22.2	43.5	43.5	(43.5)
311	68.6	74.7	2.8	2.2
222	10.9	11.2	9.8	9.7
400	5.8	7.6	7.6	7.8

Temperature corrections were made using 50 as a mean atomic weight, and a Debye temperature of 383°K.

It is clear from the agreement between the measured and calculated intensities that there is a small amount of random disorder, almost complete Mn-Al disorder, and a substantial moment on the Co atoms.

7.2 Co_2MnSi

No references were found to any ternary alloys in the Co-Mn-Si system.

A 20 g ingot was made at the composition Co_2MnSi with a loss in weight on melting of 0.9%. The alloy was annealed at 720°C for 24 h, and then rapidly quenched. An X-ray photograph was taken, and the measured and calculated results are compared in table (7.4).

TABLE 7.4

Density g/cm^3	a_0 from density	a_0 Measured	$F^2(\theta = 0)$ Calculated (111)	(200)	(220)	Structure
			121	225	8649	$L2_1$
7.40	5.65A	5.654 A	313	121	8649	$F\bar{4}3m$
			0	225	8649	B2

The lattice parameters are in excellent agreement, and visually the superlattice lines were as expected for the $L2_1$ structure.

The magnetic isothermals are shown in figure (7.3) and the resulting spontaneous magnetization curve in figure (7.17). The principal magnetic features are summarized in table (7.5).

TABLE 7.5

θ_F (°K)	σ_{00} (emu/g)	μ_{00} (μ_B)	$\mu_{0,293}$ (μ_B) Co	$\mu_{0,293}$ (μ_B) Mn
985 ± 5	141.0 ± 1	5.07 ± 0.04	0.74 ± 0.07	3.52 ± 0.14

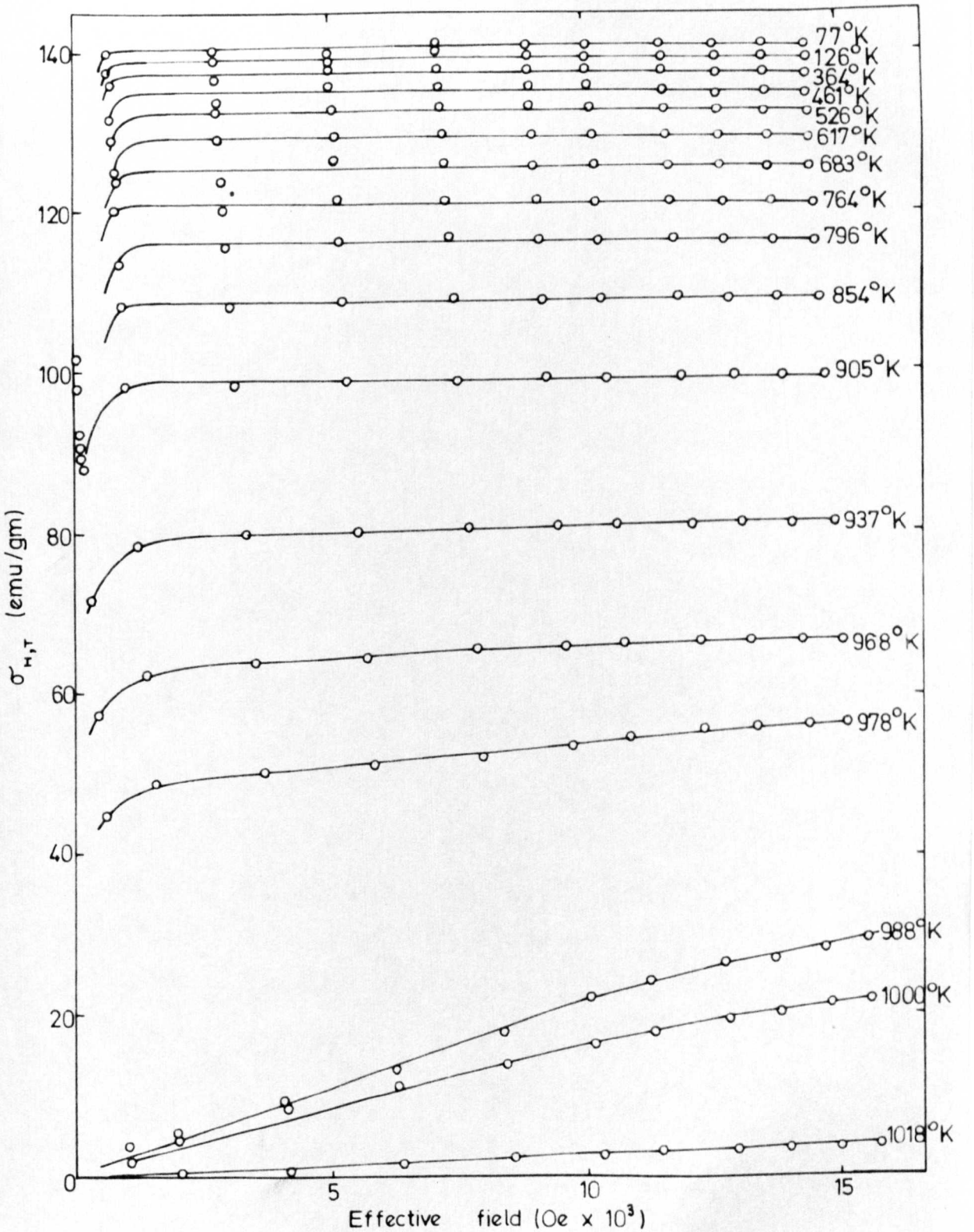

Fig. 7.3 Magnetic isotherms of Co_2MnSi.

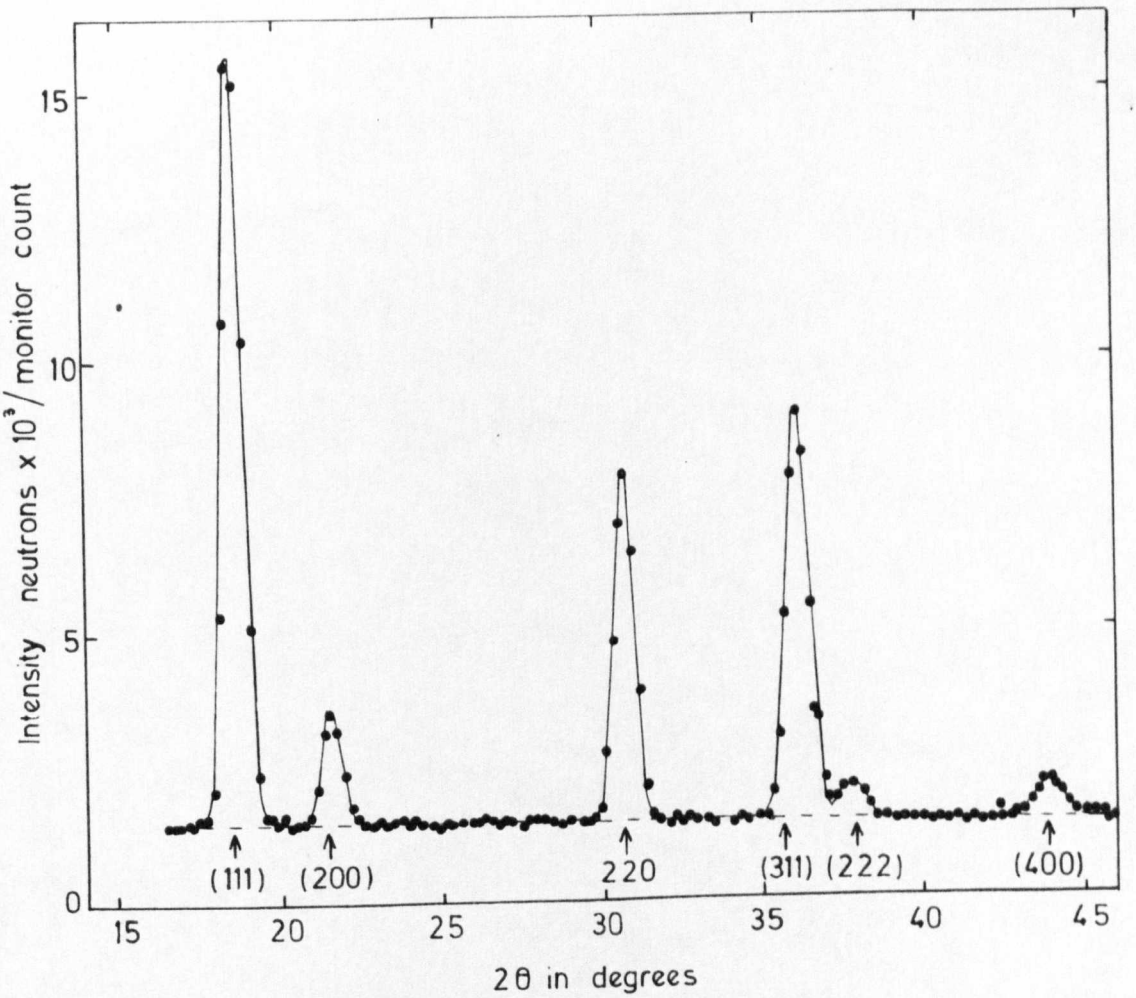

Fig. 74 Neutron diffraction of Co_2MnSi at 293° K

The neutron diffraction pattern recorded at 293°K is shown in figure (7.4). In contrast to Co_2MnAl the alloy is clearly highly ordered in the $L2_1$ structure, and the odd superlattice lines may be used to determine the positions and magnitudes of the magnetic moments. The measured and calculated intensities are compared in table (7.6). The measured intensities were corrected for the effects of temperature using a Debye temperature 429°K, and a mean atomic weight of 50.

TABLE 7.6

hkl	Calculated intensities			Measured intensities
	Nuclear	$\mu(Co) = 0.74$, $\mu(Mn) = 3.52$		
	$L2_1$	$L2_1$	S = 0.97	
111	94.2	143	135	136
200	16.9	21.5	20.2	18.9
220	28.0	62.5	62.5	(62.5)
311	80.0	90.8	85.4	85.0
222	7.8	8.0	7.5	8.7
400	7.3	9.9	9.9	10.4

Good agreement is achieved for all the lines. There is a small amount of random disorder and a moment on both the Co and Mn atoms.

7.3 Co_2MnGa

Hames (1960) reported that an alloy at the composition Co_2MnGa was ferromagnetic and probably had the Heusler structure, but was unable to distinguish unambiguously between the Co, Mn, and Ga atoms. The same structure was obtained on quenching and furnace cooling, but with

slightly different lattice parameters, 5.77 A, and 5.78 A respectively.

A 20 g ingot was made at the composition Co_2MnGa with a loss in weight on melting of 0.4%. The specimen was annealed at 800°C for 24 h and quenched. Table (7.7) compares the calculated and measured X-ray data.

TABLE 7.7

Density g/cm^3	a_0 from density	a_0 Measured	$F^2(\theta = 0)$ Calculated (111)	(200)	(220)	Structure
			36	4	12100	$L2_1$
8.44	5.76 A	5.770 A	20	36	12100	$F\bar{4}3m$
			25	25	12100	DO_3

The odd superlattice lines were very weak but distinct, but the even superlattice lines could not be resolved, as expected for the $L2_1$ structure.

The magnetic isothermals are shown in figure (7.5) and the spontaneous magnetization curve in figure (7.17). The main features are summarized in table (7.8).

TABLE 7.8

θ_F (°K)	σ_{00} (emu/g)	μ_{00} (μ_B)	$\mu_{0,293}$ (μ_B) Co	$\mu_{0,293}$ (μ_B) Mn
694 ± 3	93.3 ± 1	4.05 ± 0.04	0.49 ± 0.05	2.82 ± 0.1

A neutron diffraction pattern was recorded at 293°K, and is shown in figure (7.6). The measured intensities were corrected for the effects

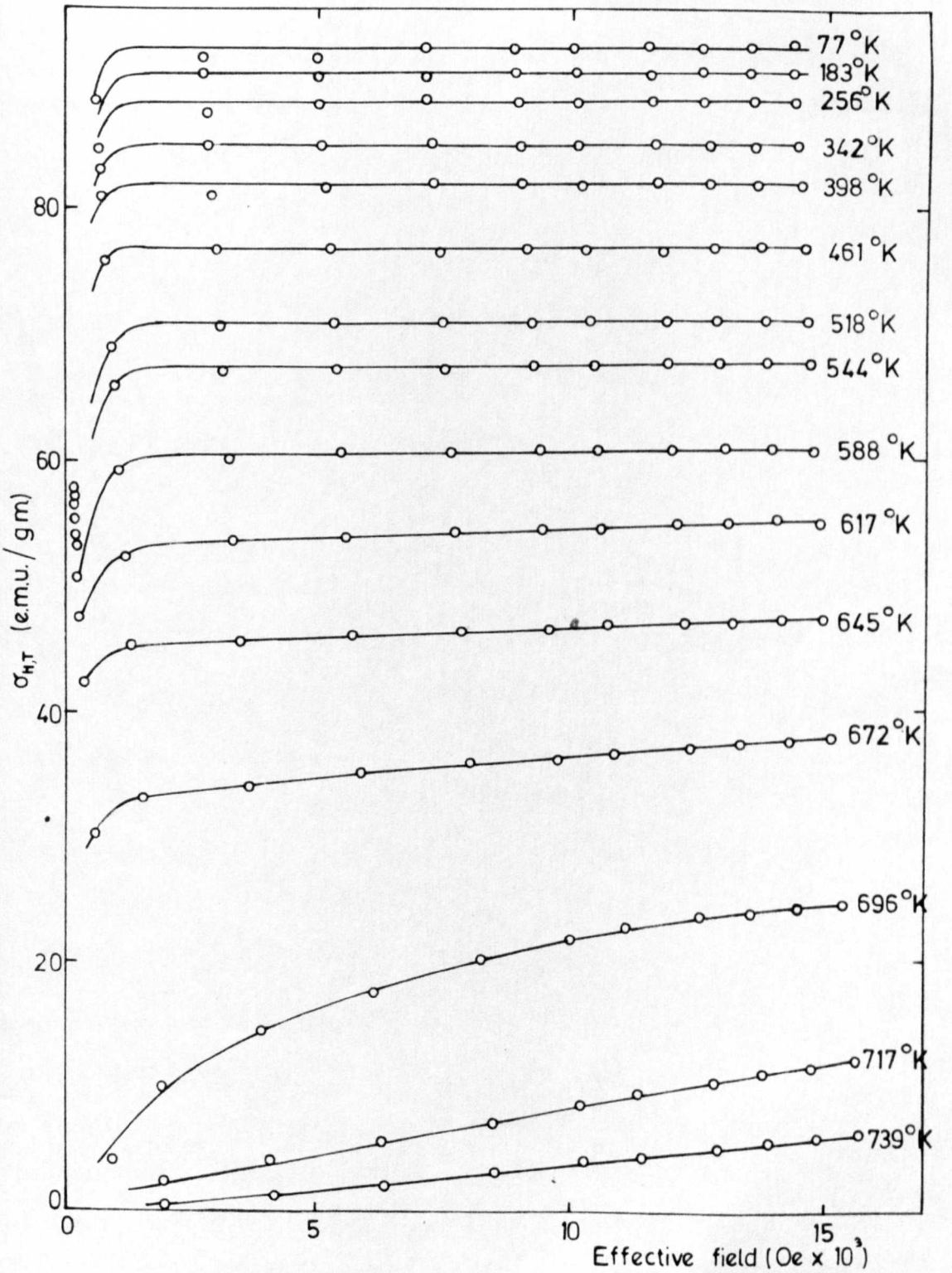

Fig. 7.5 Magnetic isotherms of Co_2MnGa

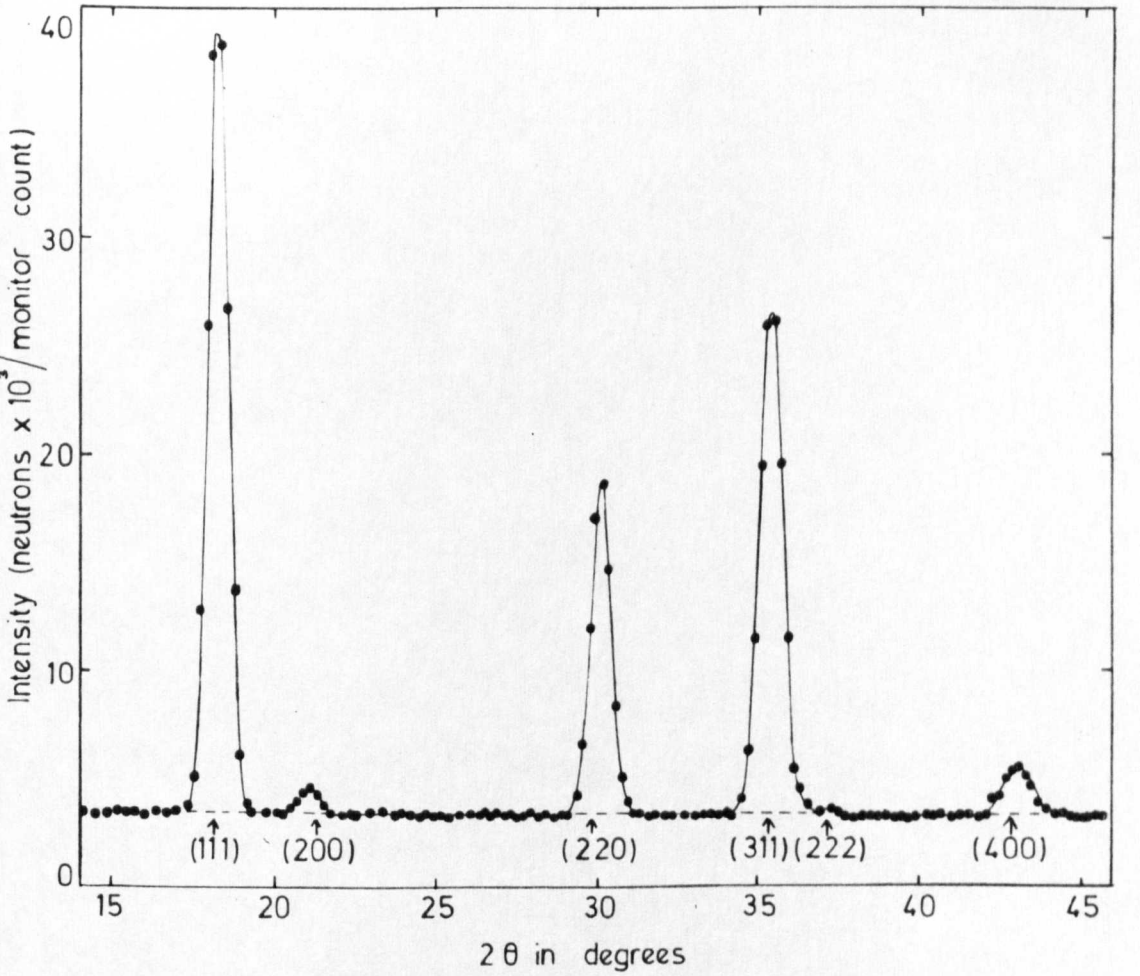

Fig. 7 6 Neutron diffraction pattern of Co_2MnGa at 293° K

of temperature using an estimated Debye temperature of 316°K, and a mean atomic weight of 61. The measured and calculated intensities are compared in table (7.9).

TABLE 7.9

hkl	Calculated intensities			Measured intensities
	Nuclear	$\mu(Co) = 0.49$, $\mu(Mn) = 2.82$		
	$L2_1$	$L2_1$	S = 0.96	
111	188	222	204	202
200	1.8	6.7	6.2	6.8
220	68.6	89.6	89.6	(89.6)
311	160	167	154	156
222	0.8	1.2	1.1	1.0
400	17.8	19.4	19.4	19.3

It is noted that, even when fully ordered in the $L2_1$ structure, the nuclear contributions to the even superlattice lines are very small, and hence the magnetic contributions may be assessed very accurately. It is clear from the results that apart from the lack of any tendency for preferential Mn-Ga disorder, this alloy has very similar properties to Co_2MnAl.

7.4 Co_2MnGe

The only ternary alloy in the system Co-Mn-Ge to be reported was by Castelliz (1953), who reported that CoMnGe crystallized in a hexagonal $B8_2$ structure.

A 20 g ingot was made at the composition Co_2MnGe with a loss in

weight on melting of 0.7%. After annealing at 800°C for 24 h, the alloy was quenched. An X-ray photograph was taken, and the measured and calculated results are compared in table (7.10).

TABLE 7.10

Density g/cm^3	a_0 from density	a_0 Measured	$F^2(\theta = 0)$ Calculated (111)	(200)	(220)	Structure
			49	9	12321	$L2_1$
8.50	5.76 A	5.743 A	29	49	12321	$F\bar{4}3m$
			36	36	12321	DO_3

The lattice parameters are in good agreement, and the superlattice line intensities were as expected for the $L2_1$ structure. The odd lines were very weak but clearly visible, but only one extremely faint even superlattice line could be resolved.

The magnetic isothermals are shown in figure (7.7) and the spontaneous magnetization curve in figure (7.17). The principal features are summarized in table (7.11).

TABLE 7.11

θ_F (°K)	σ_{00} (emu/g)	μ_{00} (μ_B)	$\mu_{0,293}$ (μ_B) Co	$\mu_{0,293}$ (μ_B) Mn
905 ± 3	116.3 ± 1	5.11 ± 0.04	0.72 ± 0.08	3.48 ± 0.16

The neutron diffraction pattern recorded at 293°K is shown in figure (7.8). The measured intensities were corrected for the effects of temperature using an estimated Debye temperature 357°K and a mean

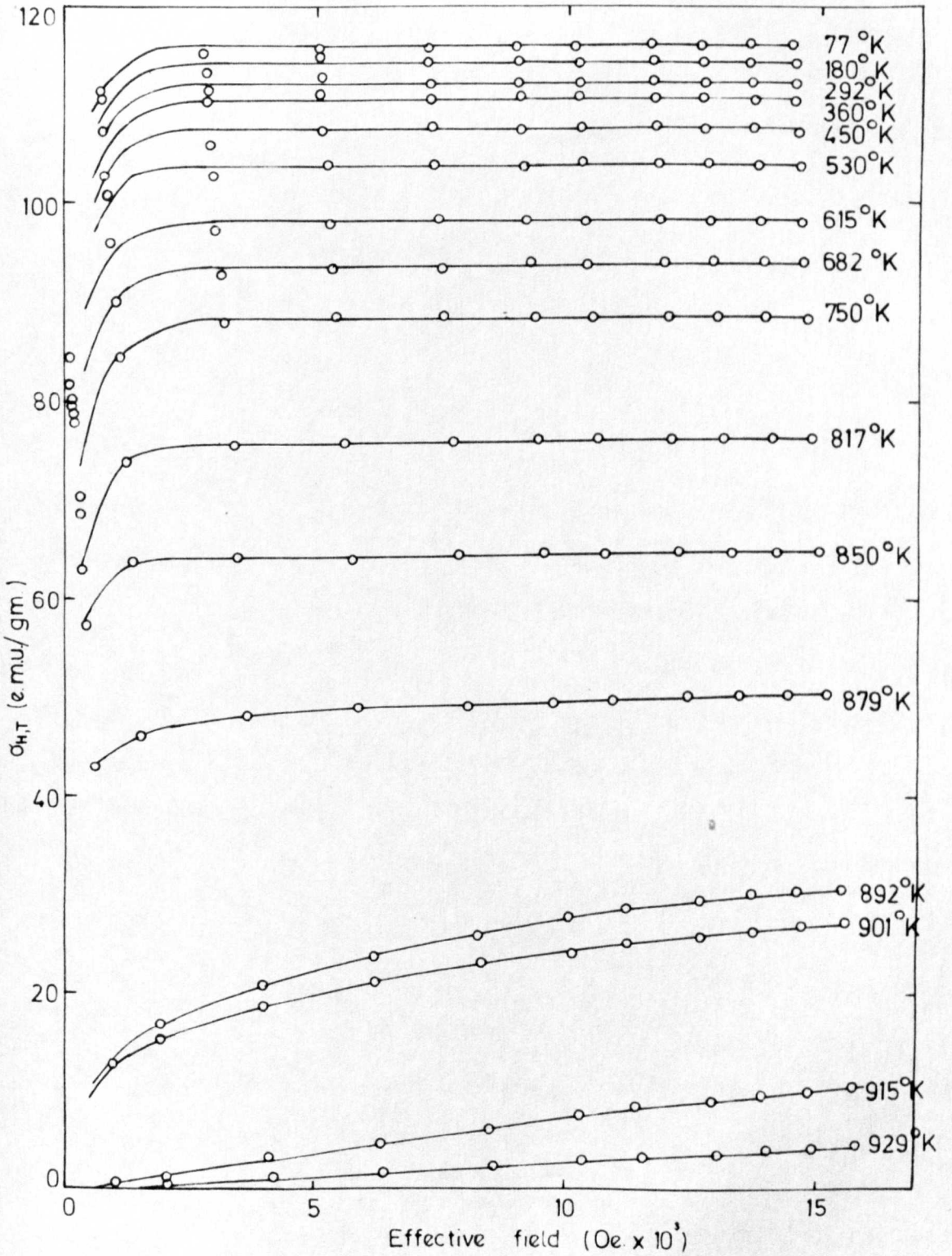

Fig. 7.7 Magnetic isotherms of Co_2MnGe

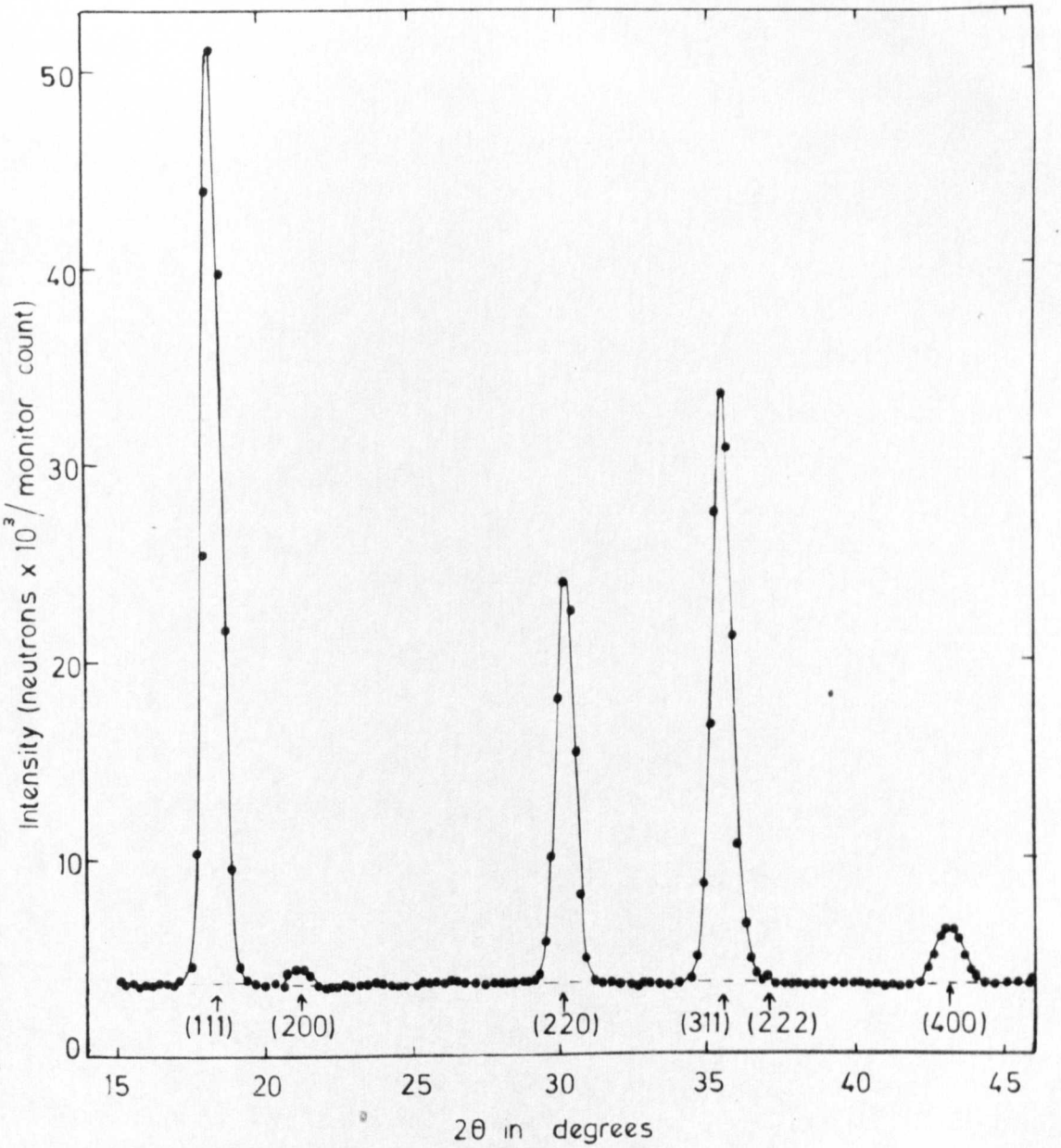

Fig. 7.8 Neutron diffraction pattern of $Co_2Mn\,Ge$ at 293°K

atomic weight of 61. The measured and calculated intensities are compared in table (7.12).

TABLE 7.12

hkl	Calculated intensities			Measured intensities
	Nuclear	$\mu(Co) = 0.72$, $\mu(Mn) = 3.48$		
	$L2_1$	$L2_1$	S = 0.97	
111	231	283	266	258
200	0.04	5.2	4.9	5.1
220	88.2	124	124	(124)
311	195	207	195	202
222	0.02	0.3	0.3	0.5
400	22.9	25.7	25.7	25.8

In this alloy, the nuclear comtributions to the (200) and (222) peaks are virtually zero and hence the magnetic contributions may be assessed very accurately.

The magnetic moment distribution within the alloy is very similar to that of Co_2MnSi.

7.5 Co_2MnIn

An attempt was made to form an alloy at the composition Co_2MnIn, but the In did not go into solution.

7.6 Co_2MnSn

Castelliz (1953) reported that an alloy at the composition Co_2MnSn had the Heusler structure with a lattice parameter 5.977 kX. The structure was verified by Kripyakevich et al (1954), but with a slightly different

lattice parameter 5.991 kX. Oxley (1964) measured the magnetization from 77°K to 293°K and derived a value of $\mu_{00} = 5.0\ \mu_B$ per Co_2MnSn group.

A 20 g ingot was made at the composition Co_2MnSn with a loss in weight on melting of 0.7%. The alloy was annealed at 720°C for 48 h and then quenched. An X-ray photograph was taken and the measured and calculated results are compared in table (7.13).

TABLE 7.13

Density g/cm^3	a_0 from Density	a_0 Measured	$F^2(\theta = 0)$ Calculated (111)	(200)	(220)	Structure
			625	441	16641	$L2_1$
8.68	6.06 A	6.000 A	533	625	16641	$F\bar{4}3m$
			586	586	16641	DO_3

The lattice parameters are in good agreement, and the line intensities were as expected for the $L2_1$ structure. Both sets of superlattice lines were weak but clear, but with the odd lines rather more intense than adjacent even lines.

The magnetic isothermals are shown in figure (7.9) and the spontaneous magnetization curve in figure (7.17). The principal features are summarized in table (7.14).

TABLE 7.14

θ_F (°K)	σ_{00} (emu/g)	μ_{00} (μ_B)	$\mu_{0,293}$ (μ_B) Co	$\mu_{0,293}$ (μ_B) Mn
829 ± 4	97.4 ± 1	5.08 ± 0.05	0.72 ± 0.08	3.48 ± 0.16

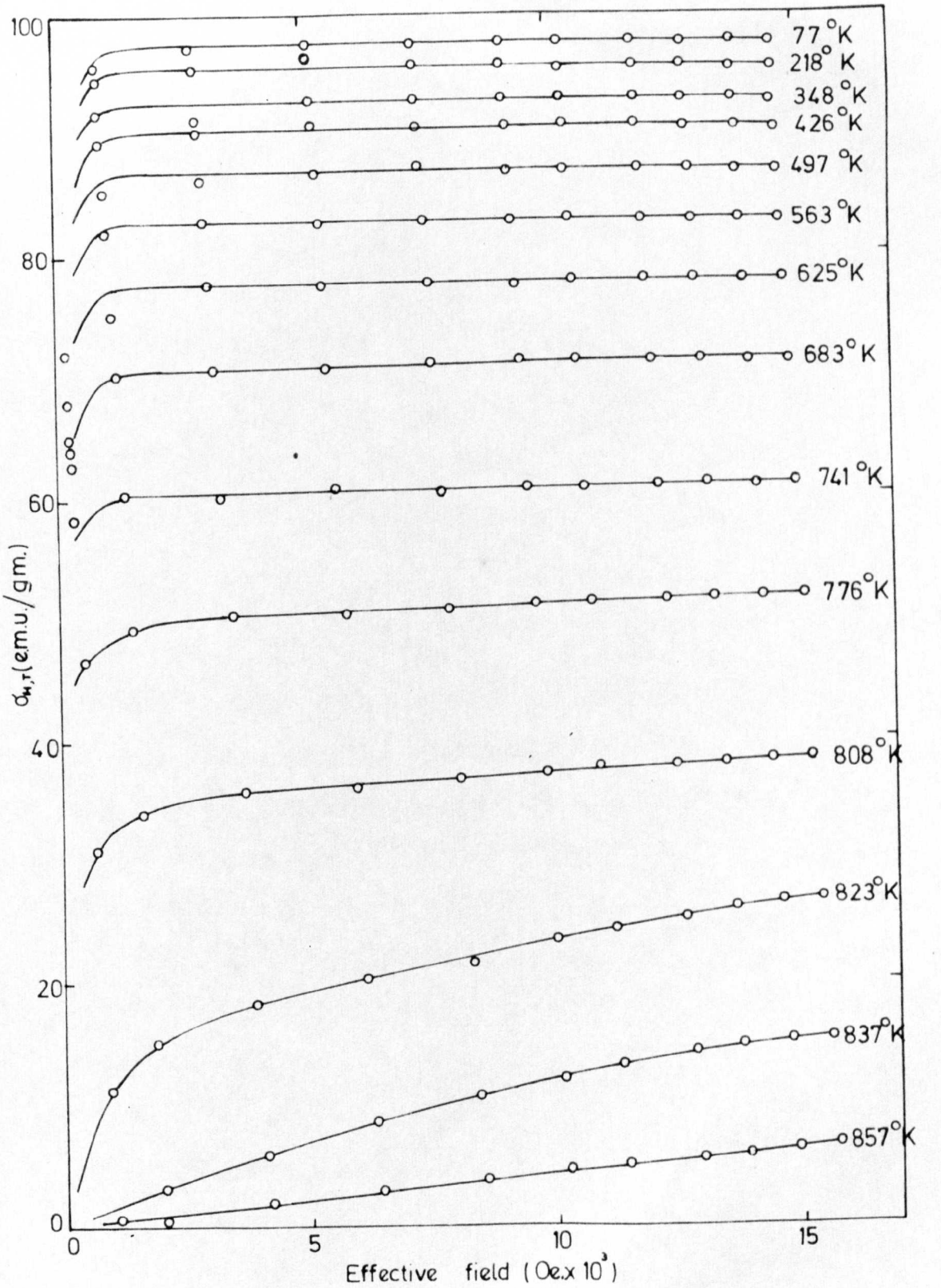

Fig. 7·9 Magnetic isotherms of Co_2MnSn

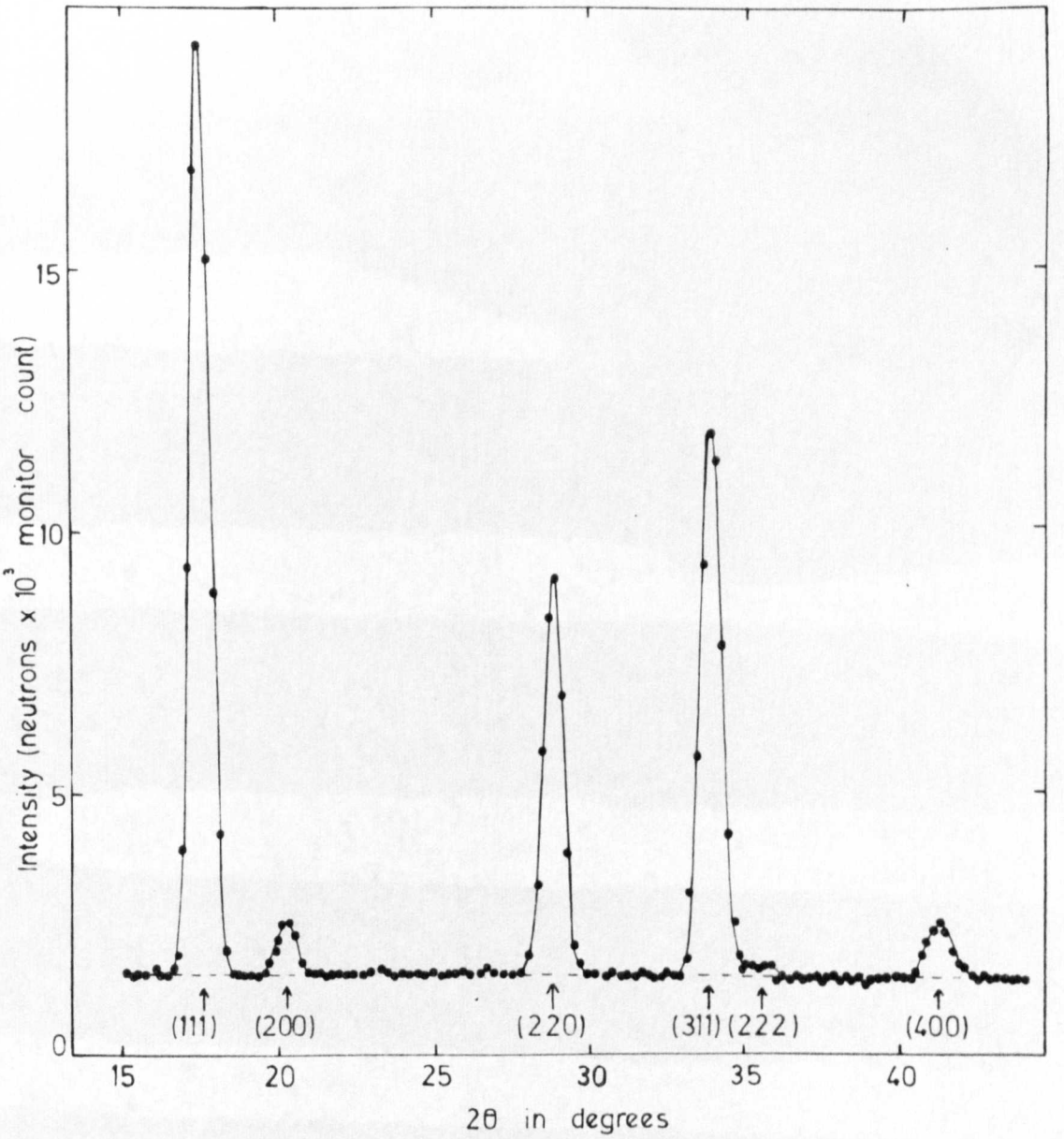

Fig. 7.10 Neutron diffraction pattern of Co_2MnSn at 293°K

The neutron diffraction pattern recorded at 293°K is shown in figure (7.10). The measured intensities were corrected for the effects of temperature using a mean atomic weight of 73, and an estimated Debye temperature of 349°K. The measured and calculated intensities are compared in table (7.15).

TABLE 7.15

hkl	Calculated intensities			Measured intensities
	Nuclear	$\mu(Co) = 0.72$, $\mu(Mn) = 3.48$		
	$L2_1$	$L2_1$	S = 0.985	
111	173	236	229	227
200	6.1	12.3	12.0	12.3
220	56.3	99.0	99.0	(99.0)
311	139	153	149	151
222	2.8	3.2	3.1	3.7
400	14.5	18.2	18.2	19.4

Exellent agreement is again obtained for this alloy, and its magnetic properties are very similar to those of Co_2MnSi and Co_2MnGe.

7.7 Co_2MnSb

No references could be found to any earlier investigations on an alloy at this composition.

A 20 g ingot was made at the composition Co_2MnSb, with a loss in weight on melting of 0.6%, but it was noticed on crushing that a small amount, 0.76 g, of Co was undissolved. After annealing at 720°C for 24 h the alloy was quenched. An X-ray photograph was taken and the

calculated and measured results are compared in table (7.16).

TABLE 7.16

Density g/cm^3	a_0 from density	a_0 Measured	$F^2(\theta = 0)$ Calculated (111)	(200)	(220)	Structure
			674	484	16900	$L2_1$
7.84	6.29 A	5.929 A	580	674	16900	$F\bar{4}3m$
			625	625	16900	DO_3

The lattice parameters are not in very good agreement, but the difference may be explained if it is assumed that there are some vacancies on the Co sites due to the undissolved cobalt. The intensities of the super-lattice lines were as expected for the $L2_1$ structure, but in addition several other weak lines were observed. They were indexed as f.c.c. with a lattice parameter 3.552 A. Cobalt has an f.c.c. structure with a_0 = 3.542 A, and Schneider and Wunderlich (1949) have shown that a Co-Mn alloy with approximately 8% Mn has a lattice parameter 3.552 A.

A comparison of the intensities of the extra lines with the main $L2_1$ lines indicated that the alloy was really a mixture of approximately 5 At.% free Co and 95 At.% $Co_{1.75}MnSb$.

The magnetic isothermals for the alloy are shown in figure (7.11). Up to about 600°K the isothermals are typical of a ferromagnet, but above that temperature the presence of an additional ferromagnetic phase with a very high Curie temperature becomes evident. The spontaneous magnetization curves are shown in figure (7.12). The curve for Co_2MnSb* is the measured curve for the mixture. The lower curve is the projected

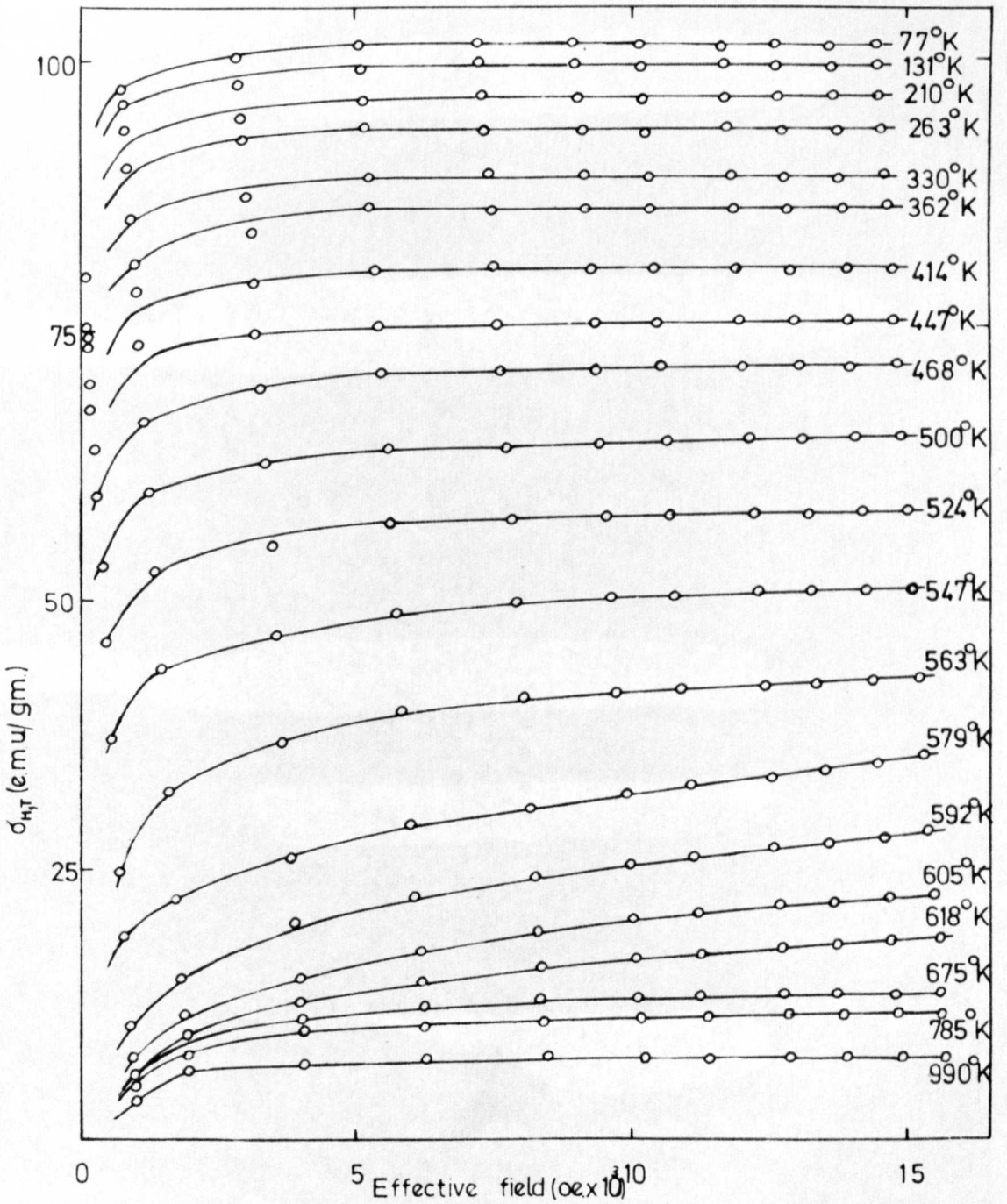

Fig. 7.11 Magnetic isotherms of Co_2MnSb*

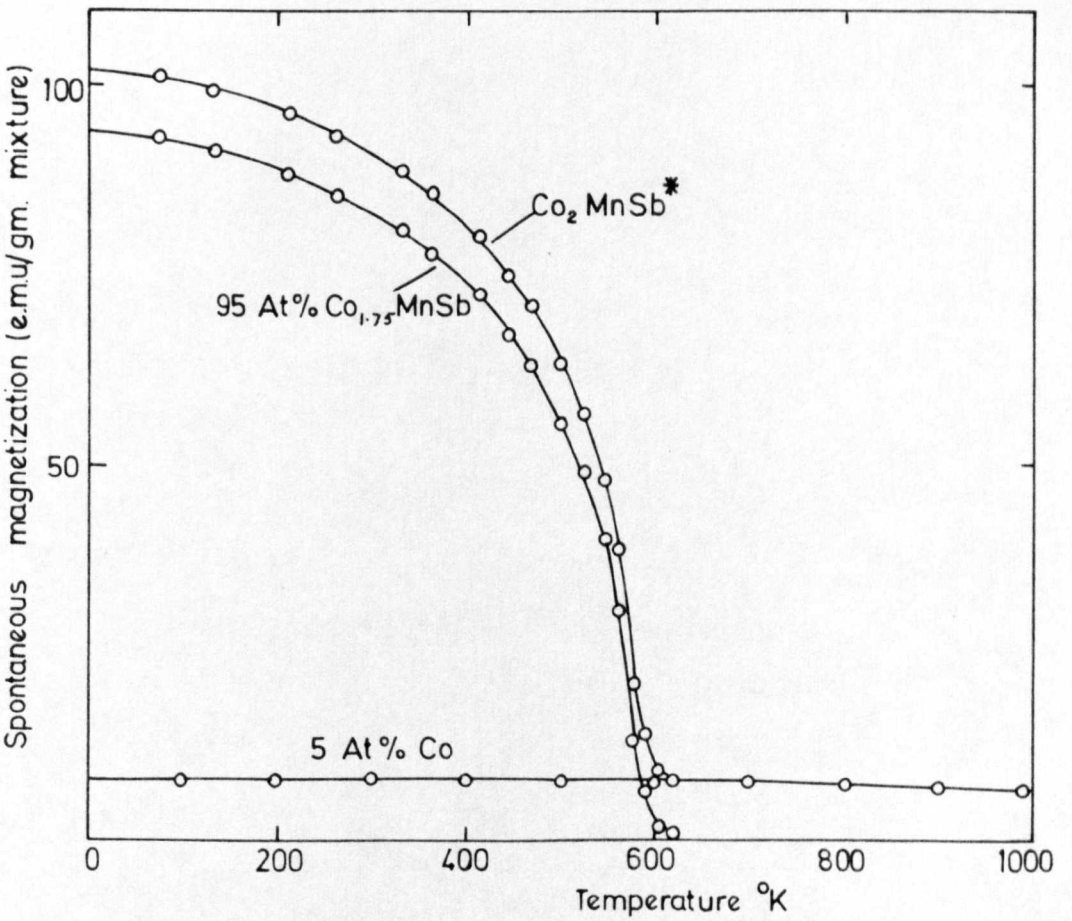

Fig. 7.12 Spontaneous magnetization $\sigma_{o,T}$ versus temperature for the alloy Co_2 Mn Sb*

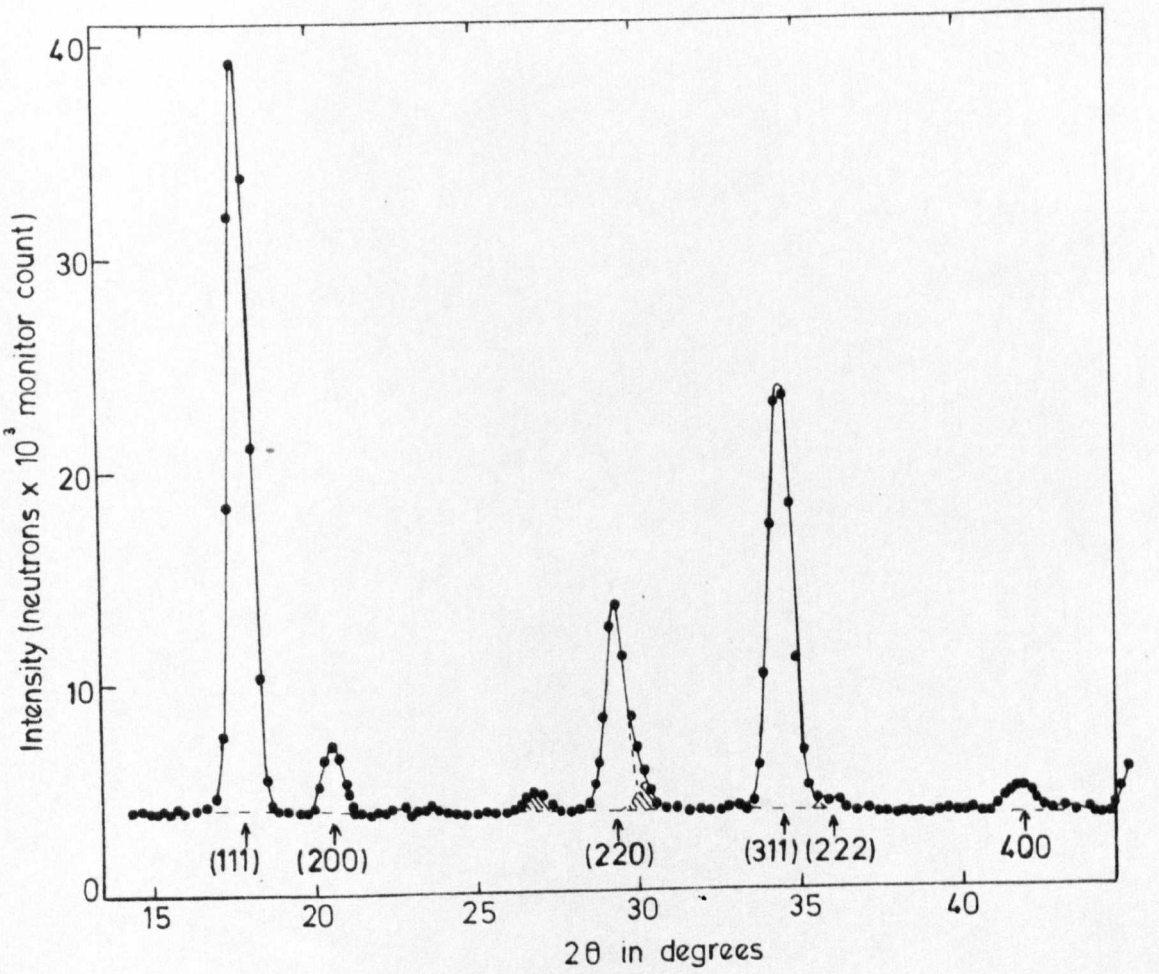

Fig 7.13 Neutron diffraction pattern of Co_2MnSb at 293°K

curve for a 5 At.% admixture of Co, assuming a magnetic moment of 1.716 μ_B per Co atom, and the curve for 95 At.% $Co_{1.75}MnSb$ is the difference between the two. The principal magnetic features are summarized in table (7.17).

TABLE 7.17

Alloy	Θ_F (°K)	σ_{00} (emu/g)	μ_{00} (μ_B)	$\mu_{0,293}$ (μ_B) Co	$\mu_{0,293}$ (μ_B) Mn
Co_2MnSb*	-	101.8 1	-	-	-
$Co_{1.75}MnSb$	600 ± 10	98.7 ± 2	4.90 ± 0.1	0.52 ± 0.1	3.50 ± 0.2
Co	(1388)	(163.9)	(1.716)	(1.716)	-

The neutron diffraction pattern recorded at 293°K is shown in figure (7.13). The measured intensities were corrected for the effects of temperature using a mean atomic weight of 73, and an estimated Debye temperature of 319°K. The diffraction pattern clearly shows the additional lines due to the undissolved Co. The measured and calculated intensities are compared in table (7.18).

Nuclear intensities are shown for the alloys Co_2MnSb and $Co_{1.75}MnSb$, and the measured and calculated total intensities for the latter alloy are compared. The odd superlattice line intensities are approximately 10% greater than calculated, but this may be explained if the proportion of undissolved Co is slightly in excess of 5 At.%.

The distribution of magnetic moments in this alloy is very similar to that of Co_2MnSn, but the Curie temperature is very much lower. This may be due to the reduced proportion of Co in this alloy.

TABLE 7.18

hkl	Calculated intensities			Measured intensities
	Nuclear		$Co_{1.75}MnSb$	
	Co_2MnSb $L2_1$	$Co_{1.75}MnSb$ $L2_1$	$\mu(Co) = 0.52$ $\mu(Mn) = 3.5$	
111	138	149	198	229
200	9.9	6.4	18.6	18
220	45.3	37.3	67.4	(67.4)
311	117	126	131	154
222	4.5	2.9	4.2	4.2
400	11.7	9.7	12.1	11

7.8 CoMnSb

Nowotny and Glatzl (1952) reported that an alloy at the composition CoMnSb had a Cl type structure with a lattice parameter 5.88 kX, but were unable to definitely distinguish between the Mn and Co atoms. The alloy at the stoichiometric composition contained 2 phases.

A 20 g ingot was made at the composition CoMnSb with a loss in weight on melting of 0.5%. The alloy was annealed at 720°C for 48 h, and then quenched. An X-ray photograph was taken, and the measured and calculated results are compared in table (7.19).

The lattice parameters are in good agreement, and the superlattice line intensities were consistent with the Cl_b structures (1) or (2). Several weak additional lines indicated the presence of a small amount of another phase.

TABLE 7.19

Density g/cm^3	a_0 from density	a_0 Measured	$F^2(\theta = 0)$ Calculated (111)	(200)	(220)	Structure Cl_b
			1405	2401	10609	1. CoMn-Sb
7.6	5.9 A	5.870 A	1201	2809	10609	2. CoMnSb-
			2601	1	10609	3. Co-MnSb

The magnetic isothermals for the alloy are shown in figure (7.14), and the resulting spontaneous magnetization curve in figure (7.15). The principal magnetic features are summarized in table (7.20).

TABLE 7.20

θ_F (°K)	σ_{00} (emu/g)	μ_{00} (μ_B)	$\mu_{0,293}$ (μ_B) Co	$\mu_{0,293}$ (μ_B) Mn
471 ± 4	95.8 ± 1	4.04 ± 0.05	0 ± 0.2	3.30 ± 0.2

The neutron diffraction pattern recorded at 293°K is shown in figure (7.16). The additional small peaks due to the second phase are shaded. The extra reflections could not be readily indexed. The measured intensities of the main Cl_b lines were corrected for the effects of temperature using an estimated Debye temperature of 297°K, and a mean atomic weight of 77. The measured and calculated intensities are compared in table (7.21).

It is clear that structure (2) is incorrect. Good agreement is achieved for the Cl_b structure (1), if it is assumed that there is a small amount of random disorder, equivalent to S = 0.98.

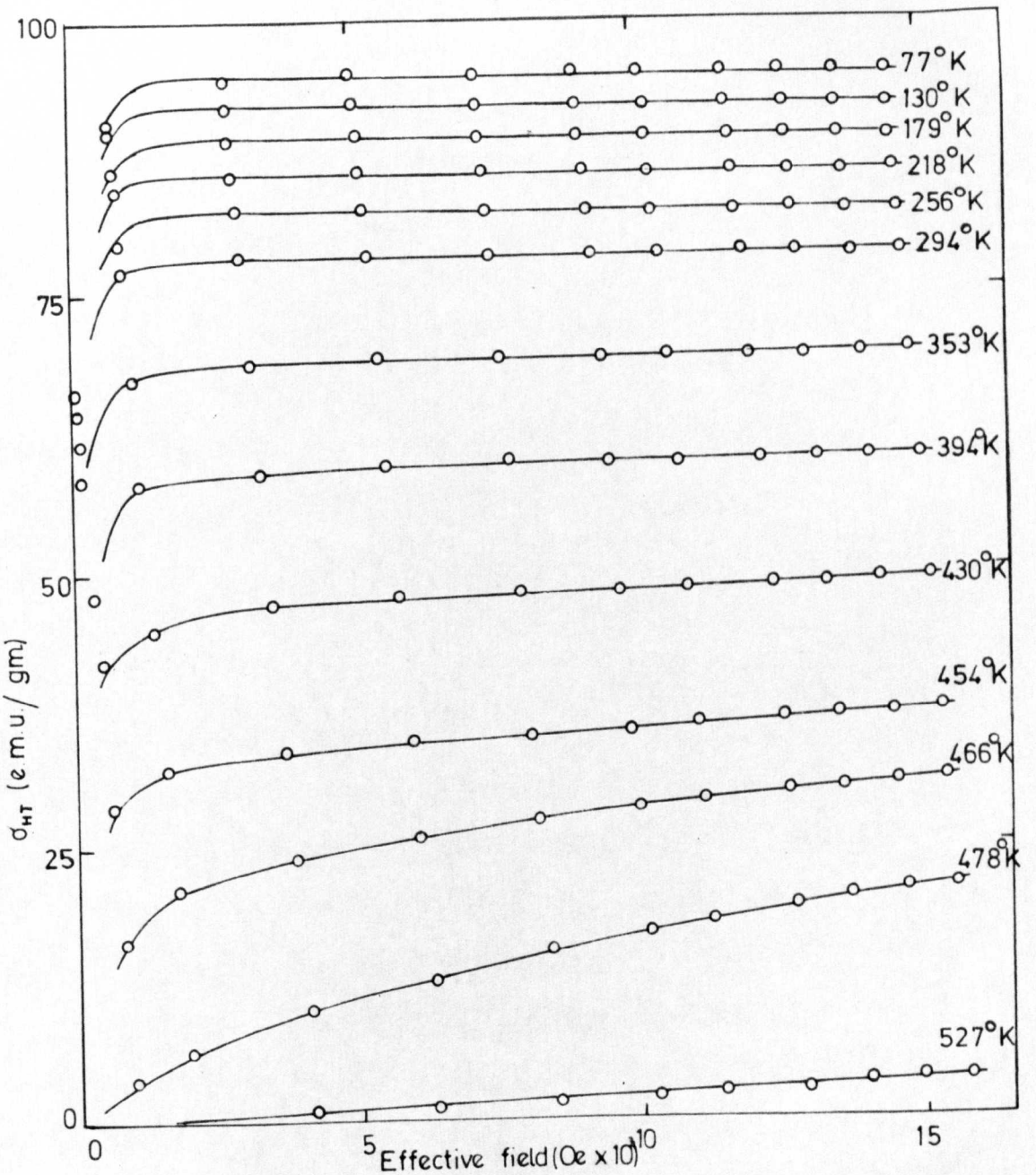

Fig. 7.14. Magnetic Isotherms of CoMnSb

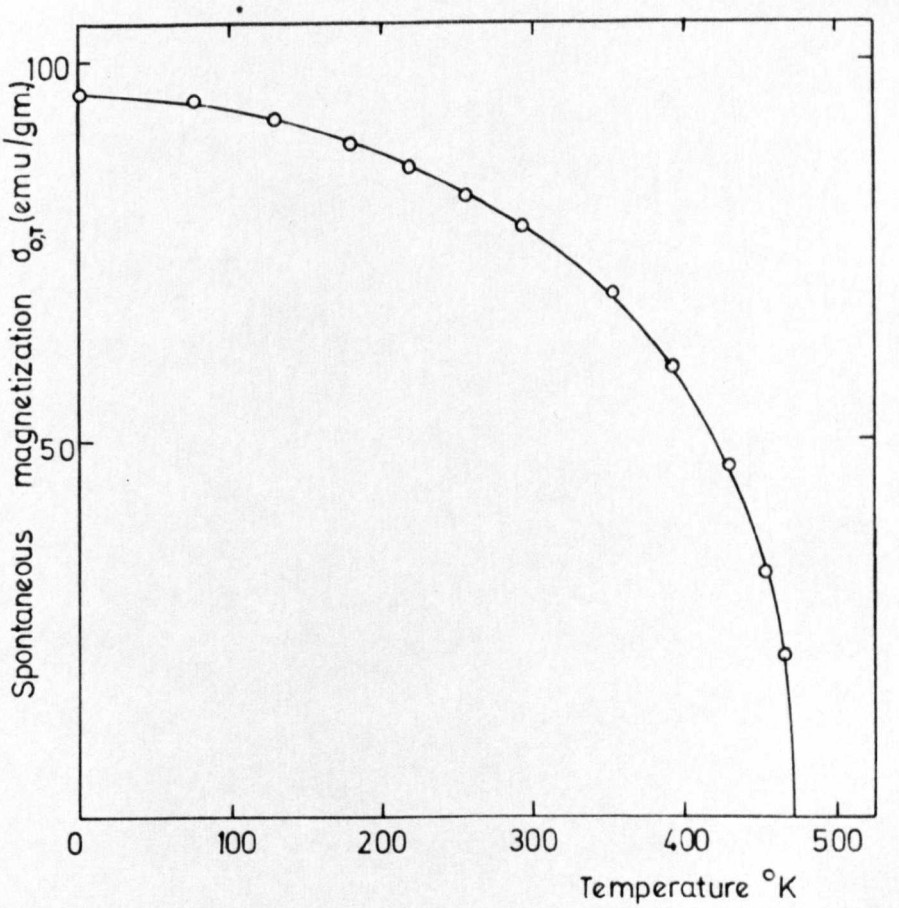

Fig.7.15 Spontaneous magnetization $\sigma_{o,T}$ versus temperature for the alloy CoMnSb.

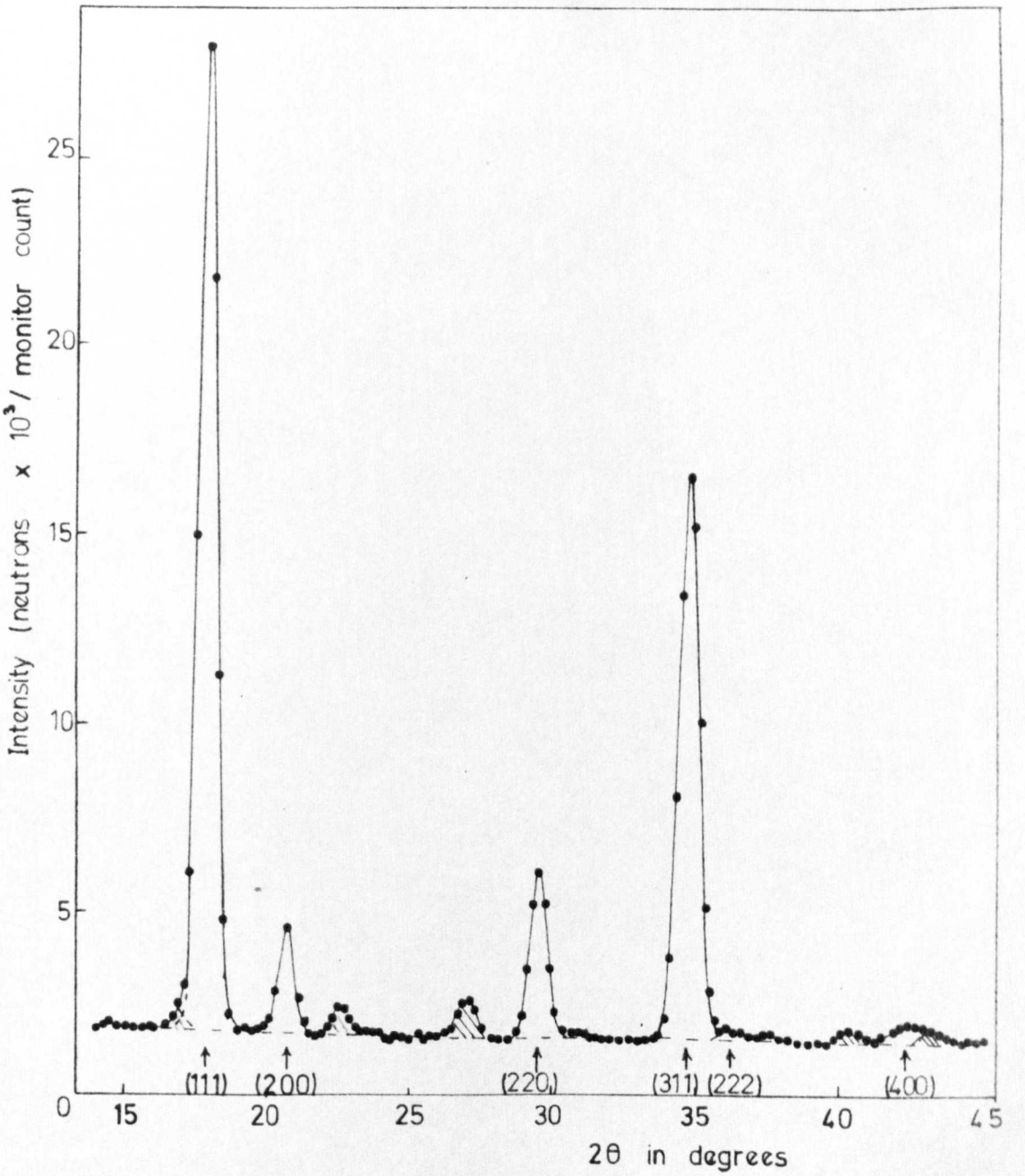

Fig.7.16. Neutron Diffraction pattern of CoMnSb at 293°K

TABLE 7.21

hkl	Calculated intensities			Measured intensities
	Nuclear Cl_b		1. S = 0.98	
	1. CoMn-Sb	2. CoMnSb-	μ(Co) = 0 μ(Mn) = 3.30	
111	146	35.7	187	188
200	0.5	125	23.3	20
220	17.8	17.8	33.9	(33.9)
311	123	30.2	128	128
222	0.2	57.4	3.2	3
400	4.6	4.6	5.7	6

It is of interest to note that this is the only alloy of the series containing cobalt that has no measurable moment on the cobalt atoms. This may be due to the fact that the proportion of Co atoms present is less than that in the cobalt Heusler alloys, and is presumably the reason for the relatively low Curie temperature.

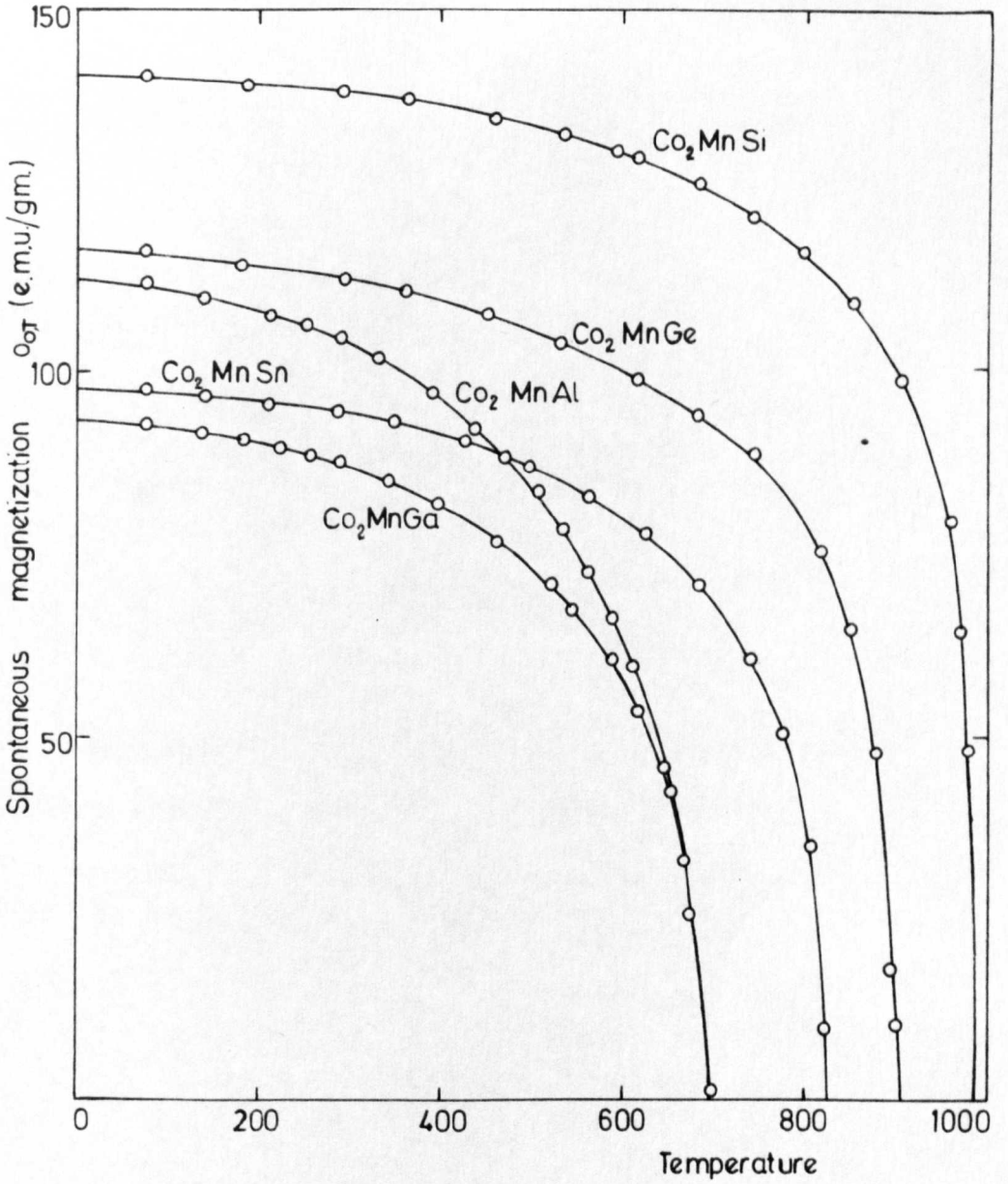

Fig. 7.17 Spontaneous magnetization $\sigma_{o,T}$ versus temperature for the alloys Co_2MnAl, Co_2MnSi, Co_2MnGa, Co_2MnGe, and Co_2MnSn.

CHAPTER 8

Experimental results - Pd_2MnX and PdMnX

8.1 Pd_2MnAl

No references were found to any earlier investigations of alloys in the Pd-Mn-Al system.

A 5 g ingot was made at the composition Pd_2MnAl with a loss in weight on melting of 1.6%. The alloy was annealed at 800°C for 24 h, and then one sample was quenched and the other was allowed to slow-cool over one week. X-ray photographs taken of the 2 samples were indistinguishable, and the results are compared with the calculated results in table (8.1).

TABLE 8.1

Density g/cm^3	a_0 from density	a_0 Measured	$F^2(\theta = 0)$ Calculated (111)	(200)	(220)	Structure
			144	2916	16900	$L2_1$
8.4	6.2 A	6.165 A	1530	144	16900	$F\bar{4}3m$
			0	2916	16900	B2

The lattice parameters are in good agreement, but none of the odd superlattice lines were visible, suggesting either some degree of Mn-Al disorder, or the B2 structure. In addition, one very faint line which could have been the (111) line of Al was just visible.

Susceptibility measurements were made on both slow-cooled and quenched samples, but the results were identical. They are shown in

the form of a reciprocal susceptibility versus temperature curve in figure (8.1). No minimum is observed, but a departure from Curie-Weiss behaviour occurs at 240°K. The principal magnetic features are summarized in table (8.2).

TABLE 8.2

θ_N (°K)	θ_p (°K)	μ_{00} (μ_B) (Neutrons)	μ_{00} (μ_B) ($1/\chi$, T)
240 ± 10	-215 ± 30	4.4 ± 0.2	4.2 ± 0.3

The neutron diffraction patterns obtained at 77°K and 293°K are shown in figure (8.2). The small peak at approximately 26.3° is relatively more intense than the corresponding X-ray line, and is probably due to a small amount of undissolved aluminium. It is clear from the absence of the odd superlattice lines at 293°K that complete Mn-Al disorder exists, and the alloy has the B2 structure. The calculated and measured intensities are compared in table (8.3).

The measured intensities for the (311) and (222) lines are not included as they are seriously overlapped by the (200) line from the copper supporting rod. But, the available information from the (111) and (331) lines is sufficient to show that at 77°K the alloy has an antiferromagnetic structure. If it is assumed that only the Mn atoms have a magnetic moment, and that adjacent Mn atoms along the cube axes are oppositely aligned, then agreement is obtained between measured and calculated intensities for a magnetic moment $\mu_{0,77} = 4.18\ \mu_B$. Extrapolation to 0°K, using a similar Brillouin curve to the ferromagnetic

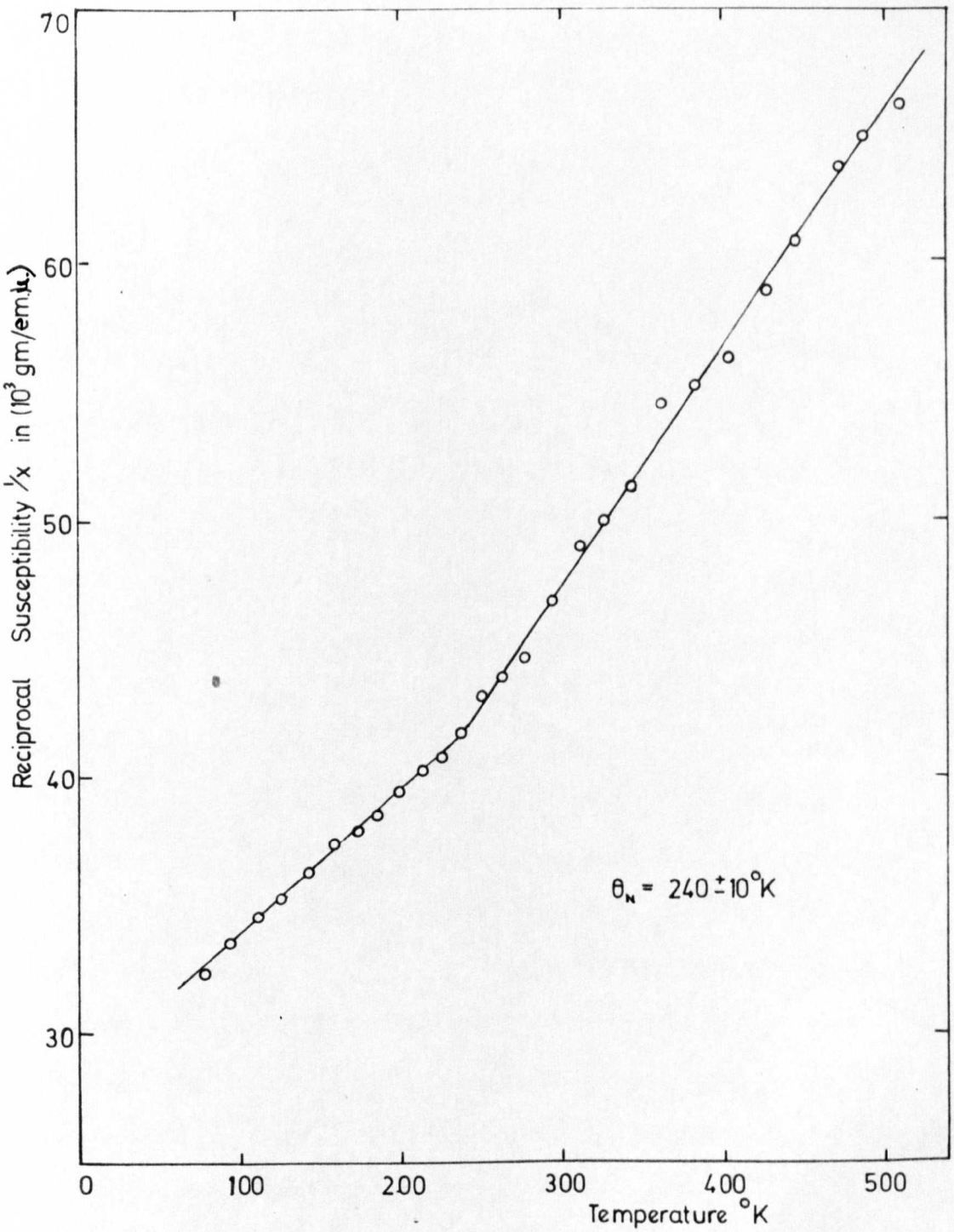

Fig. 8.1. Reciprocal Susceptibility $1/x$ versus Temperature for the Alloy Pd_2 Mn Al.

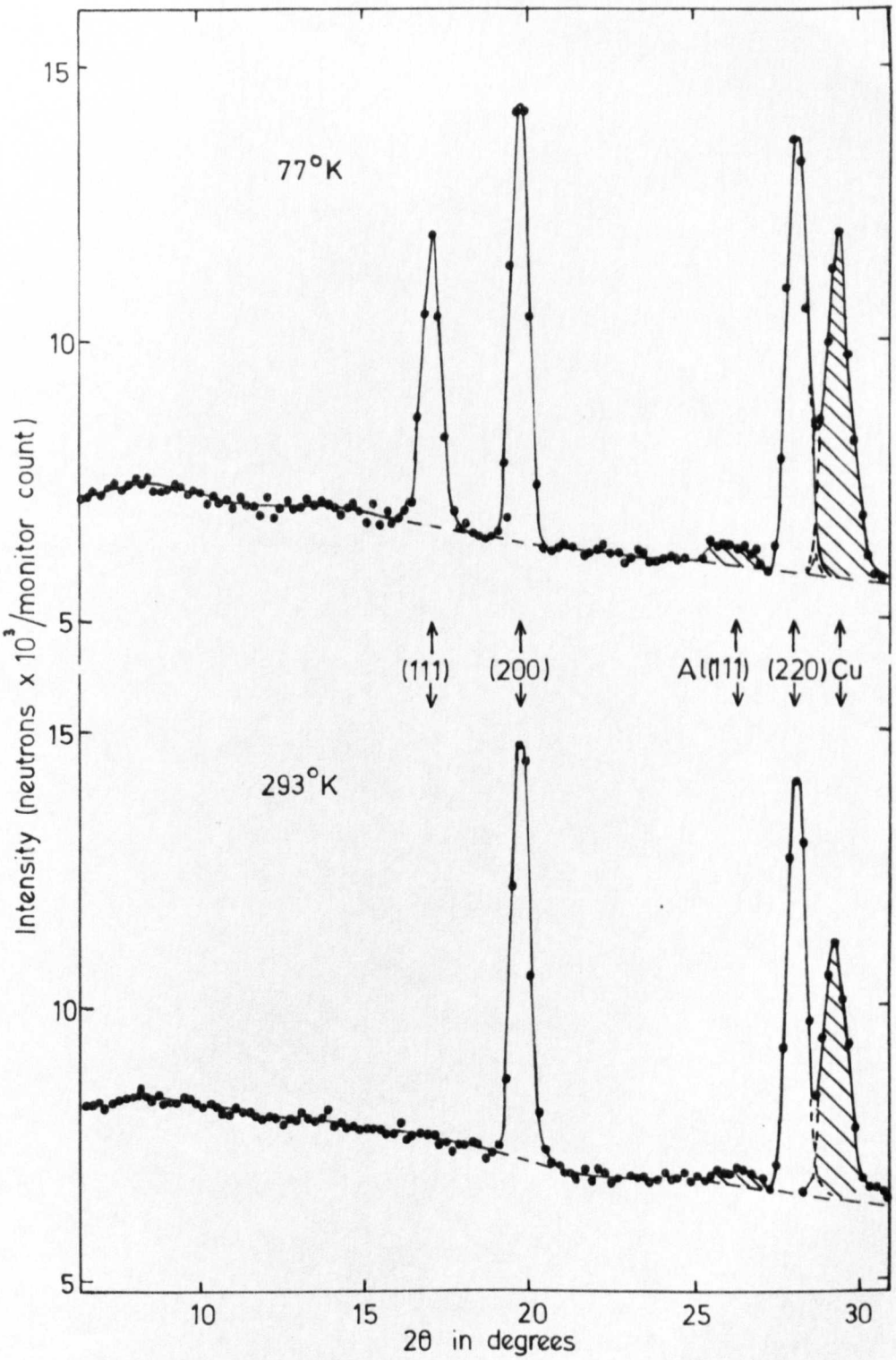

Fig. 8.2. Neutron diffraction pattern of Pd_2MnAl at 293°K and 77°K

Pd Heusler alloys, indicates a magnetic moment at $0^{\circ}K$ $\mu_{00} = 4.4\ \mu_B$.

TABLE 8.3

hkl	Nuclear intensities		Magnetic intensities	
	Calculated B2	Measured (Mean)	Calculated $\mu_{0,77} = 4.18$	Measured
111	0	0	92	92
200	147	139	0	0
220	144	(144)	0	(0)
311	0	-	25	-
222	67	-	0	-
400	37	38	0	0
331	0	0	5	3

Unfortunately, it is not possible from these results to determine the actual moment orientation as the magnetic symmetry is cubic and there is no unique axis.

8.2 $\underline{Pd_2MnSi}$

An alloy was made at the composition Pd_2MnSi, but X-ray photographs indicated a polyphase structure. A small amount of Heusler phase might have been present, but owing to the large number of other lines it was not possible to tell with any certainty.

The alloy was paramagnetic at room temperature, but weakly ferromagnetic at $77^{\circ}K$.

It is possible, but by no means certain that the ferromagnetic properties could be due to a small amount, say 5%, of Heusler phase.

8.3 Pd_2MnGa

No references could be found to any previous investigations of alloys in the ternary Pd-Mn-Ga system.

A 5 g ingot was made at the composition Pd_2MnGa with a loss in weight on melting of 1.9%. After annealing at 800°C for 24 h, one sample was quenched and another was slow-cooled over 36 h. X-ray photographs were taken of both samples, but they were indistinguishable. The calculated and measured results are compared in table (8.4).

TABLE 8.4

Density g/cm^3	a_0 from density	a_0 Measured	$F^2(\theta = 0)$ Calculated (111)	(200)	(220)	Structure
			36	1296	21904	$L2_1$
9.6	6.1 A	6.180 A	410	36	21904	$F\bar{4}3m$
			0	1296	21904	B2

The lattice parameters are in reasonable agreement. The even superlattice lines were of moderate intensity but the odd lines were not visible, suggesting either the B2 structure, or some preferential Mn-Ga disorder.

Susceptibility measurements were made on both quenched and slow-cooled samples with slightly different results. The results are shown in the form of reciprocal susceptibility versus temperature curves in figure (8.3). Both curves are typical of a paramagnetic, or antiferromagnetic, alloy together with a small amount of ferromagnetic impurity. Both alloys exhibited a small field dependency below 205°K, and the

$1/\chi$, T curves have a point of inflection at about 205°K and slightly different gradients in the paramagnetic region. All the above results are consistent with Pd_2MnGa having an antiferromagnetic structure with $\theta_P < -108$°K, together with a small amount of ferromagnetic, or possibly ferrimagnetic, phase with a Curie temperature about 205°K. The slow-cooled alloy has the larger amount of ferromagnetic phase. The principal magnetic features are summarized in table (8.5).

TABLE 8.5

θ_N (°K)	θ_P (°K)	$\mu_{0,77}$ (μ_B) (Neutrons)	μ_{00} (μ_B) (1/χ, T)
$77 < \theta_N < 293$	$\theta_P < -108$	3.7 ± 0.3	$> 4.0 \pm 0.3$

The neutron diffraction patterns obtained at 77°K and 293°K are shown in figure (8.4). The measured and calculated intensities were corrected for the effects of temperature using an estimated Debye temperature of 200°K, and a mean atomic weight of 85. The measured and calculated intensities are compared in table (8.6).

The agreement between measured and calculated intensities is reasonable. It is clear that there is only a slight tendency to order in the $L2_1$ structure. Most of the alloy has the B2 structure with the Mn and Ga atoms randomly ordered on the Mn/Ga sites.

The antiferromagnetic structure of the alloy is similar to that of Pd_2MnAl, with the magnetic moments on the Mn atoms.

There are 2 possible explanations for the ferromagnetic impurity. It may be associated with the small $L2_1$ regions, or with a small amount

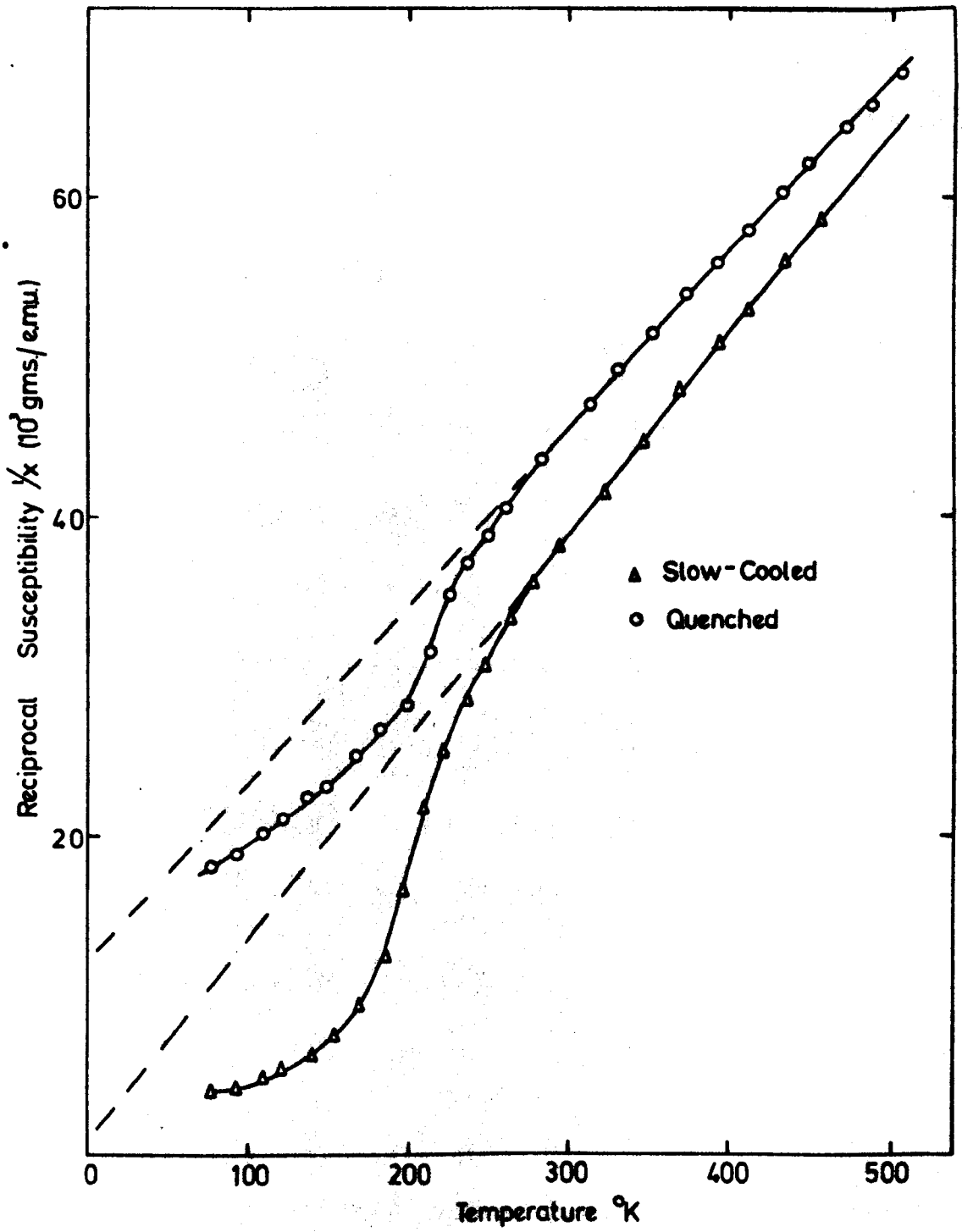

Fig. 8.3. Reciprocal Susceptibility $1/\chi$ versus Temperature for the Alloy Pd_2MnGa when Slow-cooled and Quenched.

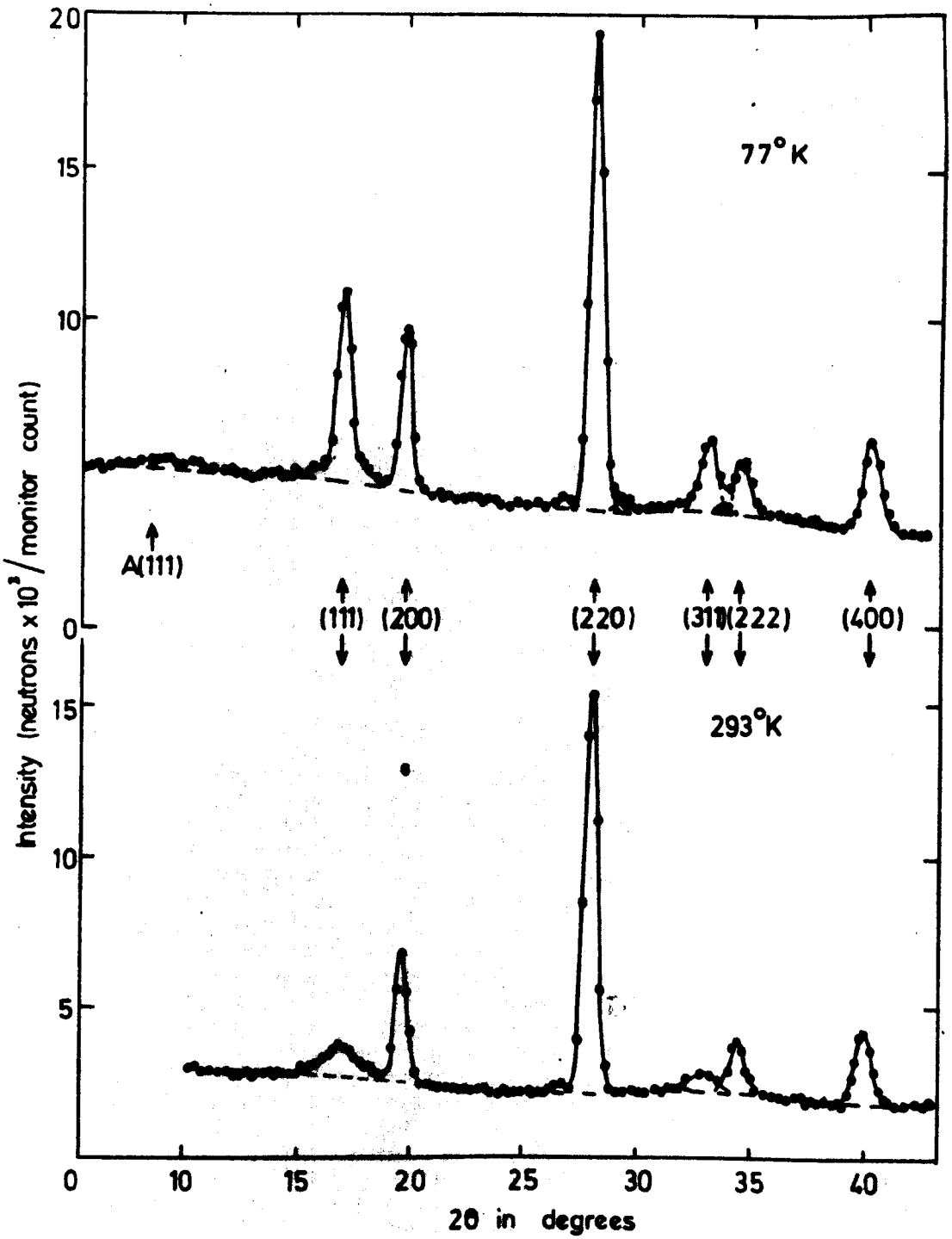

Fig. 8.4. Neutron diffraction pattern of Pd_2MnGa at 293°K and 77°K

of additional phase containing Mn and Ga.

TABLE 8.6

hkl	Nuclear intensities			Magnetic intensities	
	Calculated		Measured	Calculated	Measured
	$L2_1$	α(Mn-Ga) = 0.34	(Mean)	$\mu_{0,77}$ = 3.7	
111	215	38	45	72	73
200	70	70	73	0	0
220	251	251	(251)	0	0
311	182	32	25	20	22
222	33	33	38	0	0
400	65	65	65	0	0

The latter explanation is to be preferred since Tsuboya and Sugihara (1963) have shown that an alloy in the Mn-Ga system is ferrimagnetic with a Curie temperature 470°K. It is not unlikely that a ferromagnetic or ferrimagnetic binary alloy of Mn-Ga, with a Curie temperature of 205°K, could exist at another composition, and the diffraction patterns do show the existence of a small amount of additional phase. In addition, a very diffuse peak is observed at $2\theta \sim 9^\circ$ at 77°K. This peak is almost certainly due to another antiferromagnetic structure existing in the small $L2_1$ regions, similar to that occurring in the $L2_1$ regions of Pd_2MnIn.

8.4 $\underline{Pd_2MnGe}$

No references were found to any earlier investigations of alloys in the Pd-Mn-Ge system.

A 5 g ingot was made at the composition Pd_2MnGe with a loss in weight on melting of 1.2%. After annealing for 24 h at 800°C the alloy was quenched. An X-ray photograph was taken and the measured and calculated results are compared in table (8.7).

TABLE 8.7

Density g/cm^3	a_0 from density	a_0 Measured	$F^2(\theta = 0)$ Calculated (111)	(200)	(220)	Structure
			49	1225	22201	$L2_1$
9.4	6.2 A	6.174 A	637	49	22201	$F\bar{4}3m$
			49	49	22201	DO_3

The lattice parameters are in excellent agreement, and the intensities of the superlattice lines were as expected for the $L2_1$ structure. The even lines were of moderate intensity, but the odd lines were very weak. Several additional very weak lines were also observed on the photograph in addition to the $L2_1$ lines.

The magnetic isothermals are shown in figure (8.5), and the resulting spontaneous magnetization curve in figure (8.15). The principal magnetic features are summarized in table (8.6).

TABLE 8.6

θ_F (°K)	θ_P (°K)	σ_{00} (emu/g)	μ_{00} (μ_B)	μ_{00} (μ_B) (Neutrons)	μ_{00} (μ_B) ($1/\chi$, T)
170 ± 2	180 ± 3	52 ± 2	3.2 ± 0.2	$\sim$ 3.2	3.7

The neutron diffraction patterns obtained at 77°K and 293°K are

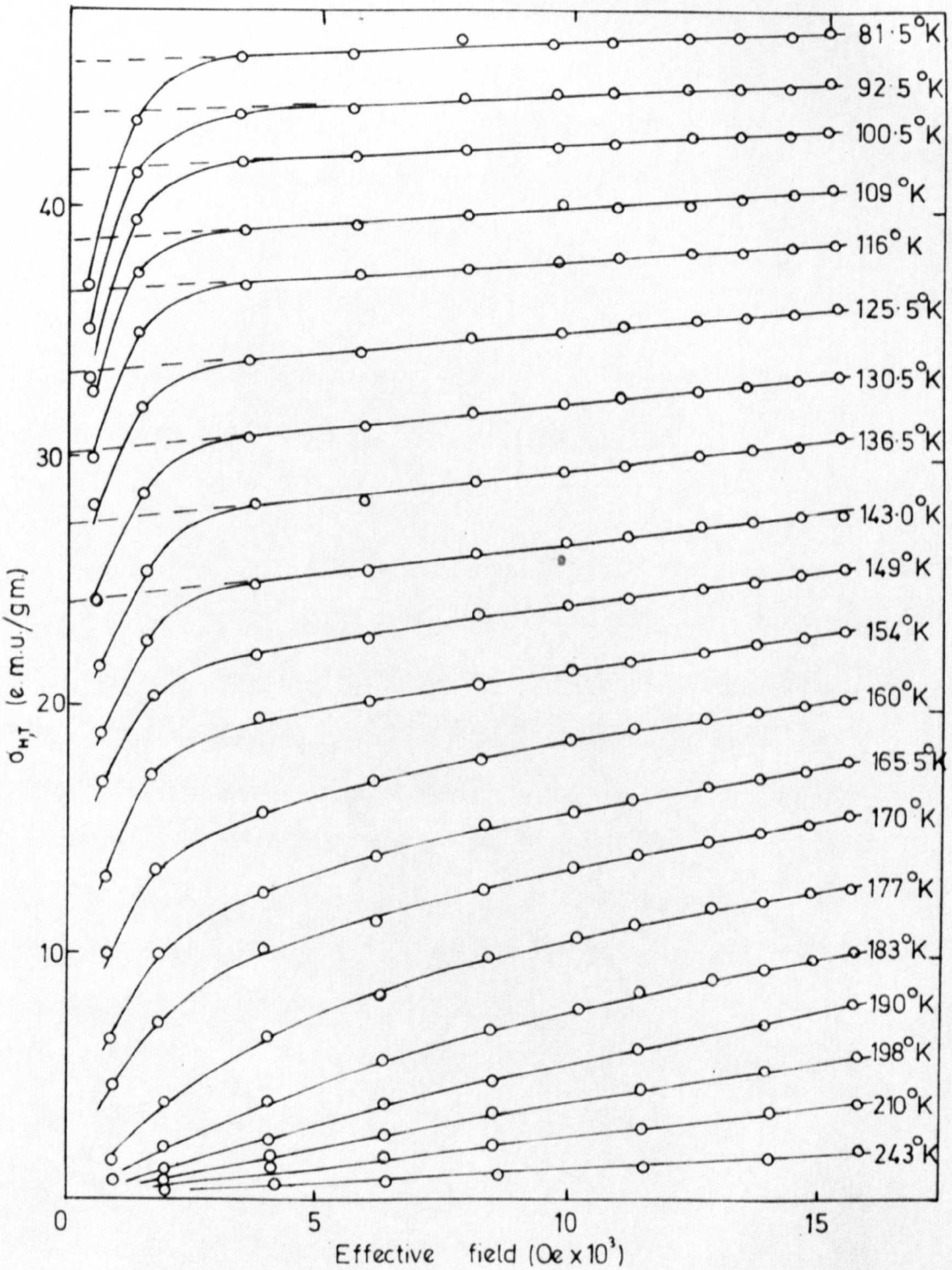

Fig 8.5. Magnetic Isotherms of Pd_2MnGe

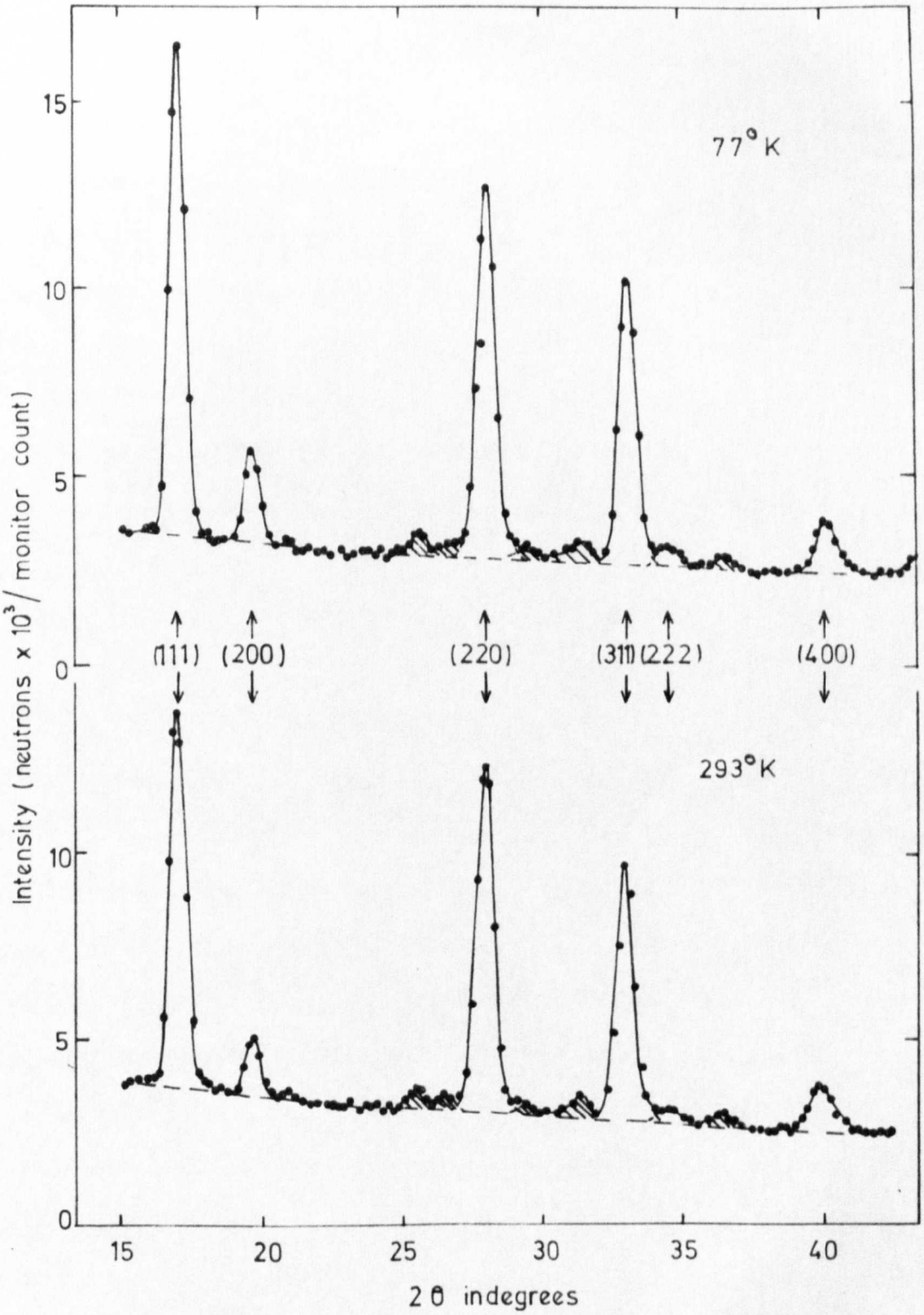

Fig. 8.6. Neutron diffraction pattern of Pd_2MnGe at 293°K and 77°K

shown in figure (8.6). In addition to the $L2_1$ lines there are several extra lines due to a small amount of a second phase. The line intensities were corrected for the effects of temperature using an estimated Debye temperature of 225°K and a mean atomic weight of 86. The measured and calculated results are compared in table (8.7).

TABLE 8.7

	Nuclear intensities		Magnetic intensities	
hkl	Calculated	Measured	Calculated	Measured
	$L2_1$		$\mu_{0,77} = 2.8$	
111	265	274	48	80
200	51	42	21	24
220	291	(291)	12	(12)
311	224	231	11	5
222	23	17	3	2
400	75	58	1	0

The agreement between the measured and calculated nuclear intensities is reasonable, but the measured intensities of the odd lines are slightly greater than is theoretically possible for an alloy at the composition Pd_2MnGe. However, this difference may be explained by a small departure from stoichiometry resulting from the presence of the second phase. The poor agreement between the measured and calculated magnetic intensities of the odd lines is probably due to the experimental error involved in measuring the small difference between 2 relatively large quantities. The results do however suggest that the magnetic

moments are confined to the Mn atoms.

8.5 Pd_2MnIn

No references were found to any earlier investigations of alloys in the Pd-Mn-In system.

A 20 g ingot was made at the composition Pd_2MnIn, with a loss in weight on melting of 1.6%. After annealing at 800°C for 48 h, one sample was quenched and another was slow-cooled over 1 week. An X-ray photograph was taken and the measured and calculated results are compared in table (8.8).

TABLE 8.8

Density g/cm^3	a_0 from density	a_0 Measured	$F^2(\theta = 0)$ Calculated (111)	(200)	(220)	Structure
			576	324	27556	$L2_1$
9.9	6.3 A	6.373 A	338	576	27556	$F\bar{4}3m$
			0	324	27556	B2

The lattice parameters of the 2 samples were identical, but the odd superlattice lines were absent from the photograph of the quenched alloy, and diffuse on the photograph of the slow-cooled alloy.

Quantitative measurements of the line intensities were made using a Philips diffractometer with Cu(Kα) radiation. The measured and calculated intensities are compared in table (8.9).

It is clear that the slow-cooled alloy has the $L2_1$ structure, with some preferential Mn-In disorder. The quenched alloy has a similar structure, but with much more, possibly complete, Mn-In disorder.

TABLE 8.9

hkl	Calculated intensities		Measured intensities	
	$L2_1$	B2	Slow-cooled	Quenched
111	520	0	240	0
200	292	292	290	390
220	16000	16000	(16000)	(16000)

Susceptibility measurements made on both quenched and slow-cooled alloys gave different results. The results are illustrated in figures (8.7a) and (8.7b) in the form of susceptibility and reciprocal susceptibility versus temperature curves. A maximum in the susceptibility occurs for the slow-cooled alloy at 142°K, and the quenched alloy shows a slight departure from Curie-Weiss behaviour over the same temperature range. The principal magnetic features are summarized in table (8.10).

TABLE 8.10

Alloy	θ_N (°K)	θ_P (°K)	μ_{00} (μ_B) (Neutrons)	μ_{00} (μ_B) (1/χ, T)
Slow-cooled	142 ± 3	50 ± 5	4.3 ± 0.2	4.1 ± 0.3
Quenched	$77 < \theta_N < 293$	-50 ± 8	~ 4.3	4.1 ± 0.3

The neutron diffraction patterns obtained at 77°K and 293°K for the 2 alloys are shown in figures (8.8) and (8.9). The room temperature diffraction patterns clearly show the different degrees of Mn-In order. The measured intensities were corrected for the effects of temperature

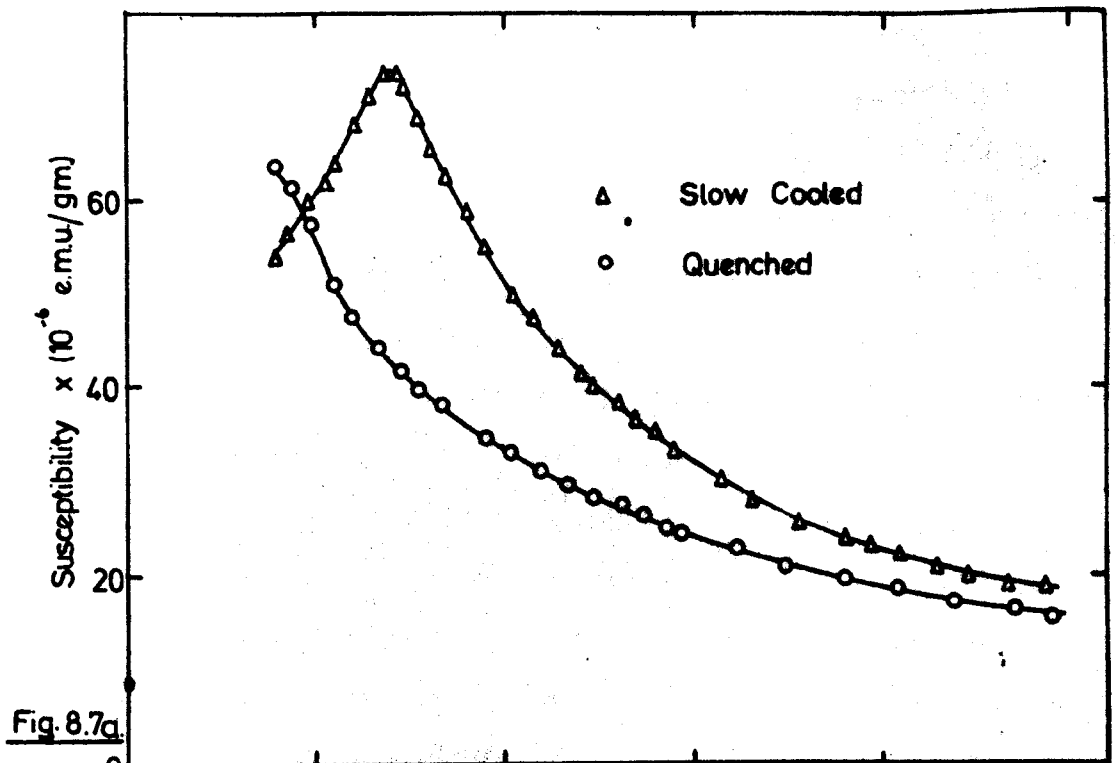

Fig. 8.7a.

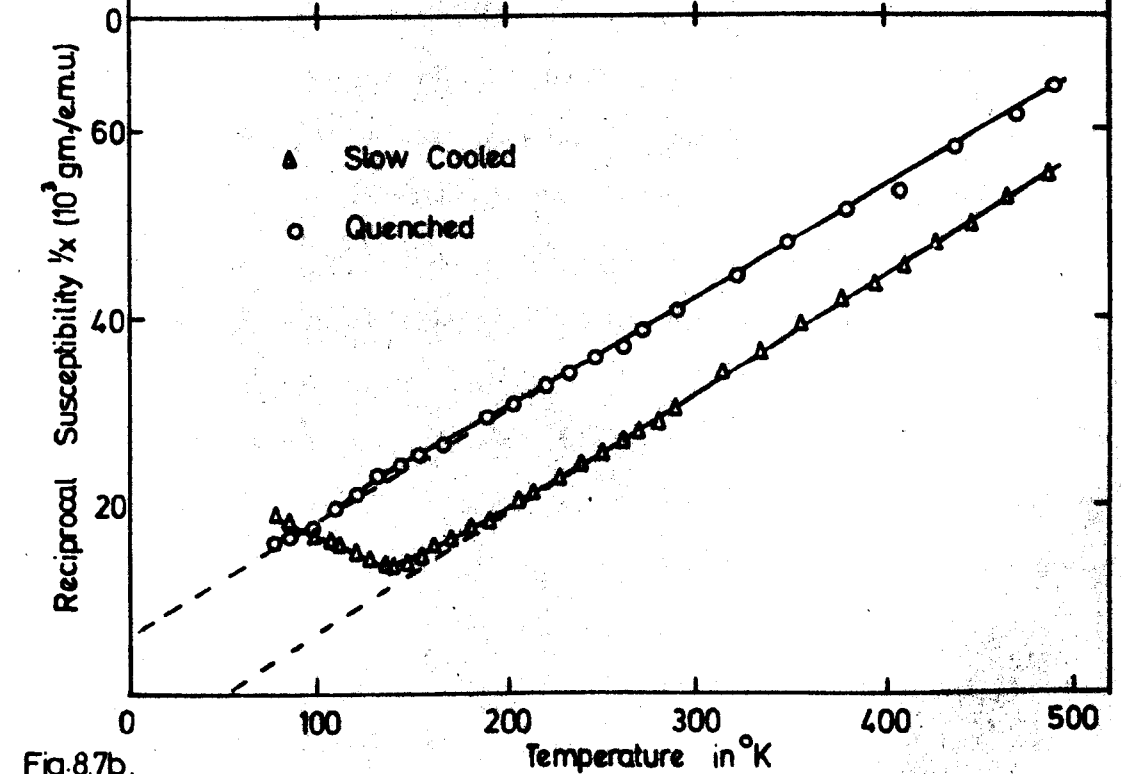

Fig. 8.7b.

a. Susceptibility x, and b. Reciprocal Susceptibility 1/x versus temperature for the alloy Pd_2MnIn when Slow-Cooled and Quenched.

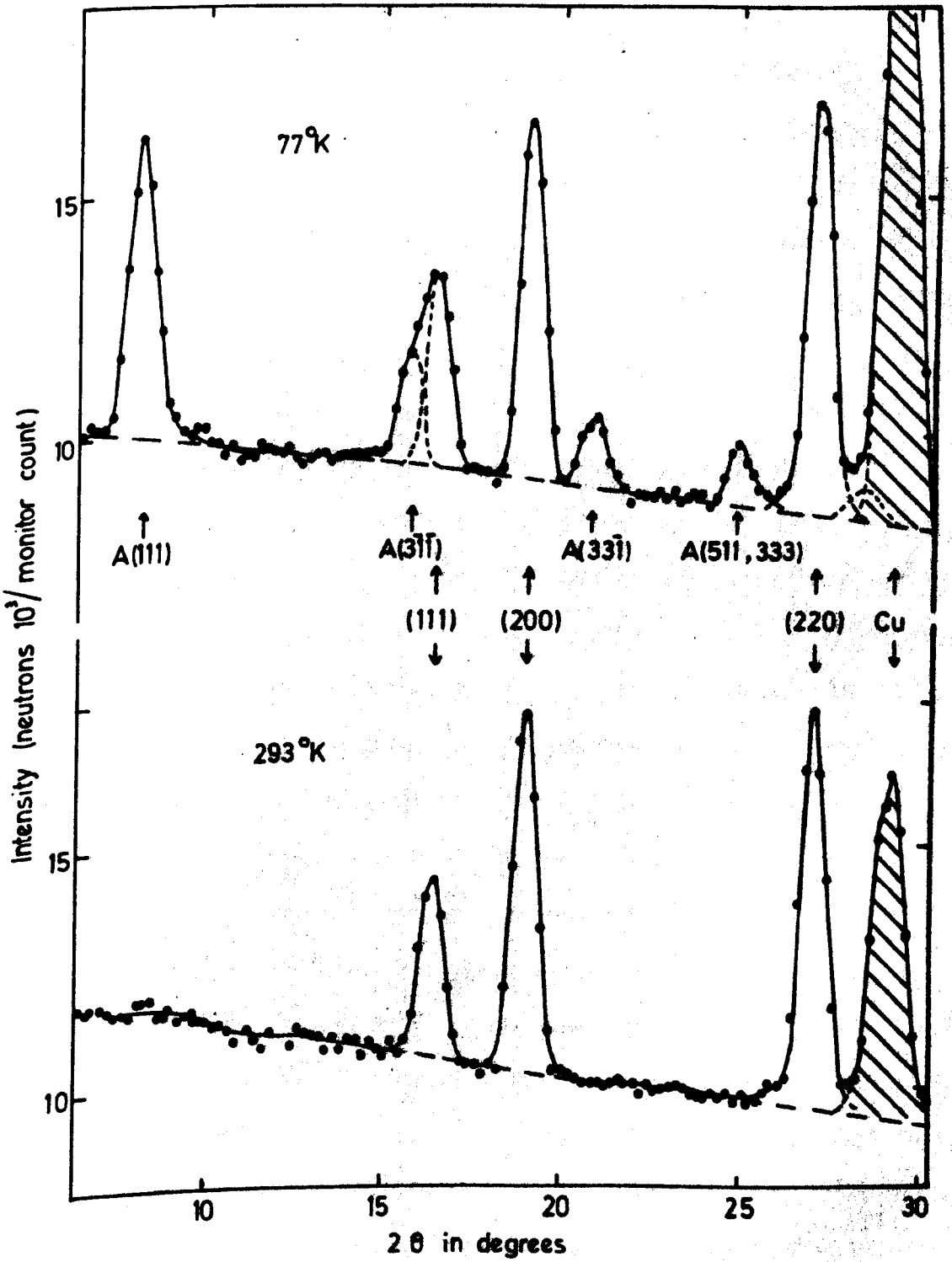

Fig. 8.8. Neutron diffraction pattern of slow cooled Pd_2MnIn at 293°K and 77°K

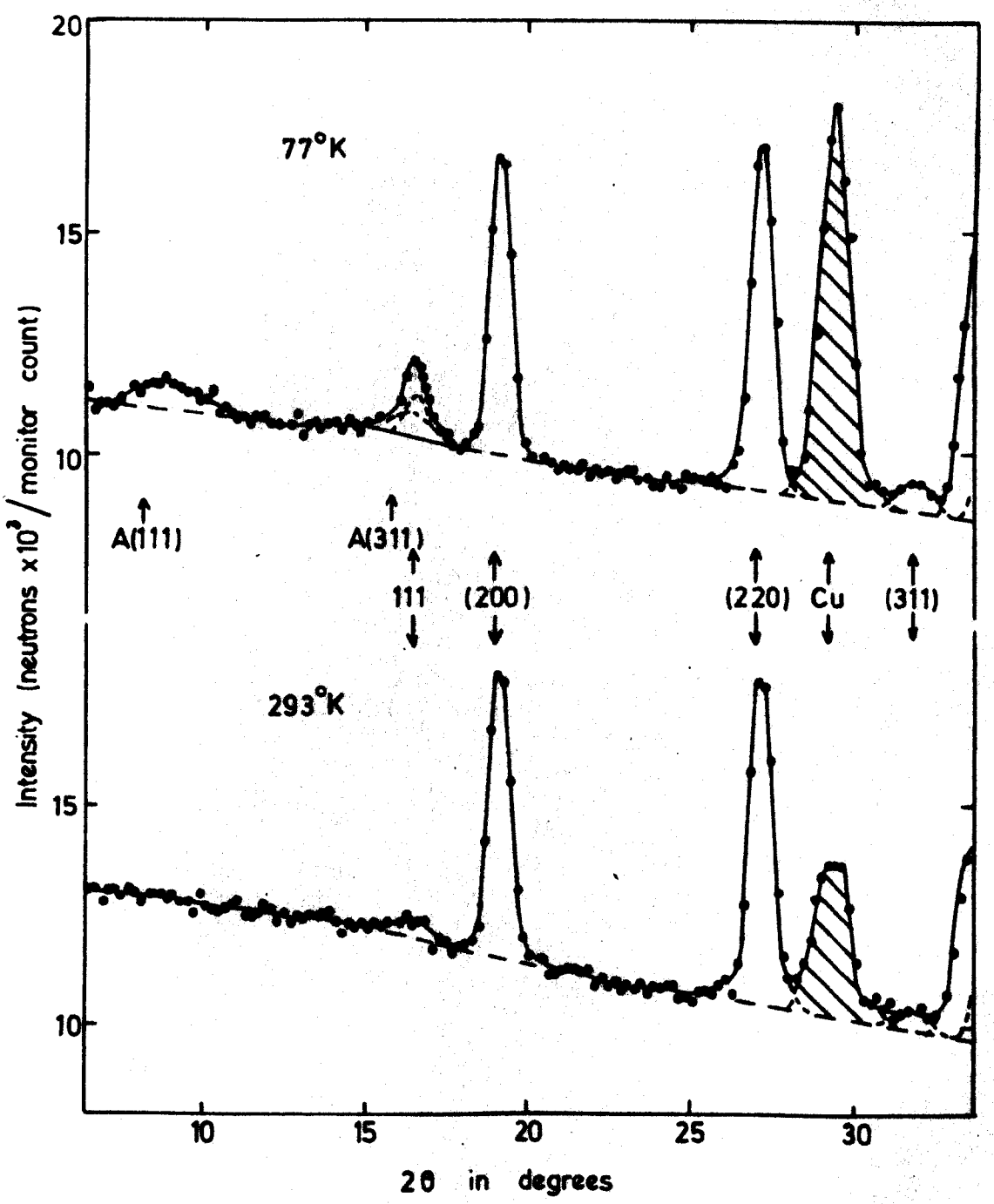

Fig. 8.9. Neutron diffraction patterns of quenched Pd_2MnIn at 293°K and 77°K

using a mean atomic weight of 97, and an estimated Debye temperature of 125°K. The measured and calculated nuclear intensities are compared in table (8.11).

TABLE 8.11

hkl	Nuclear intensities				
	Calculated			Measured	
	$L2_1$	S = 0.97		Slow-cooled	Quenched
		α(Mn-In) = 0.06, α(Mn-In) = 0.29			
111	102	64	15	63	15
200	154	124	124	124	124
220	165	165	165	(165)	(165)
311	91	57	13	62	13
222	75	60	60	-	-
400	42	42	42	42	40

Excellent agreement is obtained between the measured and calculated intensities. It is clear that as anticipated by the X-ray results, the difference between the 2 samples is the extent of Mn-In disorder.

The neutron diffraction patterns at 77°K illustrate the 2 types of antiferromagnetic order that exist.

The additional antiferromagnetic peaks that appear on the diffraction pattern of the slow-cooled alloy at 77°K may be indexed as (111), (311), (331), etc. reflections of a magnetic unit cell with lattice parameter twice that of the chemical ($L2_1$) unit cell, indicating that successive Mn atoms along the cube axes are oppositely aligned. The magnetic

structure model illustrated in figure (8.10) gives satisfactory agreement with the experimental data. The structure is similar to that determined by Shull et al (1951) for MnO. The magnetic lattice consists of parallel (111) planes within which all the Mn atoms are coupled ferromagnetically. Neighbouring (111) planes are coupled antiferromagnetically.

An alternative model was postulated by Li (1955) for MnO, and a similar structure could apply to this alloy. The Li model gives similarly positioned antiferromagnetic lines, but with intensities independent of the direction of moment orientation. The intensities would be equivalent to those of the Shull model with moments aligned along ⟨100⟩ directions.

Since the postulated magnetic symmetry is rhombohedral, the orientation of the spin direction to the unique [111] axis may be determined from the formula derived by Shirane (1959)

$$\langle \cos^2\eta \rangle = \left\{ (n - r) \sin^2\theta + (n + 2r) \cos^2 2\theta \right\} \frac{a^{*2} d^2}{3}$$

where η is the angle between the magnetic and scattering vectors, $n = h^2 + k^2 + l^2$, $r = hk + kl + lh$, a^* is the primitive translation of the reciprocal lattice, and θ is the angle betweem the spin direction and the unique axis.

The values of $\sin\theta$ obtained from several reflections using the above formula are shown in table (8.12) together with the measured and calculated intensities.

It is seen that the moments are aligned at right angles to the unique [111] axis, i.e. in the (111) plane. It is not possible from

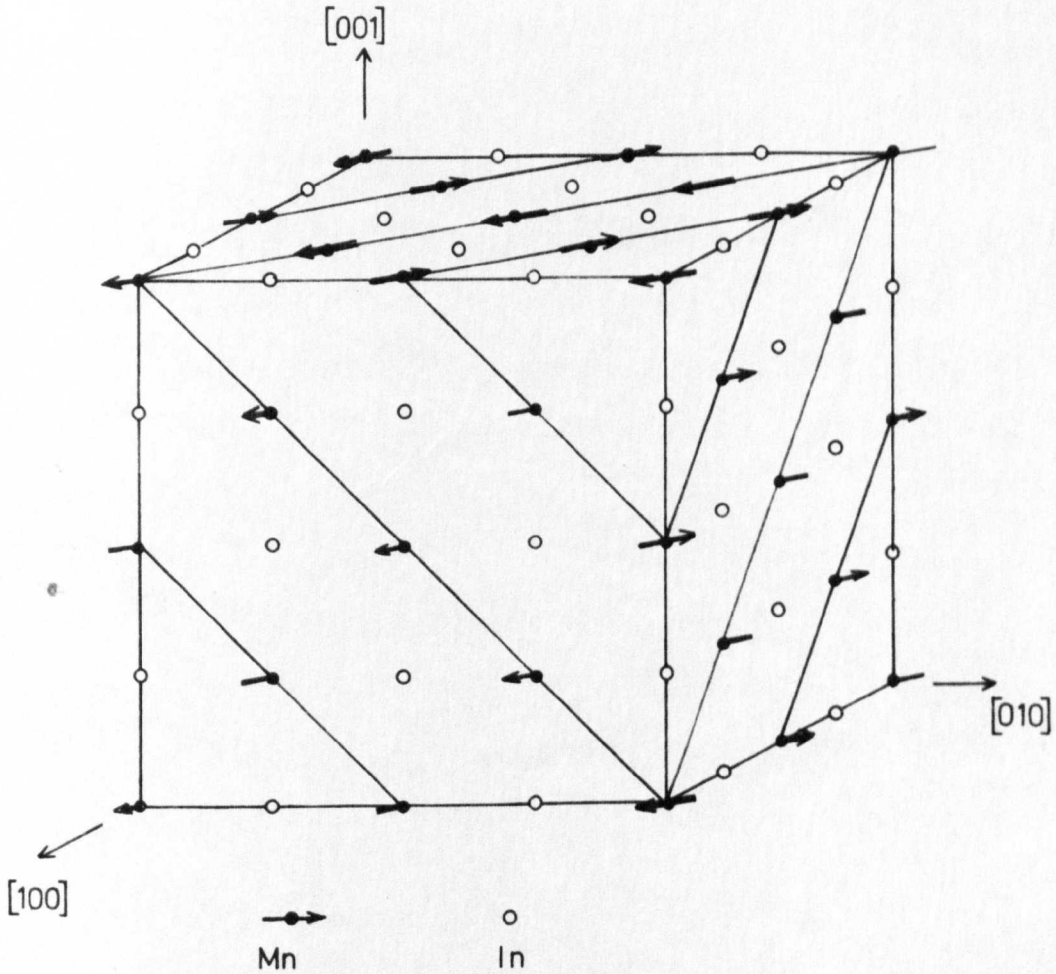

Fig.8.10. Postulated antiferromagnetic structure of ordered Pd_2MnIn. (The Pd atoms have been omitted for clarity.)

these measurements to determine the orientations within the (111) planes, but the most symmetrical arrangement is along $\langle 1\bar{1}0 \rangle$ directions in the (111) plane.

TABLE 8.12

hkl ($a = 2a_0$)	sin θ	Magnetic intensities	
		Calculated	Measured
		$\mu_{0,77} = 3.14$	
111	-	(119)	119
$3\bar{1}\bar{1}$	1.00 ± 0.01	37	37
$33\bar{1}$	0.99 ± 0.01	24	25
511,333	0.99 ± 0.01	23	23

As the moments are not aligned along $\langle 100 \rangle$ directions, the Li model is not a possible alternative.

The magnetic neutron diffraction measurements indicate that the average moment per Mn site at 77°K is 3.14 μ_B, but the nuclear scattering data shows that only 89% of the Mn atoms are on Mn sites. If it is assumed that only the chemically ordered Mn atoms are magnetically ordered, then the magnetic moment per contributing Mn atom is 3.8 μ_B.

The moment per Mn atom at 0°K may be calculated if the relationship between the degree of magnetic order and temperature is known. If it is assumed that the Pd_2MnIn follows a similar ordering curve below its Neel temperature to Pd_2MnSn and Pd_2MnSb below their respective Curie temperatures, then the extrapolated magnetic moment is $\mu_{00} = 4.3\ \mu_B$ per Mn atom.

The neutron diffraction pattern of quenched Pd_2MnIn at 77°K shows diffuse peaks which can be indexed as (111) and $(3\bar{1}\bar{1})$ on the enlarged antiferromagnetic unit cell, but in addition there are increases in intensity at the positions of the (111) and (311) nuclear peaks. These increases may be explained, as in Pd_2MnAl, in terms of an antiferromagnetic unit cell equal in size to the Heusler chemical unit cell. It has been shown that the Mn and In atoms are randomly ordered on the B and D sites over substantial regions of the quenched alloy. In these regions the chemical order is the B2, CsCl type, with one sublattice occupied exclusively by the Pd atoms and the other by Mn and In atoms randomly. If the Mn atoms on adjacent Mn/In sites are antiferromagnetically aligned as in Pd_2MnAl, then additional magnetic peaks would be expected to occur at the (111), (311), etc. positions of the nuclear peaks of the ordered Heusler alloy. In table (8.13) the calculated intensities for the proposed structure, assuming an average moment per Mn site at 77°K of 2.0 μ_B, are compared with the measured values.

TABLE 8.13

hkl	Magnetic intensities	
$(a = a_0)$	Calculated	Measured
	$\mu_{0,77} = 2.0$	
111	(23)	23
311	7	7

If it is assumed that only the regions of B2 type chemical order contribute to this type of antiferromagnetism, then the actual moment

per contributing Mn atom at 77°K is 3.7 μ_B.

No conclusions can be reached concerning the moment orientation in the B2 regions as the magnetic symmetry is cubic, and hence there is no unique axis.

8.6 Pd_2MnSn

No references were found to any earlier investigations of alloys in the Pd-Mn-Sn system.

A 20 g ingot was made at the composition Pd_2MnSn with a loss in weight on melting of 1.2%. After annealing for 48 h at 800°C, one sample was quenched and another was slow-cooled over 36 h, but no differences were observed. The results from the X-ray photographs that were taken are compared with the calculated results in table (8.14).

TABLE 8.14

Density g/cm^3	a_0 from density	a_0 Measured	$F^2(\theta = 0)$ Calculated (111)	(200)	(220)	Structure
			625	289	27889	$L2_1$
9.7	6.4 A	6.380 A	457	625	27889	$F\bar{4}3m$
			121	121	27889	DO_3

The lattice parameters are in excellent agreement, and the superlattice lines were visually of the intensity expected for the $L2_1$ structure. The actual intensities of the first 3 lines, measured using a diffractometer, are compared in table (8.15).

The magnetic isothermals are shown in figure (8.11), and the resulting spontaneous magnetization curve in figure (8.15). The

principal magnetic features are summarized in table (8.16).

TABLE 8.15

hkl	X-ray intensities Cu(Kα)	
	Calculated $L2_1$	Measured
111	571	660
200	259	310
220	16230	(16230)

TABLE 8.16

θ_F (°K)	θ_P (°K)	σ_{00} (emu/g)	μ_{00} (μ_B)	μ_{00} (μ_B) (Neutrons)	μ_{00} (μ_B) (1/χ, T)
189 ± 3	201 ± 3	61.0 ± 1	4.23 ± 0.07	4.23 ± 0.1	3.9 ± 0.3

TABLE 8.17

hkl	Nuclear intensities			Magnetic intensities	
	Calculated		Measured	S = 0.97	Measured
	$L2_1$	S = 0.97		$\mu_{0,77}$ = 4.0	
111	185	174	174	88	93
200	96	90	92	43	38
220	231	231	(231)	27.6	(27.6)
311	156	147	148	25	27
222	44	42	-	7	-
400	59	59	55	2	0

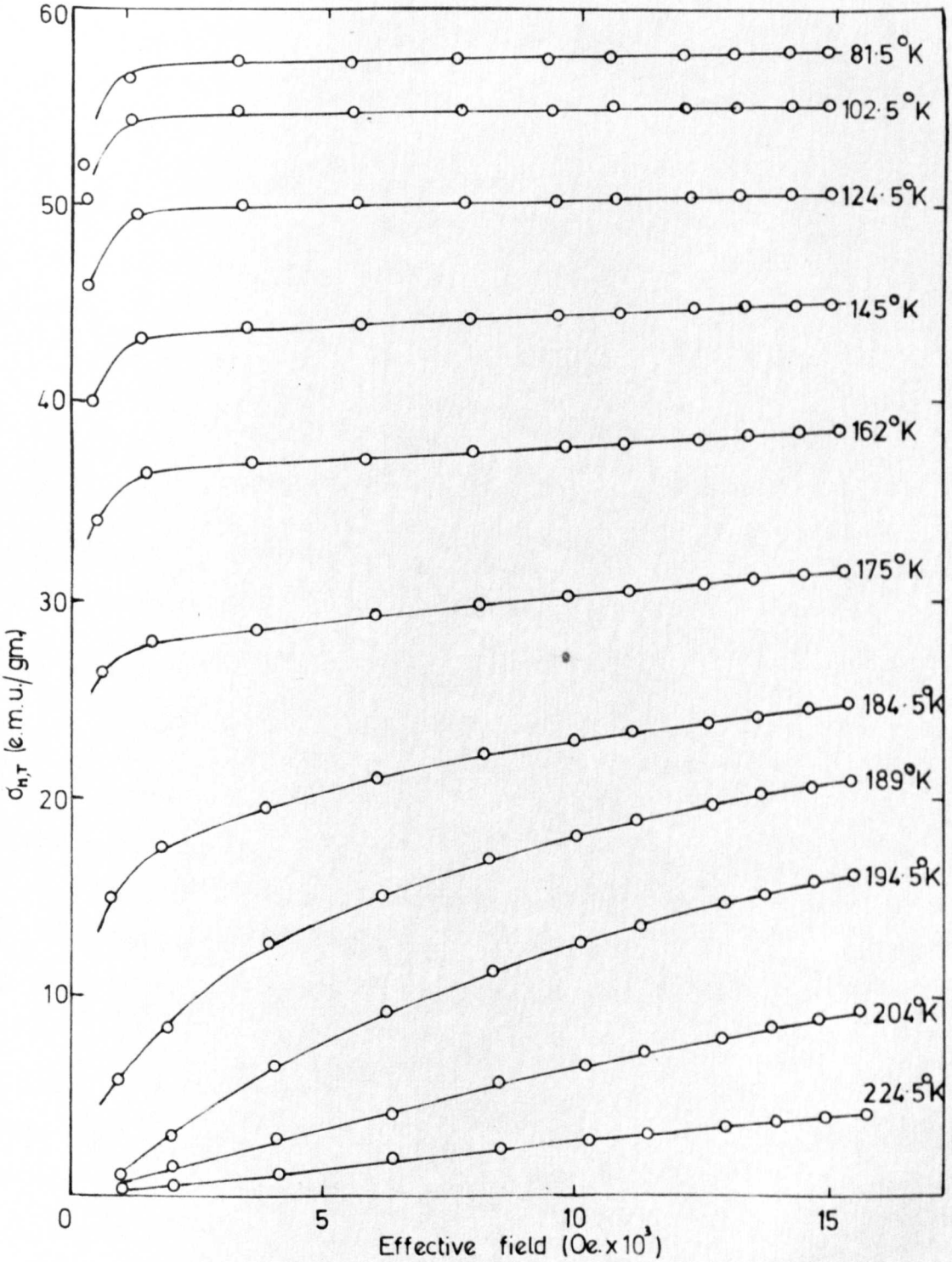

Fig.8.11. Magnetic Isotherms of Pd_2MnSn

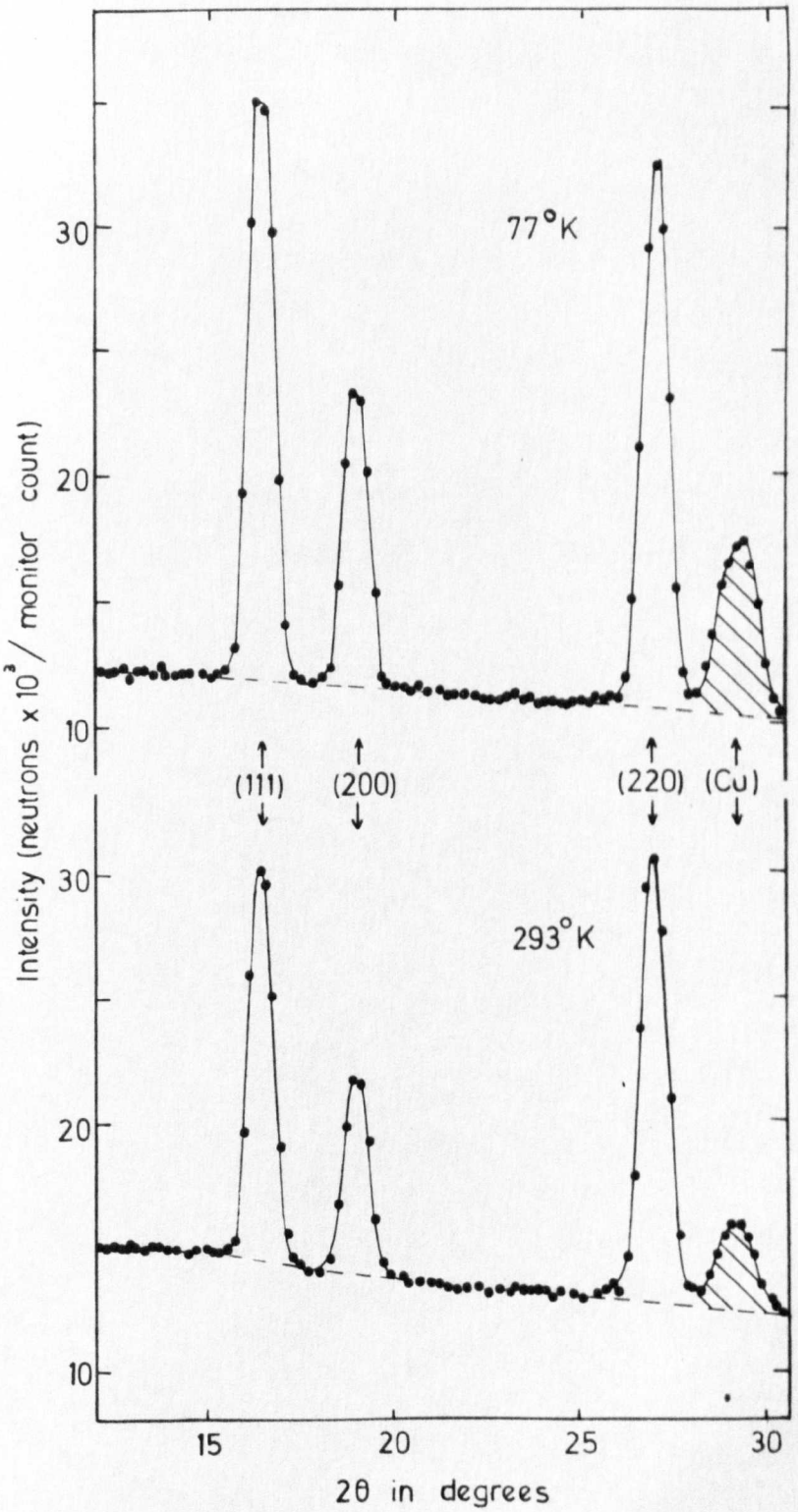

Fig. 8.12 Neutron diffraction pattern of Pd_2MnSn at 293 °K and 77°K

The neutron diffraction patterns obtained at 77°K and 293°K are shown in figure (8.11). The intensities were corrected for the effects of temperature using a Debye temperature of 225°K and an estimated mean atomic weight of 97. The measured and calculated intensities are compared in table (8.17).

The agreement between measured and calculated intensities is good if it is assumed that there is a small amount of random disorder, equivalent to S = 0.97, and that the entire moment resides on the Mn atoms.

8.7 Pd_2MnSb

Hames (1960) reported a new ordered ~~a new ordered~~ alloy at the composition Pd_2MnSb which was very weakly magnetic at room temperature, but due to the weakness of the superlattice lines was unable to determine definitely the detail of the ordered structure.

A 20 g ingot was made at the composition Pd_2MnSb with a loss in weight on melting of 1.5%. The alloy was annealed at 800°C for 48 h, and then one sample was quenched and another was slow-cooled over 36 h, but no differences were observed. The results from the X-ray photographs are compared with the calculated results in table (8.18).

The lattice parameters are in good agreement and the superlattice lines were visually of the intensity expected for the $L2_1$ structure. The actual intensities of the first 3 lines, measured using a diffractometer, are compared in table (8.19).

The magnetic isothermals are shown in figure (8,13) and the resulting spontaneous magnetization curve in figure (8.15). The principal

magnetic features are summarized in table (8.20).

TABLE 8.18

Density g/cm^3	a_0 from density	a_0 Measured	$F^2(\theta = 0)$ Calculated (111)	(200)	(220)	Structure
			676	256	28224	$L2_1$
9.2	6.5 A	6.424 A	466	676	28224	$F\bar{4}3m$
			144	144	28224	DO_3

TABLE 8.19

hkl	X-ray intensities Cu(Kα) Calculated $L2_1$	Measured
111	610	650
200	228	210
220	16480	(16480)

TABLE 8.20

θ_F (°K)	θ_P (°K)	σ_{00} (emu/g)	μ_{00} (μ_B)	μ_{00} (μ_B) (Neutrons)	μ_{00} (μ_B) (1/χ, T)
247 ± 3	259 ± 3	63.0 ± 1	4.40 ± 0.01	4.40 ± 0.1	4.1 ± 0.3

The neutron diffraction patterns obtained at 77°K and 293°K are shown in figure (8.14). The intensities were corrected for the effects of temperature using an estimated Debye temperature of 225°K and a mean atomic weight of 97. The measured and calculated results are compared

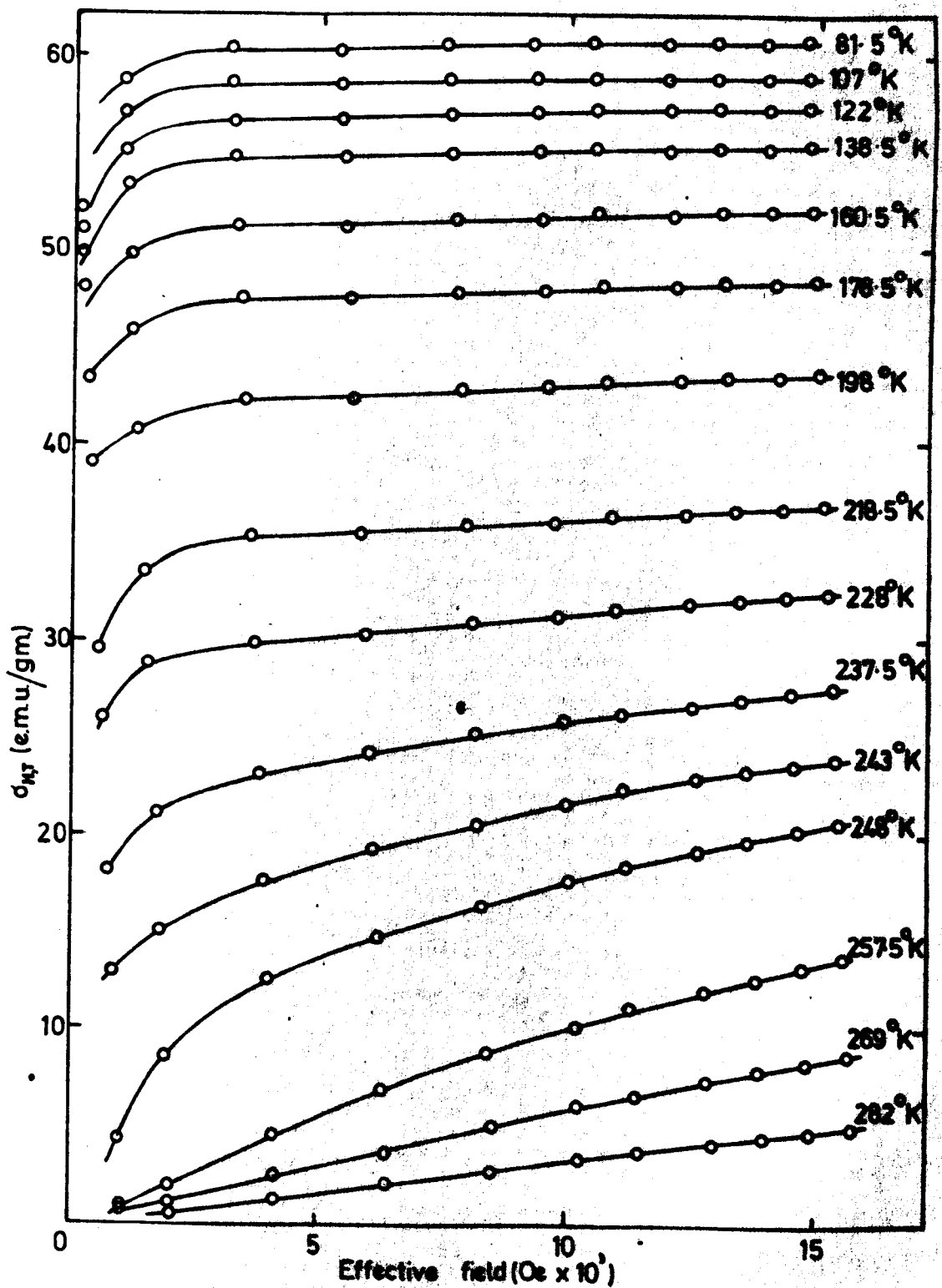

Fig. 8.13. Magnetic Isotherms of Pd_2MnSb

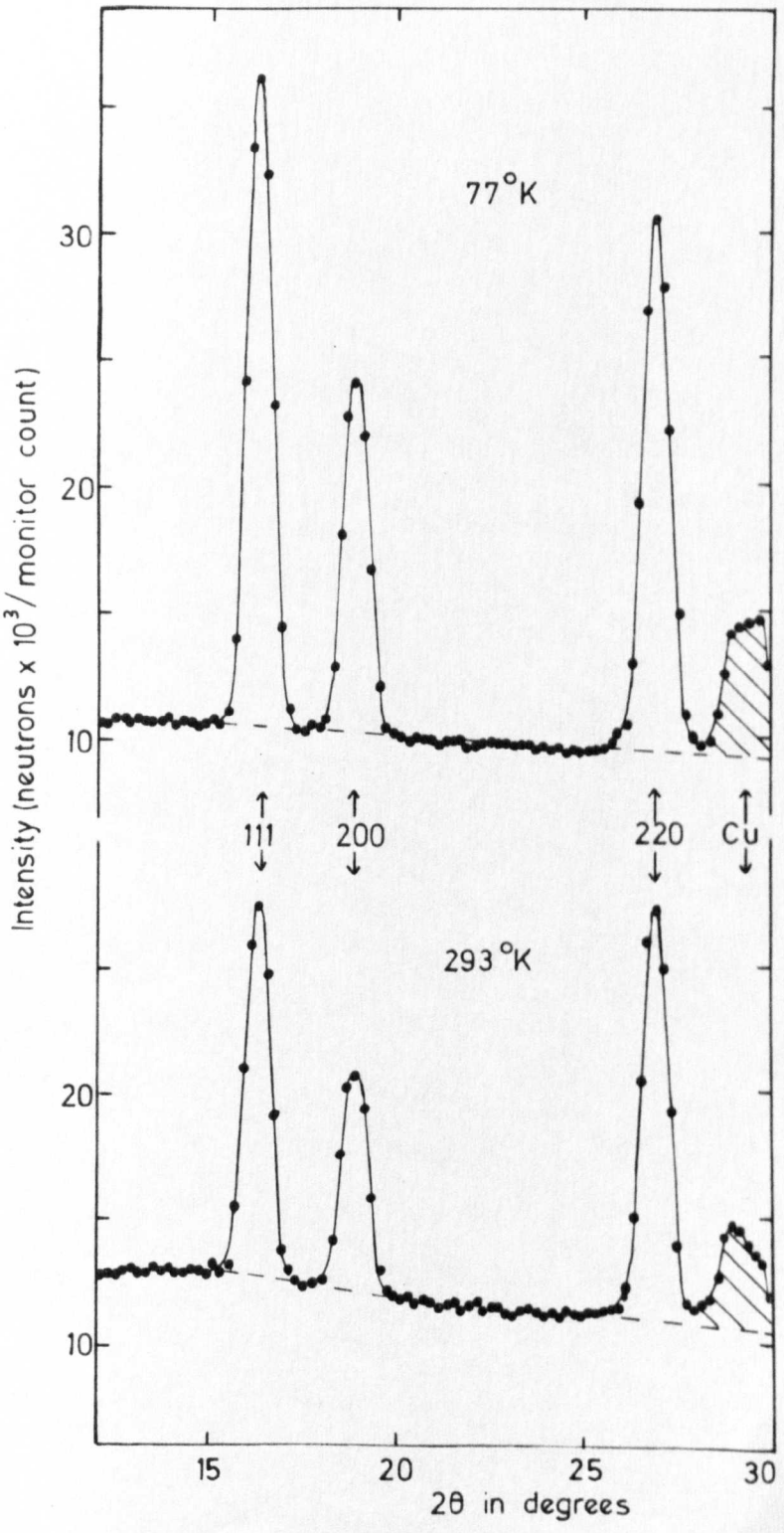

Fig. 8.14. Neutron diffraction patterns of Pd_2MnSb at 293 °K and 77 °K

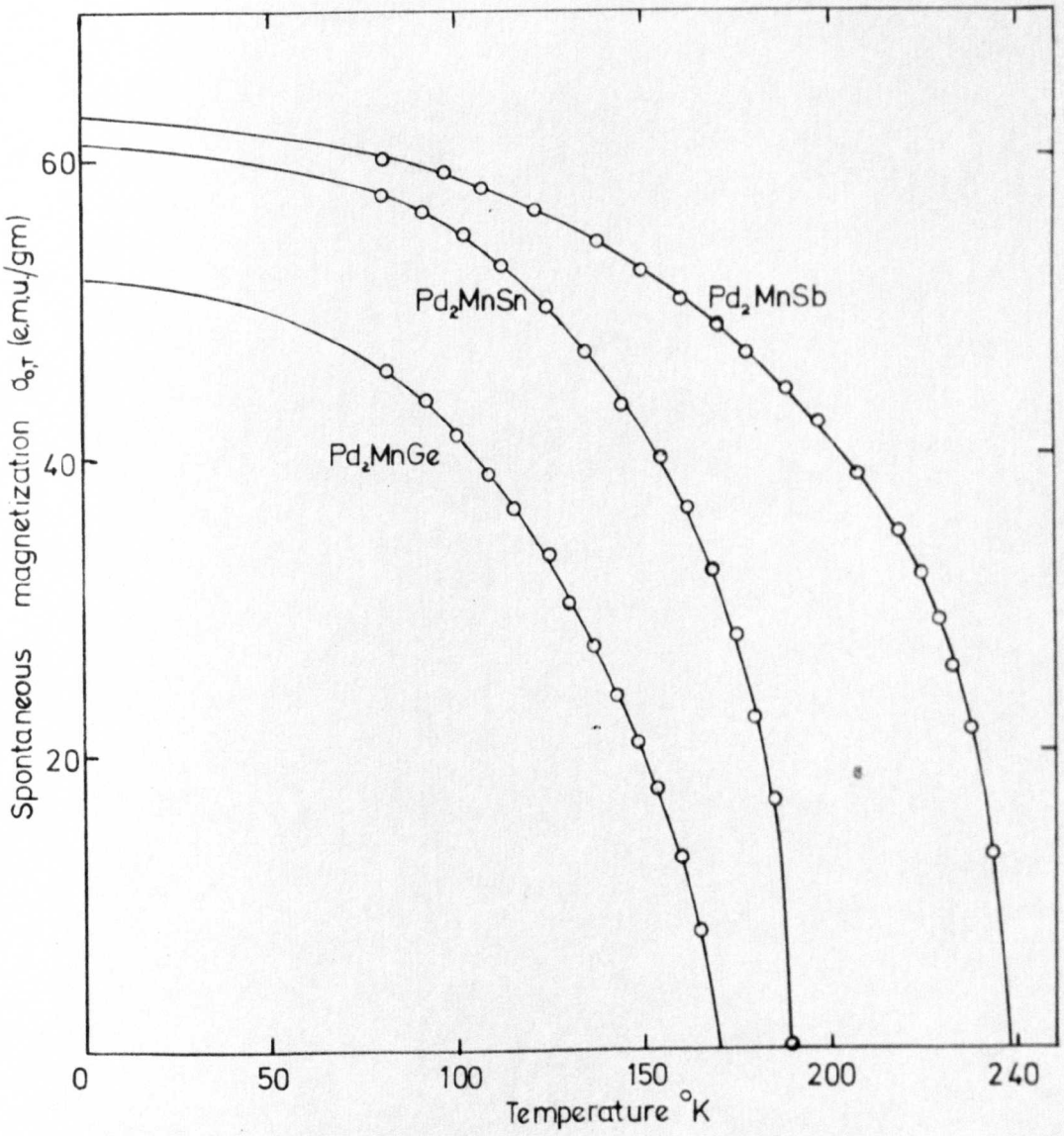

Fig. 8.15. Spontaneous Magnetization $\sigma_{o,T}$ versus Temperature for the Alloys Pd_2MnGe, Pd_2MnSn and Pd_2MnSb.

in table (8.21).

TABLE 8.21

hkl	Nuclear intensities			Magnetic intensities	
	Calculated		Measured	$L2_1$	Measured
	$L2_1$	α(Pd-Sb) = 0.4		$\mu_{0,77}$ = 4.2	
111	162	163	163	105	108
200	113	102	101	52	51
220	211	211	(211)	31	(31)
311	136	137	137	31	29
222	52	47	-	8	-
400	54	54	44	3	7

Good agreement is obtained between measured and calculated nuclear intensities if it is assumed that some preferential Pd-Sb disorder exists. However, it should be noted that slight departures from stoichiometry can give the same result. The magnetic intensities show good agreement if it is assumed that the entire moment resides on the Mn atoms.

8.8 PdMnSb

Hames (1960) reported that an alloy at the composition PdMnSb had the Cl_b structure and was ferromagnetic at room temperature.

A 20 g ingot was made at the composition PdMnSb with a loss in weight on melting of 1.8%. After annealing at 650°C for 48 h, one sample was quenched and the other was slow-cooled over 36 h, but no differences were observed. The results from the X-ray photographs are compared

with the calculated results in table (8.22).

TABLE 8.22

Density g/cm^3	a_0 from density	a_0 Measured	$F^2(\theta = 0)$ Calculated (111)	(200))	(220)	Structure Cl_b
			2792	900	14884	1. PdMn-Sb
7.9	6.2 A	6.233 A	650	5184	14884	2. PdMnSb-
			3042	400	14884	3. Pd-MnSb

The lattice parameters are in good agreement. The odd superlattice lines were of moderate intensity but the even lines were very much weaker, indicating the Cl_b structure (1) or (3). In addition, several weak lines, which could not be satisfactorily indexed, were also observed.

The magnetic isothermals for the alloy are shown in figure (8.16) and the resulting spontaneous magnetization curve in figure (8.17). The principal magnetic features are summarized in table (8.23).

TABLE 8.23

θ_F (^oK)	σ_{00} (emu/g)	μ_{00} (μ_B)
523 ± 4	80.0 ± 1	4.06 ± 0.05

As the alloy had a relatively high Curie temperature, a neutron diffraction pattern was only obtained at 293°K. The diffraction pattern is shown in figure (8.18). As with the X-ray photograph several additional weak reflections are present. The measured intensities were corrected for the effects of temperature using a mean atomic weight of

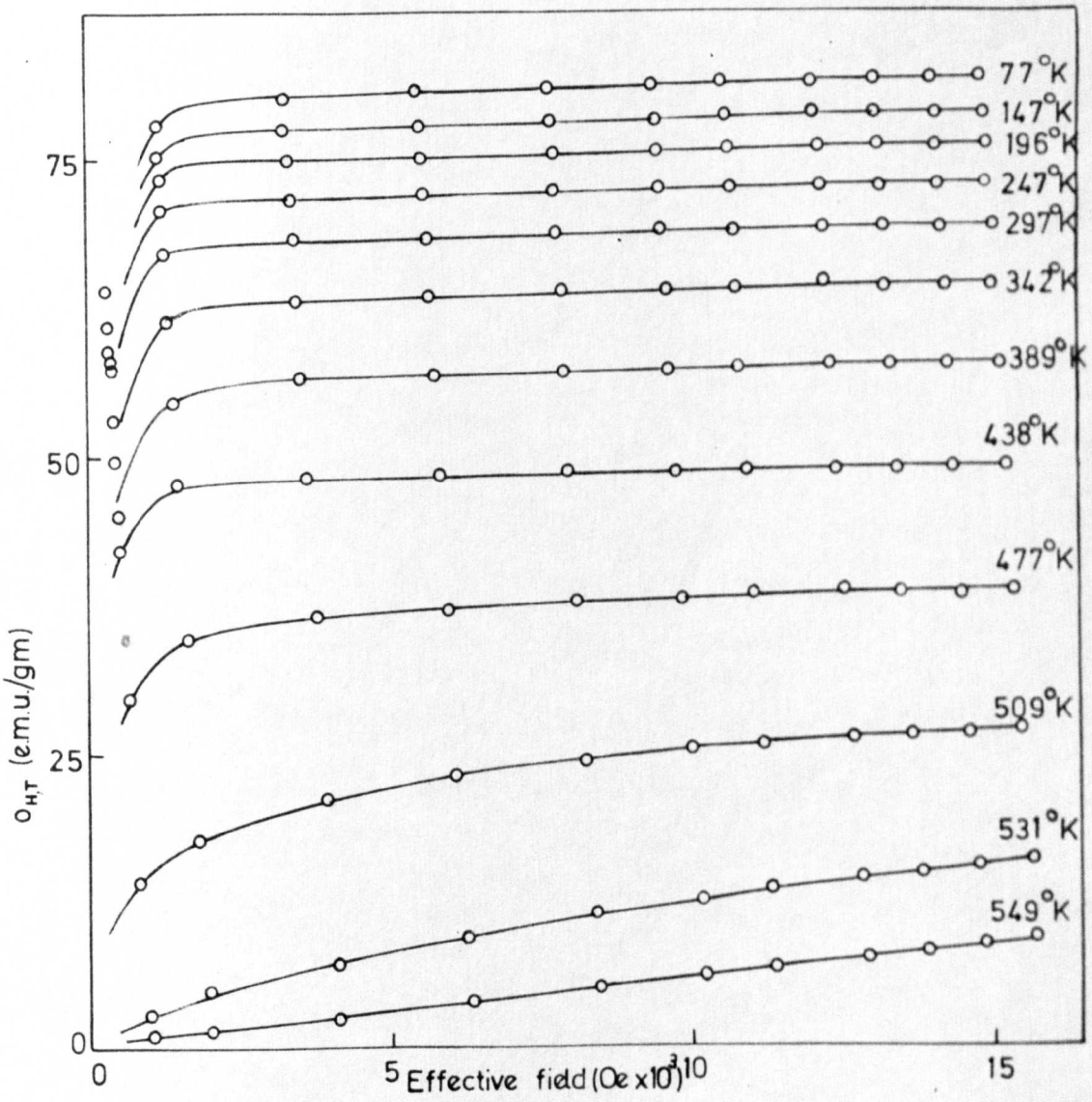

Fig. 8.16. Magnetic Isotherms of PdMnSb

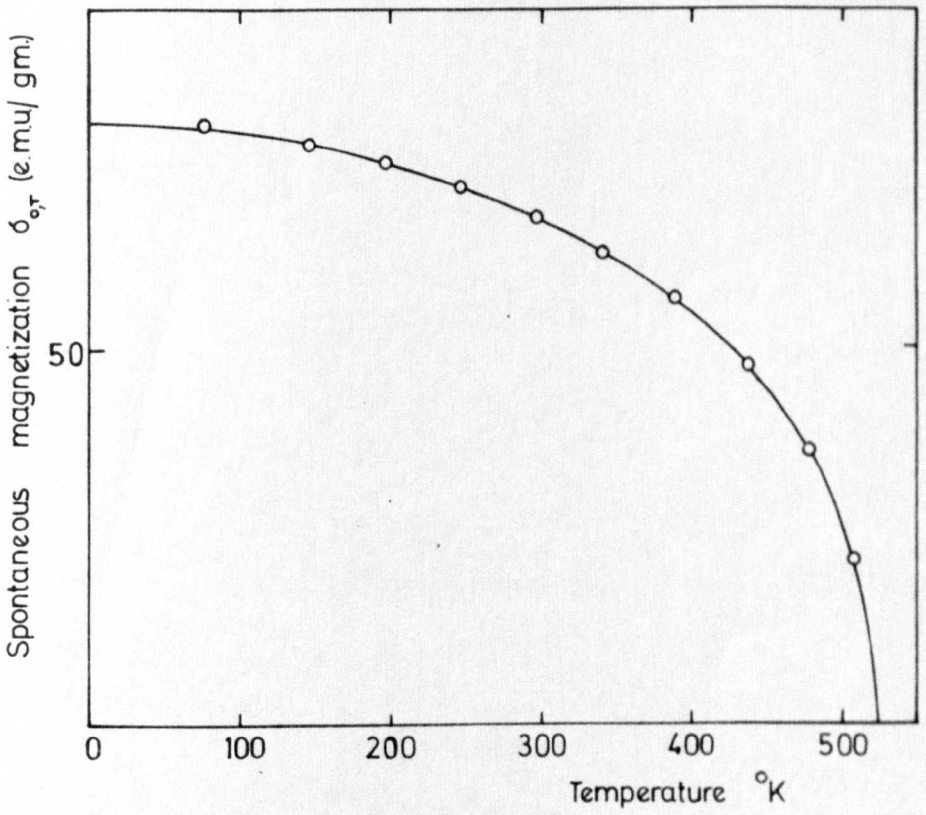

Fig. 8.17. Spontaneous magnetization $\sigma_{o,T}$ versus temperature for the alloy Pd Mn Sb

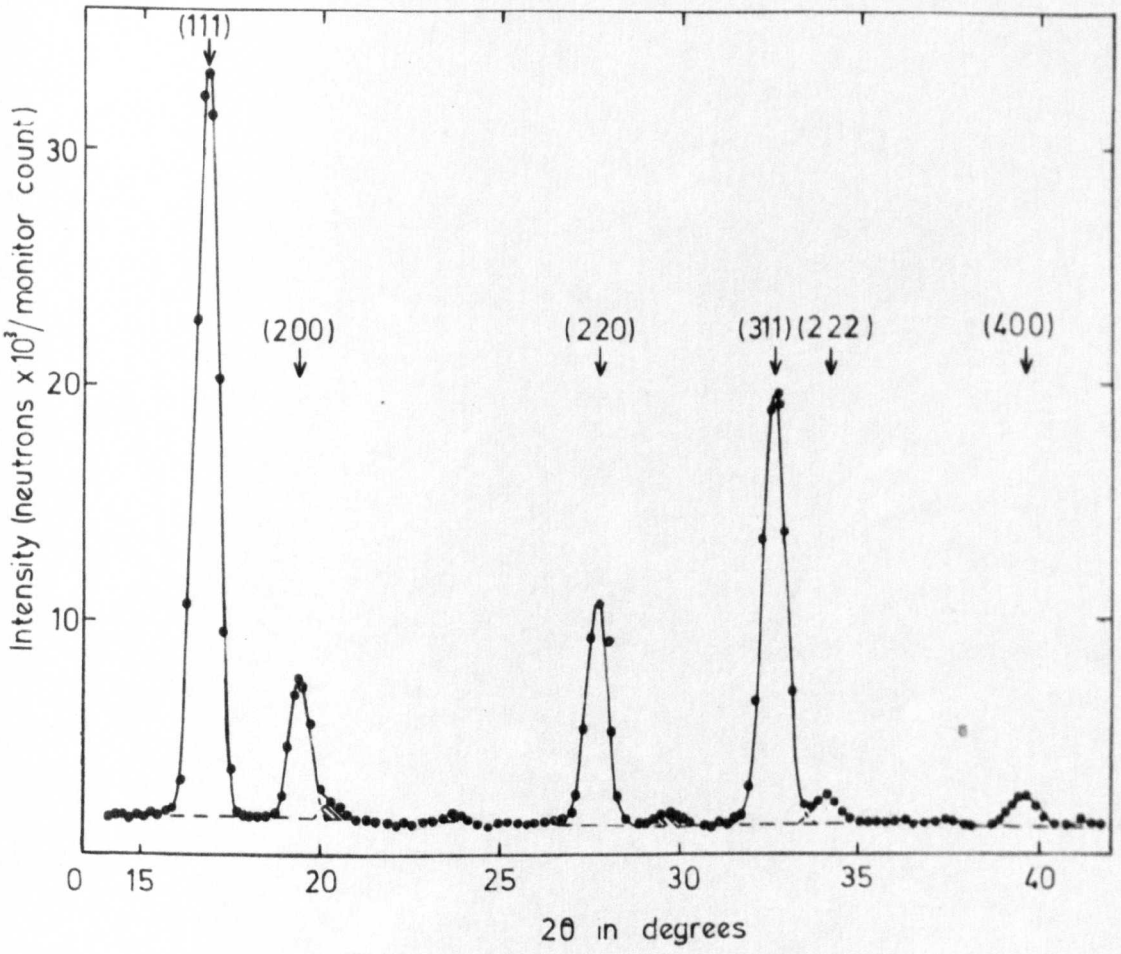

Fig. 8.18. Neutron diffraction pattern of Pd Mn Sb at 293°K

94, and an estimated Debye temperature of 150°K. The measured and calculated intensities are compared in table (8.24).

TABLE 8.24

hkl	Calculated intensities			Measured intensities
	Nuclear Cl_b		[1]. S = 0.93	
	[1]. PdMn-Sb	[3]. Pd-MnSb	$\mu_{0,293}$ = 3.44	
111	217	224	244	245
200	17.8	10.2	43	43
220	64	64	82	(82)
311	184	189	174	174
222	8.2	4.7	11	11
400	16.5	16.5	18	18

As with the X-ray results, the calculated nuclear intensities for the structures (1) and (3) do not differ much, but structure (1) is the most probable because of its similarity to the $L2_1$ structure. The measured and calculated magnetic intensities, assuming that the entire moment is confined to the Mn atoms, and that there is some random disorder, are in excellent agreement.

It is of interest to note that, in contrast to the alloys containing cobalt, this alloy has a much higher Curie temperature than the ferromagnetic Heusler alloys containing palladium.

CHAPTER 9

Summary and conclusions

9.1 Introduction

Any discussion of the intrinsic magnetic properties of an intermetallic compound must consider two principal features, firstly, the electronic configuration and spin distribution responsible for the observed magnetic moment, and secondly the coupling mechanisms responsible for the cooperative behaviour of the moments.

In chapter 2 a survey was given of the principal theories of magnetic ordering. It is known that the coupling mechanisms originate in the quantum mechanical part of the electron Coulomb energy known as the exchange energy, and direct, indirect, and superexchange mechanisms are well established. However, there are deep differences in opinion about the electronic states of the electrons contributing to the observed magnetic moment. In insulating compounds the situation is relatively simple. The energy levels of the incomplete 3d or 4f shells, although modified by the electrostatic fields of neighbouring ions, are nevertheless fairly discrete and are occupied by an integral number of electrons in accordance with Hund's rule. The nett moment of each ion is coupled to neighbouring ions via a direct or super-exchange interaction. In metals, however, the situation is complicated by the presence of conduction electrons, and a wide spectrum of viewpoints is held.

At one extreme one can consider the magnetic moments as localized in a manner essentially similar to that in insulators, and regard the effects of the conduction electrons as a minor perturbation. Non-integral magnetic moments are explained as the average of 2 or more integral moments distributed randomly through the metal. This approach has the attraction of simplicity, but is too restrictive for all but limited application.

At the other extreme is the collective electron theory. In this approximation it is assumed that the 3d and 4s electrons are sufficiently perturbed to permit itinerant behaviour, and a continuum of energy levels exists. Since the 3d and 4s bands are occupied to the same maximum Fermi energy level, the number of electrons in each band will be in general non-integral. Furthermore, if the exchange coupling favours parallel alignment, say, of the magnetic moments of the 3d electrons, the energies of those aligned parallel to the given direction will be lowered, and those aligned antiparallel will be raised with respect to the Fermi level. Consequently the numbers of spins in the two directions will not be equal, and there will be a nett spontaneous magnetization corresponding in general to a non-integral number of Bohr magnetons per atom. This theory has been applied extensively to the ferromagnetic transition metals but again further applications are limited. In transition metal alloys for example the theory treats all the 3d electrons collectively and makes virtually no distinction between the constituent elements.

The limitations of these extreme models become increasingly evident

when they are employed to explain the intrinsic magnetic properties of intermetallic compounds. When the intermetallic compound contains a rare-earth metal, the 4f electrons are well screened and may be considered to be effectively localized. The atomic moment is generally the same irrespective of the local environment, and the coupling between the moments of different atoms is via an interaction involving the conduction electrons, possibly of the RKKY type. In contrast when the intermetallic compound contains a transition group element such as iron or manganese the situation is less definite. The 3d electrons are not so well screened, and the observed atomic moment varies appreciably with environment, not only from one compound to another, but also between crystallographically different sites within the same compound. For example, Nathans et al (1958) were able to show from polarized neutron diffraction measurements that the 2 crystallographically different iron sites in Fe_3Al have different average moments. The A iron sites with 4 Fe and 4 Al atoms as nearest neighbours have an average moment of 1.46 ± 0.1 β, but the D sites which have 8 Fe atoms as nearest neighbours have an average moment 2.14 ± 0.1 β. The Al sites have no detectable moment. It is clear that the effect of the Al atoms is to reduce the moment on adjacent Fe sites, but not on the more distant Fe sites that are completely surrounded by iron atoms and possess a moment very close to the 2.2 β observed in metallic iron.

It is evident from the above discussion that neither of the extreme viewpoints is entirely appropriate to the particular case of transition group intermetallic compounds. A more viable theory is to be found

intermediate between the two extremes. It would require partial localization of the 3d electrons, but would permit a degree of itinerancy to enable them to participate to a limited extent in exchange interactions involving different atoms. The magnitudes of the atomic moments would be in general non-integral and would be dependent upon the environment of neighbouring atoms. Coupling between adjacent atoms could involve direct interactions between the 3d electrons, but longer range interactions between more distant quasi-localized 3d electrons would involve the conduction electrons possibly via some RKKY type interaction. In addition, in favourable circumstances, some form of superexchange might occur via an intervening atom.

9.2 The molecular field theory

Although intermetallic compounds are different from ionic compounds in that they cannot be fully described in terms of a strictly localized model, it is still possible to discuss their intrinsic magnetic properties in terms of the molecular field theory, provided that necessary allowance is made for deviations such as non-integral atomic moments.

In the original molecular field theory, Weiss (1907) represented the interaction of a magnetic atom with the remainder of a ferromagnetic crystal by an effective field H_e proportional to the average nett moment of the crystal, as described in equation (2.10).

$$H_e = H + cI \qquad (2.10)(9.1)$$

The relationship between the exchange integral J_e and the Curie temperature θ was developed in section (2.5) by summing over z nearest

neighbours and resulted in the energy expression of equation (2.27)

$$3k\theta = 2zJ_e S(S+1) \qquad (2.27)(9.2)$$

where $\theta = \theta_F$.

The molecular field theory was extended, principally by Néel, to the antiferromagnetic case when J_e is negative. It was assumed that the antiferromagnetic lattice could be divided into 2 antiparallel ferromagnetic sublattices A and B such that A atoms only had B atoms as nearest neighbours and vice-versa. The result of a summation over nearest neighbours only, is an expression identical to equation (9.2) but with $\theta = -\theta_N$.

9.3 The generalized molecular field theory

The molecular field theory as developed by Weiss and Néel is limited as it considers only nearest neighbour interactions, and predicts that $\theta/\theta_N = -1$. Experimental values differ very widely from this ratio, and furthermore some antiferromagnetic lattices, notably the f.c.c. lattices, cannot be divided into a simple 2 sublattice arrangement as required by the Néel treatment.

A generalized molecular field theory that overcomes these objections and includes second and more distant neighbour interactions has been developed, and is described in detail by Smart (1966). In summary, the magnetic lattice is divided into as many sublattices as is necessary to ensure that an atom has no interaction with another atom on the same sublattice, then the molecular field exerted on an atom on the i^{th} sublattice is obtained by summation of contributions from all the other sublattices. Finally, the generalized energy expression (9.3) is

obtained in place of equation (9.2)

$$3k\theta = 2S(S+1)\sum_{i=1}^{N} z_i J_i \qquad (9.3)$$

where z_i is the number of i^{th} neighbours of a particular atom over which J_i, the exchange interaction between i^{th} neighbours, operates. N is the number of sets of neighbours for which $J_i \neq 0$.

The paramagnetic Curie temperature thus represents merely the algebraic sum of all the exchange interactions acting on a given atom.

When a state of magnetic order exists, below a transition temperature $\theta_C = \theta_N$ or θ_F, then the situation is different. Essentially $k\theta_C$ is a measure of the energy required to bring a material from a state of perfect order to one in which all long range order is destroyed. It is made up of a series of contributions which can be either positive or negative, and may be represented by equation (9.4).

$$3k\theta_C = 2S(S+1)\sum_{i=1}^{N} \gamma_i z_i J_i \qquad (9.4)$$

where $\gamma_i = \pm 1$. The contribution $\gamma_i J_i$ of an i^{th} neighbour is positive if the exchange interaction is such as to support the existing moment orientation, and negative if vice-versa. Hence $\gamma_i = +1$ when i^{th} neighbours are aligned parallel, and -1 when they are aligned antiparallel.

9.4 Application of the generalized molecular field theory to alloys with the $L2_1$ and B2 structures with one magnetic atom

In order to perform the summations in equations (9.3) and (9.4) it is necessary to consider firstly where the magnetic moments may be said to be localized, and secondly how many sets of exchange interactions act

upon a particular moment.

The neutron diffraction results indicate that in most of the alloys investigated the moment is localized on one site, that of the Mn atom, except when the alloy contains cobalt when part of the moment is usually on the Co site. In view of this, the generalized theory will be developed for $L2_1$ and B2 alloys initially on the assumption that only one type of magnetic atom, the Mn atom, is present. The effect of an additional moment will be considered later. Furthermore, it will be assumed that for a particular alloy at the composition X_2MnY the moment exhibited by each Mn atom will be the same, whether the alloy is ordered in the B2 or $L2_1$ structures. The experimental results are in accord with this, and it is also reasonable theoretically since the immediate environment of each Mn atom is unchanged at the body centre of a cube of 8 nearest neighbour X atoms. In addition, it will be assumed that the same exchange interaction exists between equally spaced Mn ions in both B2 and $L2_1$ alloys, provided that the intervening atoms, if any, are the same.

It is reasonable to consider that up to 4 exchange interactions may act upon any one Mn atom. The 4 types of interaction are illustrated in figure (9.1). Table (9.1) gives the number of neighbours z_i over which the exchange interaction J_i operates in the $L2_1$ and B2 structures.

TABLE 9.1

	z_1	z_2	z_3	z_4
$L2_1$	0	12	0	6
B2	3	6	4	3/2

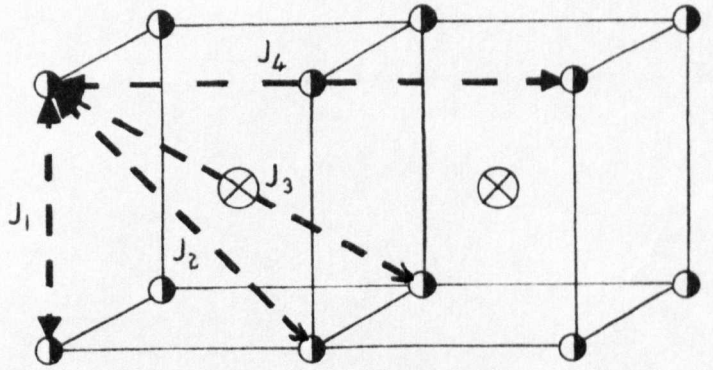

Fig. 9·1a B 2 structure X_2 (Mn Y)

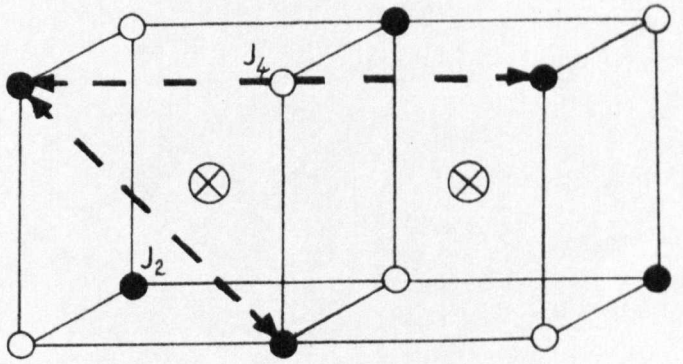

Fig. 9·1b $L2_1$ structure X_2 Mn Y

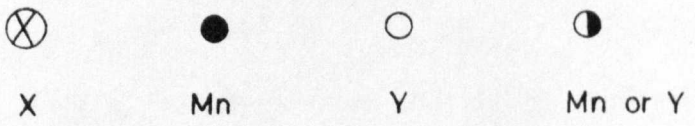

The exchange interactions J_1 J_2 J_3 and J_4 for the B_2 and $L2_1$ structures.

If $\rho = 3/2S(S + 1)$ then for 4 exchange interactions equation (9.3) becomes

$$k\rho\theta = z_1J_1 + z_2J_2 + z_3J_3 + z_4J_4 \qquad (9.5)$$

Substituting for z_i for the B2 and $L2_1$ structures results in the equations

$$k\rho\theta = 3J_1 + 6J_2 + 4J_3 + \frac{3}{2}J_4 \qquad (9.6)$$

for the B2 structure, and

$$k\rho\theta = 12J_2 + 6J_4 \qquad (9.7)$$

for the $L2_1$ structure.

The equations that may be derived from equation (9.4) depend upon the type of magnetic order that exists below the critical temperature. In ferromagnetic materials, $\gamma_i = +1$, $\theta = \theta_F$, and equations identical (9.6) and (9.7) are obtained. Thus, it is not possible from molecular field theory to determine the values of the individual exchange interactions that act on an atom in ferromagnetic materials, but only their algebraic sum, and the limiting values expressed by the inequalities A(1.3) and A(1.5).

It should be noted that no distinction is made here between θ and θ_F since no allowance has been made for short range order effects. In the calculations, θ is used wherever possible in preference to θ_F.

Antiferromagnetic structures exhibited by s.c., b.c.c., and f.c.c. magnetic lattices have been described by ter Haar and Lines (1962), and Smart (1966). Simple cubic and f.c.c. magnetic lattices may each exhibit 3 types of antiferromagnetic order, types 1, 2, and 3 respectively. All the antiferromagnetic B2 alloys investigated exhibit s.c. type 1

ordering, with nearest neighbours arranged antiferromagnetically. The antiferromagnetic $L2_1$ alloys exhibit f.c.c. type 2 ordering, with adjacent ferromagnetic (111) planes aligned antiparallel as in figure (8.10). Substituting for z_i, and $\gamma_i = +1$ or -1 respectively for parallel or antiparallel moment orientation, in the energy equation (9.4) results in the equations

$$k\rho\theta_N = -3J_1 + 6J_2 - 4J_3 + \tfrac{3}{2}J_4 \qquad (9.8)$$

for B2 s.c. type 1 antiferromagnetism, and

$$k\rho\theta_N = -6J_4 \qquad (9.9)$$

for $L2_1$ f.c.c. type 2 antiferromagnetism.

It is noted that the nett contribution of the exchange interaction J_2 to equation (9.9) is zero since half the moments involved are aligned parallel, and the other half antiparallel.

In the antiferromagnetic $L2_1$ alloys, J_2 and J_4 may be obtained explicitly from the simultaneous equations (9.7) and (9.9) by substituting θ and θ_{N2}. In the antiferromagnetic B2 alloys, expressions may be obtained for $(J_1 + \frac{4}{3}J_3)$ and $(J_2 + \frac{J}{4}4)$ by substituting θ and θ_{N1} in equations (9.6) and (9.8), but if it is assumed that $J_3 = 0$ then J_1 may be obtained explicitly. If the alloy can be ordered in both B2 and $L2_1$ structures then in principle a comparison can be made of the values obtained for J_2 and J_4 in the two cases.

9.5 Application to the alloys Pd_2MnX

All the Pd_2MnX alloys containing group III B elements Al, Ga or In are antiferromagnetic and may be obtained with the B2 structure. With appropriate heat treatment further ordering into the $L2_1$ structure is

possible in some cases. The alloys containing group 1V B elements Ge and Sn or the group V B element Sb are ferromagnetic and are doubly ordered in the $L2_1$ structure.

A summary of the structural and magnetic features is given in table (9.2), and the calculated exchange integrals are tabulated in table (9.3).

TABLE 9.2

Alloy	Structure	a_0 (A)	Θ_P (^oK)	Θ_F (^oK)	Θ_N (^oK)	μ_{00} (β)
Pd_2MnAl	B2	6.165	-215 ± 30	-	240 ± 10	4.4 ± 0.2
Pd_2MnGa	B2	6.180	$<$-108	-	210 ± 50	4.2 ± 0.3
	$L2_1$	''		-	180 ± 90	''
Pd_2MnIn	B2	6.373	-50 ± 5	-	150 ± 40	4.3 ± 0.2
	$L2_1$	''	50 ± 5	-	142 ± 3	''
Pd_2MnGe	$L2_1$	6.174	180 ± 3	170 ± 2	-	3.2 ± 0.2
Pd_2MnSn	$L2_1$	6.380	201 ± 3	189 ± 3	-	4.23± 0.1
Pd_2MnSb	$L2_1$	6.424	259 ± 3	247 ± 3	-	4.40± 0.1

TABLE 9.3

Alloy	$(J_1+\frac{4}{3}J_3)/\rho$	J_2/ρ	J_4/ρ	$(J_2+\frac{J}{2}4)/\rho$
Pd_2MnAl	-76 ± 7			2 ± 3
Pd_2MnGa	$<$-53 ± 10	$<$30 ± 15	-30 ± 15	$<$15 ± 15
Pd_2MnIn	-37 ± 5	16 ± 1	-24 ± 1	4 ± 2
Pd_2MnGe	-	$30 > \frac{J_2}{\rho} > 10$	$10 > J_4 > -30$	15 ± 1
Pd_2MnSn	-	$34 > \frac{J_2}{\rho} > 11$	$12 > J_4 > -34$	17 ± 1
Pd_2MnSb	-	$44 > \frac{J_2}{\rho} > 15$	$14 > J_4 > -44$	22 ± 2

It is noted that in all the alloys J_2 is almost certainly positive, and $(J_1 + \frac{4}{3}J_3)$ and J_4 are negative for the alloys containing group III B elements. The most complete data is available for Pd_2MnIn. If it is assumed that J_3 is small relative to J_1, then J_1 is negative, J_2 is positive, and J_4 is negative. In addition $|J_4| > |J_2|$. Hence, if only one exchange mechanism is present it must be oscillatory and must not fall off too rapidly with distance. A mechanism such as the RKKY interaction may be appropriate. Alternatively several different mechanisms, possibly including a form of superexchange, may be operating. It is clear however that alloys that contain elements from the same sub group, that might be expected to have similar electronic configurations, do have similar chemical and magnetic structures.

9.6 Application to the alloys Ni_2MnX

In the alloys Ni_2MnX the magnetic moments are principally confined to the Mn sites, and consequently it might be expected that the alloys will have magnetic properties that are similar to those of the corresponding alloys in the series Pd_2MnX. The observed structural and magnetic features are summarized in table (9.4) and the calculated exchange integrals are shown in table (9.5).

All the $L2_1$ alloys are ferromagnetic but the one alloy with a B2 structure has a complicated antiferromagnetic cone spiral spin structure.

The replacement of Pd by Ni results in a reduced cell size and an increase in magnitude of the ferromagnetic exchange forces. The antiferromagnetic exchange forces in the $L2_1$ alloys containing group III B elements may still be present, but are not so dominant. In Ni_2MnAl J_1

is still negative but not sufficiently so as to dominate and produce a simple type 1 antiferromagnetic structure.

TABLE 9.4

Alloy	Structure	a_0 (A)	θ_P (^oK)	θ_F (^oK)	θ_N (^oK)	μ_{00} (β)
Ni_2MnAl	B2	5.821	200 ± 50	-	300 ± 10	4.4 ± 0.3
Ni_2MnGa	$L2_1$	5.825		379 ± 3	-	4.17 ± 0.2
Ni_2MnIn	$L2_1$	6.068		323 ± 4	-	4.40 ± 0.05
Ni_2MnSn	$L2_1$	6.052		344 ± 3	-	4.05 ± 0.05
Ni_2MnSb	$L2_1$	6.000		360 ± 4	-	3.27 ± 0.05

TABLE 9.5

Alloy	J_2/ρ	J_4/ρ	$(J_2+\frac{J_4}{2})/\rho$
Ni_2MnAl	Antiferromagnetic cone spiral		
Ni_2MnGa	$64 > \frac{J_2}{\rho} > 21$	$21 > \frac{J_4}{\rho} > -64$	32 ± 1
Ni_2MnIn	$54 > \frac{J_2}{\rho} > 18$	$18 > \frac{J_4}{\rho} > -54$	27 ± 1
Ni_2MnSn	$58 > \frac{J_2}{\rho} > 19$	$19 > \frac{J_4}{\rho} > -58$	29 ± 1
Ni_2MnSb	$60 > \frac{J_2}{\rho} > 20$	$20 > \frac{J_4}{\rho} > -60$	30 ± 1

Smart (1966) has shown that when the ratios of the exchange integrals fall between certain limits then a non-collinear structure will have a lower energy than either a ferromagnetic or antiferromagnetic arrangement. This is evidently the case with Ni_2MnAl. The extrapolated paramagnetic and ferromagnetic Curie temperatures would be about 200^oK whereas the spiral transition temperature is 300^oK. The Néel temperature for type 1 order would presumably be between the two.

If Ni_2MnAl could be ordered into the $L2_1$ structure it would probably be ferromagnetic. Conversely, if the alloys Ni_2MnGa and Ni_2MnIn could be preferentially disordered into the B2 structure then some form of amtiferromagnetic structure, or at least a reduction in Curie temperature would be expected.

9.7 Application to the alloys Co_2MnX

It is unprofitable to analyse the magnetic structures of the alloys containing Co in terms of the simple molecular field theory since too many possible exchange forces must be considered. However, several distinct features of these alloys are evident from the summary of magnetic and structural data in table (9.6).

TABLE 9.6

Alloy	Structure	a_0 (A)	θ_F (°K)	μ_{00} (β)	μ_{293}(Co) (β)	μ_{293}(Mn)(β)
Co_2MnAl	B2	5.756	697 ± 3	4.01 ± 0.04	0.61 ± 0.1	2.50 ± 0.2
Co_2MnSi	$L2_1$	5.654	985 ± 5	5.07 ± 0.04	o.74 ± 0.07	3.52 ± 0.14
Co_2MnGa	$L2_1$	5.770	694 ± 3	4.05 ± 0.04	0.49 ± 0.05	2.82 ± 0.1
Co_2MnGe	$L2_1$	5.743	905 ± 3	5.11 ± 0.04	0.72 ± 0.08	3.48 ± 0.16
Co_2MnSn	$L2_1$	6.000	829 ± 4	5.08 ± 0.05	0.72 ± 0.08	3.48 ± 0.16
$Co_{1.75}MnSb$	$L2_1$*	5.929	600 ± 10	4.9 ± 0.1	0.52 ± 0.1	3.50 ± 0.2

All the alloys containing group 1V B elements have very similar properties. They have a nett moment of about 5 β per molecule and individual atomic moments of approximately 3.5 β and 0.75 β per Mn and Co site respectively. The Curie temperatures decrease with increasing lattice parameter in the series Si, Ge to Sn.

The alloys containing group III B elements have lower nett moments of about 4 β and correspondingly lower Curie temperatures. In common with the other series, the alloy containing Al is ordered in the B2 structure, and is presumably subject to Mn - Mn exchange forces of the type J_1. If J_1 is negative this may explain why Co_2MnAl has a Curie temperature lower than might be expected relative to the alloy containing Ga. Alternatively, Mn - Co - Mn exchange interactions along J_3 may be a contributing factor.

The alloy $Co_{1.75}MnSb$ has a nett moment similar to that of the alloys containing group IV B elements, but has a relatively low Curie temperature. This is almost certainly the effect of a reduction of the number of exchange interactions due to vacancies on some of the Co sites.

9.8 Application to the alloys Cu_2MnX

The Heusler alloys containing Cu have been the subject of many investigations, but this series is still the most incomplete, probably because the $L2_1$ structure usually only forms after very careful heat treatment, and additional phases are often present. A summary of the best available data is given in table (9.7).

TABLE 9.7

Alloy	Structure	a_0 (A)	θ_F (^oK)	μ_{00} (β)
Cu_2MnAl	$L2_1$	5.95	600 ± 10	3.7 ± 0.2
Cu_2MnIn	$L2_1$	6.2	520 ± 5	4.0 ± 0.1
Cu_2MnSn	$L2_1$	6.17	(530)	4.1 ± 0.1

In contrast to the other series, the most stable $L2_1$ alloys contain

group III B elements. All the alloys have a total moment of about 4 β and are strongly ferromagnetic, when they are ordered in the $L2_1$ structure. If the $L2_1$ structure is destroyed by appropriate heat treatment there is no tendency towards partial disorder into the B2 structure, completely new phases are formed, and these phases are non-ferromagnetic. The formation of magnetic order is clearly dependent upon the presence of certain types of chemical order.

9.9 Application to the alloys XMnSb with the Cl_b structure

In general, Heusler alloys form most readily when they contain group IV B elements. There is a tendency to form the B2 structure with group III B elements, and it is often difficult to dissolve completely 50 At.% of element X in alloys containing the group V B element Sb. However, intermetallic compounds with the Cl_b structure form readily at the equiatomic composition XMnSb. At this composition highly ordered vacancies occur in the lattice and the electron per atom ratio is clearly much different from that in the Heusler series. A summary of the principal magnetic features is given in table (9.8).

TABLE 9.8

Alloy	a_0 (A)	θ_F (^oK)	μ_{00} (β)
PdMnSb	6.233	523 ± 4	4.06 ± 0.05
NiMnSb	5.929	735 ± 5	4.05 ± 0.05
CoMnSb	5.870	471 ± 4	4.04 ± 0.05
CuMnSb	6.097	Antiferro	4.2 ± 0.2

The nett moment per molecule is approximately 4 β and is concentrated

at the Mn sites. In the alloys containing Pd and Ni the exchange integrals J_2 and J_4 are altered so as to give Curie temperatures that are higher than those of the alloys in the corresponding $L2_1$ series. The reverse behaviour is shown by CoMnSb, but this is further evidence that the high Curie temperatures of the Co_2MnX alloys is largely due to exchange forces involving the moments on the Co atoms. On the other hand, CuMnSb has a susceptibility that is complicated and is field dependent, but is definitely antiferromagnetic at low temperatures.

9.10 Summary and conclusions

A wide range of related alloys has been investigated. Manganese is the one element common to all of them, and in every case the Mn ion carries a large magnetic moment, usually about 4 β, which is coupled via some form of exchange interaction to neighbouring Mn ions in an ordered magnetic structure. In addition to the ferromagnetic configurations associated with the traditional Heusler alloys, antiferromagnetic and complex spiral spin structures have been revealed.

Some new intermetallic compounds have been discovered, and their structures have been determined. In some cases, such as Cu_2MnSb and CuMnSb, earlier data has been shown to be incomplete or of doubtful validity. Lattice parameters have been determined from X-ray diffraction photographs, and neutron diffraction data has been employed to determine quantitatively the extent and type of long range order. Magnetic structures have been determined from magnetic and neutron diffraction data.

An attempt has been made to describe the magnetic structures in

terms of a molecular field theory, and although it is not suggested that this approach is at all rigorous its application does indicate the probable signs and orders of magnitude of the exchange integrals that are present. Several important features do emerge. In particular, if elements from within a particular B sub group are considered, the lattice parameter increases with increasing atomic number, but this is usually accompanied by a decrease in magnitude of both positive and negative exchange integrals. It is not possible from these results to say whether the decrease in the exchange integrals is primarily an effect of the change in element, or is due to, the increase in lattice parameter. However, Austin and Mishra (1967) have shown that a reduction in cell size, caused by an increase in pressure, of some of the ferromagnetic Heusler alloys containing Ni, results in a small increase in Curie temperature.

It is clear however that alloys containing elements from the same sub group do tend to form similar chemical and magnetic structures, and a change from one sub group to another usually has a marked effect on the exchange integrals. Apart from CuMnSb, antiferromagnetism occurs only in alloys containing group lll B elements, and the alloys containing group lV B elements are exclusively ferromagnetic.

Qualitatively the increase in conduction concentration that presumably occurs on substitution of an element from a higher sub group results also in a relative increase in the ferromagnetic exchange integrals. But, it is difficult in the absence of any quantitative information about the conduction electron polarization or concentration

to make any detailed calculations of exchange forces, or to attempt to fit the results to an RKKY curve.

In order to further the investigation of the effect of the conduction electrons on the exchange integrals it would be of interest to perform additional measurements on these alloys so that the details of their electronic structure could be determined. It would also be most helpful if additional members of an alloy series could be formed with the $L2_1$ or B2 structures in which the degree of long range order could be carefully controlled. Complete control of the degree of B2 - $L2_1$ order in Pd_2MnIn, for example, would enable an assessment to be made of the validity of this type of molecular field approach. Further important information could be obtained if a continuous series of $L2_1$ or B2 alloys could be formed at compositions such as $Pd_2Mn(In_xSn_{1-x})$.

APPENDIX

Molecular field calculations for $L2_1$ and B2 alloys

The molecular field theory is developed in section (9.4) for s.c. type 1 magnetic lattices with half the lattice sites occupied randomly by magnetic atoms, and for f.c.c. type 2 magnetic lattices. A summary is given below of the molecular field equations for alloys with $L2_1$ and B2 chemical structures but with ferromagnetic or type 1, 2, or 3 antiferromagnetic lattices. The magnetic lattices are defined in the same manner as ter Haar and Lines (1962) and the summations have been made over the 4 interactions illustrated in figure (9.1).

a). Simple cubic magnetic lattice (B2 chemical)

$$\left.\begin{aligned}
&\text{Paramagnetic or ferromagnetic order} && \rho\theta &&= 3J_1 + 6J_2 + 4J_3 + \tfrac{3}{2}J_4 \\
&\text{Antiferromagnetic order type 1} && \rho\theta_{N1} &&= -3J_1 + 6J_2 - 4J_3 + \tfrac{3}{2}J_4 \\
&\qquad\qquad\qquad\quad \text{type 2} && \rho\theta_{N2} &&= -J_1 - 2J_2 + 4J_3 + \tfrac{3}{2}J_4 \\
&\qquad\qquad\qquad\quad \text{type 3} && \rho\theta_{N3} &&= J_1 - 2J_2 - 4J_3 + \tfrac{3}{2}J_4
\end{aligned}\right\} \quad A(1.1)$$

b). Face-centred cubic magnetic lattice ($L2_1$ chemical)

$$\left.\begin{aligned}
&\text{Paramagnetic or ferromagnetic order} && \rho\theta &&= 12J_2 + 6J_4 \\
&\text{Antiferromagnetic order type 1} && \rho\theta_{N1} &&= -4J_2 + 6J_4 \\
&\qquad\qquad\qquad\quad \text{type 2} && \rho\theta_{N2} &&= -6J_4 \\
&\qquad\qquad\qquad\quad \text{type 3} && \rho\theta_{N3} &&= -4J_2 + 2J_4
\end{aligned}\right\} \quad A(1.2)$$

For each possible state of magnetic order there is a characteristic

transition temperature Θ_F or Θ_N, but the particular type of order that will occur will be the one corresponding to the highest transition temperature. This type of order will persist at lower temperatures provided that the exchange forces are not temperature dependent. Conversely, if a particular type of order is observed, then the transition temperature corresponding to that type of order is greater than the transition temperatures corresponding to the other possible types of order.

Hence, when s.c. type 1 order persists $\Theta_{N1}(sc) > \Theta_F$, Θ_{N2} and Θ_{N3}, and when f.c.c. type 2 order exists $\Theta_{N2}(fcc) > \Theta_F$, Θ_{N1} and Θ_{N3}. When the alloys are ferromagnetic $\Theta_F > \Theta_{N1}$, Θ_{N2} and Θ_{N3}.

Applications of the above inequalities to equations A(1.1) and A(1.2) enables the following limits to be put to the values taken by the exchange integrals.

a). Ferromagnetism (B2)

$$\left.\begin{aligned} J_1 + 2J_2 &> 0 \\ J_1 + 4J_2 + 4J_3 &> 0 \\ J_1 + \tfrac{4}{3}J_3 &> 0 \end{aligned}\right\} \qquad A(1.3)$$

b). Antiferromagnetism type 1 (B2)

$$\left.\begin{aligned} J_1 - 2J_2 &< 0 \\ J_1 + 4J_3 - 4J_2 &< 0 \\ J_1 + \tfrac{4}{3}J_3 &< 0 \end{aligned}\right\} \qquad A(1.4)$$

It is noted that in the B2 structure J_4 has no effect on the type

of order that persists. Furthermore, if it is assumed that $J_3 = 0$, then J_1 is positive if ferromagnetism exists, and negative if type 1 antiferromagnetism exists.

c). Ferromagnetism ($L2_1$)

$$J_2 > 0, \qquad -J_4 < J_2 \qquad \text{A(1.5)}$$

d). Antiferromagnetism type 2 ($L2_1$)

$$J_4 < 0, \qquad J_2 < |J_4| \qquad \text{A(1.6)}$$

In this case the type of magnetic order that persists depends entirely upon the relative signs and magnitudes of J_2 and J_4.

REFERENCES

Anderson P.W., Phys. Rev. 79 (1950) 350-6

Phys. Rev. 115 (1959) 2-13

'Exchange in insulators', in 'Magnetism 1,' G.T.Rado and H.Suhl, ed. Academic Press, New York and London, 1963.

Anderson P.W., and H.Hasegawa, Phys. Rev. 100 (1955) 675-81.

Austin I.G., and P.K.Mishra, Phil. Mag. 15 (1967) 529-38.

Bacon G., 'Neutron Diffraction' O.U.P. 1962.

Bradley A.J., Proc. Phys. Soc. (London). 47 (1935) 879-99.

Bradley A.J., and J.W.Rodgers, Proc. Roy. Soc. A144 (1934) 340-59.

Castelliz L., Mh. Chem. 82 (1951) 1059-85.

Mh. Chem. 84 (1953) 765-76.

Coles B.R., W.Hume-Rothery, and H.P.Myers, Proc. Roy. Soc. A196 (1949) 125-33.

Corliss L.M., N.Elliott, and J.M.Hastings, Phys. Rev. 104 (1956) 924-8.

Crangle J., and M.J.C.Martin, J. Sci. Inst. 36 (1959) 100.

Dirac P.A.M., 'Principles of Quantum Mechanics' O.U.P. 1935.

Endo K., T.Ohoyama, and R.Kimura, J. Phys. Soc. Japan, 19 (1964) 1494-5.

Felcher G.P., J.W.Cable, and M.K.Wilkinson, J. Phys. Chem. Solids, 24 (1963) 1663-5.

de Gennes P.G., Phys. Rev. 118 (1960) 141-54.

ter Haar D., and M.E.Lines, Phil. Trans. Roy. Soc. (London) A254 (1962) 521-55.

Halpern O., and M.H.Johnson, Phys. Rev. 55 (1939) 898-923.

Hames F.A., J. Appl. Phys. 31 (1960) 370S-371S.

Heisenberg W., Zeits. f. Physik. 49 (1928) 619.

Heusler F., Verh. der deut. phys. Gesell, 5 (1903) 219.

Heusler F., Starck W., and E.Haupt, Verh. der deut. phys. Gesell 5 (1903) 220-3.

Heusler O., Ann. der Physik, 5 (1934) 155-201.

International Tables for X-ray Crystallography, Kynoch Press, Birmingham (England), 1959.

Ising E., Zeits. f. Physik, 31 (1925) 253.

Kasuya T., Prog. Theoret. Phys. 16 (1956) 45-57.

Kimura R., K.Endo, and T.Ohoyama, J. Phys. Soc. Japan, 17 (1962) 723-4.

Kouvel J.S., Gen. Electric Research Report No. 57-RL-1799. (1957).

Kramers H.A., Physica 1 (1934) 182.

Kripyakevich P.I., E.I.Gladyshevskii, and O.S.Zarechnynk, Doklady Akad. Nauk SSSR 95 (1954) 525.

Li Yin-Yuan, Phys. Rev. 100 (1955) 627-31.

Mattis D.C., 'The Theory of Magnetism' Harper and Row, New York, Evanston and London, 1965.

Nathans R., and A.Paoletti, Phys. Rev. Letters 2 (1959) 254-6.

Nathans R., M.T.Piggott, and C.G.Shull, J. Phys. Chem. Solids 6 (1958) 38-42.

Nathans R., C.G.Shull, G.Shirane, and A.Andresen, J. Phys. Chem. Solids 10 (1959) 138-46.

Nowotny H., and B.Glatzl, Mh. Chem. 83 (1952) 237-41.

Ohoyama T., P.J.Webster, and R.S.Tebble, J. Phys. D. Ser.2. 1 (1968) 951-2.

Oxley D.P., Thesis, Sheffield University, 1964.

Oxley D.P., C.T.Slack, R.S.Tebble, and K.C.Williams, Nature 197 (1962) 465.

Persson E., Naturwiss 16 (1928) 613.

Z. Physik 57 (1929) 115.

Potter H.H., Proc. Phys. Soc. 41 (1929) 135-42.

Raynor G.V., J. Inst. Metals, 70 (1944) 507.

Robinson K., Phil. Mag. 43 (1952) 775-82.

Acta Cryst. 7 (1954) 494-7.

Ross A.D., and Gray R.C., Proc. Roy. Soc. Edinburgh 31 (1910) 85-99.

Ruderman M.A., and C.Kittel, Phys. Rev. 96 (1954) 99-102.

Schneider A., and W.Wunderlich, Z. Metallk. 40 (1949) 260.

Shirane G., Acta Cryst. 12 (1959) 282-5.

Shull C.G., W.A.Strauser, and E.O.Wollan, Phys. Rev. 83 (1951) 333-45.

Slater J.C., Phys. Rev. 49 (1936) 537, 931.

Smart J.S., 'Effective Field Theories of Magnetism', W.B.Saunders Company, Philadelphia, 1966.

Stoner E.C., Proc. Roy. Soc. (London) A165 (1938) 372.

Phys. Soc. Rept. Progress Phys. 11 (1948) 43.

J. Phys. et radium 12(1951) 372.

Sucksmith W., Phil. Mag. 8 (1929) 158-65.

Proc. Roy. Soc. (London) A170 (1939) 551-60.

Sucksmith W., and S.P.Anderson, J. Sci. Inst. 33 (1956) 234-6

Sucksmith W., and L.F.Bates, Proc. Roy. Soc. (London) 104 (1923) 499.

Taglang P., and Mme. Fournier, J. de Physique 22 (1961) 295-7.

Take E., and A.Semm, Verh. der deut. phys. Gesell. 16 (1914) 971-89.

Tsuboya I., and M.Sugihara, J. Phys. Soc. Japan, 16 (1961) 1257.

J. Phys. Soc. Japan, 18 (1963) 143.

van Vleck J.H., J. Chem. Phys. 9 (1941) 85.

Weiss P., J. de Physique, 6 (1907) 667.

Wohlfarth E.P., Proc. Roy. Soc. (London) A195 (1949) 434.

Yosida K., Phys. Rev. 106 (1957) 893-8.

Young E., Phil. Mag. 46 (1923) 291-305.

Zener C., Phys. Rev. 81 (1951) 440-4.

Phys. Rev. 82 (1951) 403-5.

Phys. Rev. 83 (1951) 299-301.

Phys. Rev. 85 (1952) 324-8.

Zener C., and R.R.Heikes, Rev. Mod. Phys. 25 (1953) 191-8.